CHALMERS
UNIVERSITY OF TECHNOLOGY

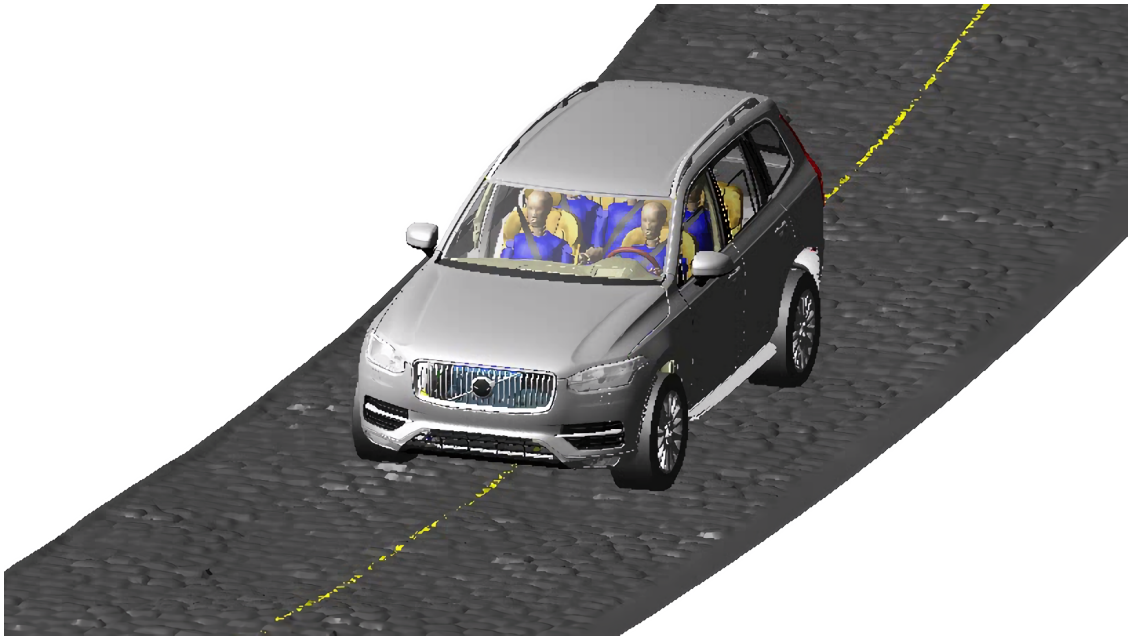

Detection and monitoring of mechanical faults in vehicles

using multivariate frequency function estimates

Master's thesis in Electrical Engineering

DANIEL MCKELVEY

DEPARTMENT OF ELECTRICAL ENGINEERING

CHALMERS UNIVERSITY OF TECHNOLOGY
Gothenburg, Sweden 2022
www.chalmers.se

Master's thesis 2022

Detection and monitoring of mechanical faults in vehicles

using multivariate frequency function estimates

DANIEL MCKELVEY

CHALMERS
UNIVERSITY OF TECHNOLOGY

Department of Electrical Engineering
Chalmers University of Technology
Gothenburg, Sweden 2022

Detection and monitoring of mechanical faults in vehicles
using multivariate frequency function estimates
DANIEL MCKELVEY

Supervisor: Tomas McKelvey, Department of Electrical Engineering
Advisor: Patrik Nordberg, Volvo Cars
Examiner: Thomas Rylander, Department of Electrical Engineering

Master's Thesis 2022
Department of Electrical Engineering
Chalmers University of Technology
SE-412 96 Gothenburg
Telephone +46 31 772 1000

Cover: Snapshot from the vehicle simulation

Typeset in LaTeX
Gothenburg, Sweden 2022

Detection and monitoring of mechanical faults in vehicles
using multivariate frequency function estimates
DANIEL MCKELVEY
Department of Electrical Engineering
Chalmers University of Technology

Abstract

Self driving vehicles are becoming increasingly common; especially in the context of testing vehicles on proving grounds. Since there is no driver to recognise mechanical faults, the vehicles may become unsafe. This thesis, as part of the research project Enablers for Testing Autonomous Vehicles at Existing Proving grounds (ETAVEP) a collaborative effort of vehicle industry in Western Sweden, developed a general detector that will detect and help localise mechanical faults. The detector uses sensors (accelerometers) placed in the vehicle to create a virtual representation of the mechanical state using the frequency function, also known as the frequency response. This state is then tracked on-line and deviations large enough from the original state will trigger the detector. Large enough is quantified by fitting a statistical model during a training phase; then in the on-line detection phase we can calculate the distance between the current state and the statistical model. Furthermore, we are able to derive a closed form expression of the distribution of the distance; thus, allowing setting the detection threshold using the probability of false alarm.
The detector was evaluated on three different sensor setups; a state of the art multi-body simulation, a vehicle in an lab environment, and lastly a proof of concept with an outfitted vehicle driving on a proving ground. The detector worked well and was able to detect the injected faults reliably.

Keywords: monitoring, system identification, multivariate, frequency domain, engineering, thesis.

Acknowledgements

I would like to thank my advisor Prof. Tomas McKelvey for prompt feedback and encouragement helping me to finish the thesis. The advice, discussions and company knowledge from Patrik Nordberg, my advisor at Volvo Cars, were instrumental in getting the thesis up and running smoothly. Lastly, I would like to thank Arvid Pearson, Volvo Cars, and the other helpful people at Volvo Cars for their fantastic work of generating and collecting the data used in the thesis; it wouldn't have happened without your work.

Daniel McKelvey, Gothenburg, November 2022

Contents

List of Figures

Symbols

$[\cdot]_{i,j}$	element (i, j) operator
$[\cdot]_i$	element (i) operator
$\boldsymbol{v}^*$	Complex conjugate of $\boldsymbol{v}$
$\boldsymbol{v}^T$	Transpose of $\boldsymbol{v}$
$\boldsymbol{v}^H = (\boldsymbol{v}^*)^T$	Hermitian transpose of $\boldsymbol{v}$
$\text{vec}(\cdot)$	Vectorisation operator
$\text{diag}(\cdot)$	Diagonal matrix operator
$G(\omega)$	Frequency Function
$R_{xy}(t)$	Cross Covariance
$\Gamma_{xy}(\omega)$	Cross Spectral Density (CSD)
$\triangleq$	Definition
$\hat{\boldsymbol{\mu}}$	Sample mean of $\boldsymbol{x}$
$\mathcal{N}(\boldsymbol{\mu}, \boldsymbol{\Sigma})$	Normal Distribution
$\mathcal{CN}(\boldsymbol{\mu}, \boldsymbol{\Gamma})$	Complex Normal Distribution
$F(\text{dn}, \text{dd})$	F-distribution
$\beta'(\alpha, \beta)$	Beta-prime distribution
χ^2_N	Chi-Squared distribution with N d.o.f,
$y[n]$	Value at time index n of Discrete Time System
MIMO	Multi-input Multi-output
MISO	Multi-input Single-output
SISO	Single-input Single-output

1
Introduction

Fault monitoring is the process of analysing real-time signals to make decisions on the current state of the system of interest. The decision could be binary, telling whether the system is okay or faulty. It can also include a deeper analysis of the error to locate the position and severity of the error. A simple strategy to detect faults is to first analyse the system during a training phase, learning the behaviour of the fault-free system. When monitoring the system, we compare the current state to the snapshot taken during the baseline phase. I.e. we first fit some model to the data collected during the baseline phase. Then during the monitoring phase we reason how likely the current state is given the baseline model. If it is not likely enough we can declare that a fault has happened.

This thesis has been a part of a larger research project which investigated methods and best practices for simultaneously testing autonomous vehicles and regular vehicles at the same proving grounds, i.e. test tracks. The project, Enablers for Testing Autonomous Vehicles at Existing Proving grounds (ETAVEP), is a collaboration between Chalmers, RISE, Volvo Cars, Volvo Trucks, Asta Zero och SafeRadar Research. This thesis investigated methods and feasibility of an automatic system for detecting mechanical faults in a vehicle. In autonomous vehicles a test driver will not always be present who has experience detecting mechanical faults, this might lead to the vehicle breaking down and being unsafe to drive. Autonomous drive systems might have functionality to detect when the vehicle behaves strangely, but with limited prior warning. Here, a set of accelerometers are placed at strategic locations to capture input signals, such as road vibrations, and output signals, such as how the frame of the vehicle moves. Using these two sets of signals the mechanical state of the vehicle can be described in a system model as a frequency function. System identification allows us to estimate the state, i.e. the parameters of the model. The estimation method can be chosen in several ways such as using a Auto-Regressive Exogenous Input (ARX) model–a parametric model, the non-parametric Empirical Transfer Function Estimate (ETFE) or using the non-parametric Local Rational Model (LRM) which is the focus of this thesis. All three methods can provide samples from the underlying frequency function. We will use statistics to reason how likely an estimated frequency function comes from the baseline mechanical system. The frequency function captures the dynamics of the system; therefore to estimate the frequency function we need to use the measured accelerations during some contiguous interval of time. The longer the interval the better the estimate. There is a trade-off to be made here since the length of the interval determines how often we can estimate the frequency function and get the status of the vehicle. This will of course influence the size and the time delay between the fault and the detection of

said fault.
The proposed method has several integral parts: choosing sensible input and output signals, a statistical model describing the system using a frequency function parameterisation, a method for estimating said frequency function, a baseline phase where the statistical model is fitted, and finally an online phase where new frequency function estimates are compared to the statistical to determine if the system has deviated from the baseline phase.

1.1 Related Work

Detecting changes in time-series data has been a research area for decades. The book by Michèle Basseville and Nikiforov (1993) gives a good overview of methods comparing the probability distributions of the past and present intervals. These methods may use either parametric or non-parametric models such as Auto-regressive (AR) and Instrumental Variable methods as an underlying assumption. There are several branches when comparing distribution-distribution or distribution-sample. There is the *cumulative sum* (Michèle Basseville and Nikiforov (1993); Gustafsson (2007)), the *marginalised likelihood-ratio* (Gustafsson 2007), *change point* (Yamanishi and Takeuchi 2002) and the *relative density* (S. Liu et al. (2013); Sugiyama, Suzuki, and Kanamori (2012); Kawahara and Sugiyama (2012))
The *subspace* methods are another type of method that have been popular (Michèle Basseville, Albert Benveniste, et al. (2006); Kawahara, Yairi, and Machida (2007); Mevel et al. (2002)). These methods fall under linear system identification methods based on either time-domain measurements or covariance driven matrices. The central idea is to measure the distance between intervals by comparing the subspaces spanned by the signals. Sequential use of methods such as *Principal Component Analysis (PCA)* and *Partial Least Squares (PLS)* (Yin et al. (2014); Qin (2012); Alcala and Qin (2009)), and *Singular Spectrum Analysis* (Moskvina and Zhigljavsky (2003); Idé and Tsuda (2007)) have been in common use for process monitoring but is seeing renewed interest in other areas.
Lastly, there is the set of Modal analysis and frequency based methods. They can be partitioned in to *global modelling* methods (Doebling et al. (1996); M. Basseville, A. Benveniste, Gach-Devauchelle, et al. (1993)), and *data driven* methods (Brincker and Ventura (2015); T. J. Johnson and D. E. Adams (2002); Pintelon et al. (2011)). The *global modelling* methods also perform damage identification by comparing the present model estimate to known failure modes (F. P. Kopsaftopoulos and S. D. Fassois (2013); F. P. Kopsaftopoulos and S. D. Fassois (2010)).

1.2 Contributions

The frequency function method used in this work fall under the data driven frequency based methods. It is also similar to the subspace methods, but instead of comparing the subspaces of the signals we compare the distribution of the system state (frequency function). More explicitly, the contributions of the thesis are: formalising a detector on multivariate transfer function estimates where the derived

statistic is shown to have a F-distribution under normality assumptions, and experimental evaluation of the detector using both measured and simulated data with several different systems, operating points and faults.

1.3 Outline

The thesis, following the introductory chapter, is split into four chapters. The Theory chapter builds the necessary theoretical foundation. The Method chapter describes the detection method and data flow associated with it. In the Results chapter the detection method is applied to three different data sets, and the effects of different parameter choices is investigated. In one data set the method was tested live in a car driving on different road surfaces. Finally, in the Conclusion and Discussion we analyse the implications of the results and expand on some lessons when using the method.

2
Theory

As outlined in the introduction we are interested in analysing a multi-input multi-output dynamic system. Assuming further that the system is linear time invariant (LTI) simplifies the analysis and confers some useful properties, such as the frequency function of the linear system is time invariant. As any nonlinear system can be approximated by a linear system around a operating point (Kay 1993) the linear methodology can also be applied to non-linear systems for small signal variations around a nominal operating point. The time invariance assumption holds as long as the mechanical system does not change. Hence, our focus is to detect changes in linear systems, and we approach the problem by detecting changes to the frequency function of the dynamic system.
To define the assumed LTI system, the set of available signals need to be split into natural input signals and output signals. An important property is that the input signals don't depend on the output signals, i.e. the input signals are causal to each output signal. Another is that the input signals capture the important excitation to the system, and the outputs capture the responses in the parts of the system that should be monitored. The sensor locations and the split between input and output signals should be based on physical insight so that the assumed LTI system which relate the inputs to the outputs is a causal system. The measurements taken on these input and output signals are used to reconstruct the frequency function which reflects the mechanical state of the vehicle. We have exclusively used accelerations, simulated or measured from accelerometers, since they are easy to measure in a practical setting. The measured signals are split into m input signals and p output signals.

2.1 LTI model and frequency function

The relationship between the inputs and outputs are modelled as a multivariate causal equidistantly sampled discrete time (DT) linear system. The vector output at time index n, $\boldsymbol{y}[n] \in \mathbb{R}^p$ is therefore assumed to be

$$\boldsymbol{y}[n] = \sum_{k=0}^{\infty} g[k]\boldsymbol{u}[n-k] \tag{2.1}$$

where $g[i] \in \mathbb{R}^{p\times m}$ is the matrix valued impulse response of the DT linear system and $\boldsymbol{u}[n] \in \mathbb{R}^m$ is the input signal. We note that since we are working with equidistant samples each time index corresponds to one point in time. The discrete time Fourier transform (DTFT) of the matrix valued impulse response is the frequency function,

also known as the frequency response, of the linear system and is defined as

$$G(\omega) \triangleq \sum_{k=-\infty}^{\infty} g[k]e^{-j\omega k} = \sum_{k=0}^{\infty} g[k]e^{-j\omega k}, \tag{2.2}$$

and is a continuous matrix valued function with complex elements. The second equality is due to the system being causal.
Since we are interested in monitoring the frequency function, it needs to be estimated from the collected input and output signals on a finite time interval, denoted a window. A window consists of N samples from the accelerometers (sensors) sampled at rate f_s. Once each segment is measured, we apply an estimation method to estimate the frequency function on that segment.

2.2 Estimating the frequency function

The detection method developed in this work use the frequency function estimated at select frequencies as a representation of the system status, i.e. the mechanical state of the vehicle. Below we describe three methods to calculate these samples from a window of sensor data. The LRM and ETFE methods are non-parametric methods as they don't impose any global model structure of the linear system and by extension to the frequency function. The third method is the ARX method which is a parametric method as it imposes a global model of the linear system.

2.2.1 Empirical Transfer Function Estimate

The Empirical Transfer Function Estimate (ETFE) (Ljung 1999) is a simple non-parametric method were the MIMO frequency function is constructed from the pair-wise SISO (single-input single-output) frequency function, which are estimated using spectral estimation of the input and output signals.
For a stationary random process $u[n]$, its autocorrelation function is defined as

$$\gamma_{uu}[m] \triangleq \mathrm{E}\left[u^*[n]u[n+m]\right] \tag{2.3}$$

where $\mathrm{E}\left[\cdot\right]$ is the average and $\cdot^*$ is the complex conjugate. The Wiener-Khintchine theorem shows that the Fourier transform of the autocorrelation function is the spectral density (Proakis and Manolakis 2007)

$$\Gamma_{uu}(\omega) \triangleq \sum_{k=-\infty}^{\infty} \gamma_{uu}[k]e^{-j\omega k}. \tag{2.4}$$

Following Proakis and Manolakis 2007 (p.326), a LTI system's cross-correlation between the input $u[n]$ and its output $y[n]$ can be defined by multiplying Equation (2.1) by $u^*[n-m]$ and taking the expected value, we get

$$\begin{aligned}\gamma_{yu}[m] \triangleq \mathrm{E}\left[y[n]u^*[n-m]\right] &= \mathrm{E}\left[\sum_{k=0}^{\infty} g[k]u^*[n-m]u[n-k]\right] \\ &= \sum_{k=0}^{\infty} g[k]\,\mathrm{E}\left[u^*[n-m]u[n-k]\right] \\ &= \sum_{k=0} g[k]\gamma_{uu}[m-k].\end{aligned} \tag{2.5}$$

We note that it's the convolution of the impulse response $g[n]$ and the autocorrelation function of input signal. Moving to the frequency domain by taking the Fourier transform of the equation we get that the cross spectral density of $u[n]$ and $y[n]$ is

$$\Gamma_{yu}(\omega) = G(\omega)\Gamma_{uu}(\omega). \tag{2.6}$$

Rearranging the terms, an unknown system can then be identified by

$$G(\omega) = \frac{\Gamma_{yu}(\omega)}{\Gamma_{uu}(\omega)}. \tag{2.7}$$

By collecting the pairwise estimated frequency functions we can build the estimated MIMO frequency function as

$$\left[\hat{G}_{\text{ETFE}}(\omega)\right]_{i,j} \triangleq \frac{\hat{\Gamma}_{y_i u_j}(\omega)}{\hat{\Gamma}_{u_j u_j}(\omega)}. \tag{2.8}$$

The object $[G]_{ij}$ denotes the element on the i^{th} row and j^{th} column of the matrix, and it's the univariate frequency function between the j^{th} input signal and the i^{th} output signal.
The problem has now reduced to estimating the closely related cross spectral density $\hat{\Gamma}_{yu}(\omega)$ and the spectral density $\hat{\Gamma}_{uu}$.
A common way to estimate the spectral densities, is to use Welch's method of averaged estimates, with a suitably chosen windowing function (Welch (1967), Solomon (1991), Heinzel, Rüdiger, and Schilling (2002)). The methods works by applying the windowing function multiple times with a suitable overlap over the data set, this results in several shorter signals, over which the CSD is estimated. We can note that the frequency resolution of these shorter signals will be lower and proportional to the shorter signal length. These CSD estimates are then averaged to an estimate with lower variability and lower frequency resolution (Heinzel, Rüdiger, and Schilling 2002).

2.2.2 Local Rational Model (LRM)

The LRM method for scalar valued transfer functions was introduced in McKelvey and Guerin (2012); we will extend the method for the MIMO transfer function case. A MIMO version of the original LRM method has also been described by Voorhoeve, Maas, and Oomen (2018) where a matrix fraction description parameterisation is used instead.

Preliminary results

The discrete time Fourtier transform (DTFT) a of a signal $x[n]$ is defined as

$$X(\omega) \triangleq \sum_{k=-\infty}^{\infty} x[k]e^{-j\omega k}. \tag{2.9}$$

If the signal is periodic with length N, or if the signal is a finite sequence of equally spaced samples of a function the Discrete Fourier transform can be used instead. It is defined as

$$X[m] \triangleq \sum_{k=0}^{N-1} x[k] e^{-j\frac{2\pi m}{N}k} \tag{2.10}$$

The DFT forms the basic analysis method to derive non-parametric estimates of the transfer function based on a finite window of samples of the input and output signal of the system under study.
Any causal discrete time linear system of finite McMillan degree n can be described by (see e.g Kailath (1980)) a state space model of order η

$$\begin{aligned} \boldsymbol{x}[n+1] &= \boldsymbol{A}\boldsymbol{x}[n] + \boldsymbol{B}\boldsymbol{u}[n] \\ \boldsymbol{y}[n] &= \boldsymbol{C}\boldsymbol{x}[n] + \boldsymbol{D}\boldsymbol{u}[n] + \boldsymbol{v}[n] \end{aligned} \tag{2.11}$$

where $\boldsymbol{x}[n] \in \mathbb{R}^{\eta}$ is the state-vector and $(\boldsymbol{A}, \boldsymbol{B}, \boldsymbol{C}, \boldsymbol{D})$ are the state-space matrices. The system has the corresponding frequency function

$$G(\omega) = \boldsymbol{D} + \boldsymbol{C}(e^{j\omega}\boldsymbol{I} - \boldsymbol{A})^{-1}\boldsymbol{B} \tag{2.12}$$

It was shown in McKelvey (2000) that the N-point DFT of the input and output signals are related as, for $m = 0, \ldots, N-1$

$$Y[m] = G(\omega_m)U[m] + T(\omega_m) + V[m] \tag{2.13}$$

where $\omega_m = 2\pi m/N$ and

$$\begin{aligned} G(\omega) &= \boldsymbol{D} + \boldsymbol{C}(e^{j\omega}\boldsymbol{I} - \boldsymbol{A})^{-1}\boldsymbol{B} \\ T(\omega) &= \boldsymbol{C}(e^{j\omega}\boldsymbol{I} - \boldsymbol{A})^{-1}(\boldsymbol{x}(0) - \boldsymbol{x}(N))e^{j\omega} \end{aligned} \tag{2.14}$$

This result shows that the DFT of the output $Y[m]$ is, beside the noise $V[m]$, the sum of the effect of the input, $G(\omega_m)U[m]$, and a second term $T(\omega_m)$ which depends on the initial and final state value. We also note that both $G(\omega)$ and $T(\omega)$ share the same dynamics, since the A matrix is common for both of them.

Local frequency function estimation

The MIMO LRM method forms an estimate at frequency $\omega_k = 2\pi k/N$ by a locally parameterised model which is based on the structure in (2.13). In the paper Pintelon et al. (2011) a local polynomial model is used to estimate frequency response function. We extend this to a local rational model following McKelvey and Guerin (2012). Without loss of generality we can model the frequency function for each output channel individually and we parameterise the local models of $G(\omega)$ and $T(\omega)$ for frequency k and output i as

$$G^i_{k+r} = \frac{N^i_{k+r}}{D^i_{k+r}}, \quad T^i_{k+r} = \frac{M^i_{k+r}}{D^i_{k+r}} \tag{2.15}$$

where r is an integer representing the distance to the centre frequency k and

$$N^i_{k+r} = \sum_{s=0}^{n_{\mathrm{LRM}}} N^i_s(k) r^s, \quad D^i_{k+r} = 1 + \sum_{s=1}^{n_{\mathrm{LRM}}} d^i_s(k) r^s, \quad M^i_{k+r} = \sum_{s=0}^{n_{\mathrm{LRM}}} m^i_s(k) r^s \tag{2.16}$$

were $d_s^i(k)$ and $m_s^i(k)$ are complex scalars and the row vector $N_s^i(k) \in \mathbb{C}^{1\times m}$ form the parameters of the model and n_{LRM} is the local model order. From (2.13) we can now express a local model for the output channel i as

$$[Y(k+r)]_i = \frac{N_{k+r}^i}{D_{k+r}^i}U(k+r) + \frac{M_{k+r}^i}{D_{k+r}^i} + [V(k+r)]_i \tag{2.17}$$

where the notation $[\cdot]_i$ denotes the vector element i. Let θ_k^i denote a vector comprising all the local rational model parameters $\{N_s^i(k)\}_{s=0}^{n_{\text{LRM}}}$, $\{d_s^i(k)\}_{s=1}^{n_{\text{LRM}}}$ and $\{m_s^i(k)\}_{s=0}^{n_{\text{LRM}}}$. It is clear from (2.17) that the model parameters appears as nonlinear in the expression for $[Y(k+r)]_i$. However if both sides of (2.17) is multiplied by D_{k+r}^i all parameters will be linear in the equation. To estimate the parameters of the local model, DFT data at indices $k+r$ where $r = -N_w, \ldots, N_w$ (N_w is the bandwidth) are used to form the least-squares problem

$$\hat{\theta}_k^i = \arg\min_{\theta_k^i} \sum_{r=-N_w}^{N_w} \left| [Y(k+r)]_i D_{k+r}^i - N_{k+r}^i U(k+r) - M_{k+r}^i \right|^2 \tag{2.18}$$

where $\hat{\theta}_k^i$ is the optimal parameter vector for output i at frequency index k. When forming (2.18) some indices $k+r$ might fall outside the set $\{0, 1, \ldots, N-1\}$. In this case we use the $N-$periodic property of the DFT that for any integer k, it holds that $U(k+N) = U(k)$ and $Y(k+N) = Y(k)$. The MIMO LRM estimate of row i in $G(\omega_k)$ then follows as

$$[\hat{G}_{\text{LRM}}(\omega_k)]_{i,:} = \hat{G}_{k+0}^i = \frac{\hat{N}_{k+0}^i}{\hat{D}_{k+0}^i} = \hat{N}_{k+0}^i \tag{2.19}$$

where $[\cdot]_{i,:}$ denote row i in the matrix. The number of parameters in the local model is $(n_{\text{LRM}}+1)(m+1)+n_{\text{LRM}}$ and a necessary conditions for the optimisation problem (2.18) to have a unique solution is that

$$2N_w + 1 \geq (n_{\text{LRM}}+1)(m+1) + n_{\text{LRM}}. \tag{2.20}$$

2.2.3 Auto-regressive exogenous input (ARX)

The Auto-regressive model family is commonly used in fault detection systems (Spilios D. Fassois and Fotis P. Kopsaftopoulos (2013); Michèle Basseville and Nikiforov 1993) and follows from the linear state-space models. The Auto-regressive exogenous input (ARX) models the output signals $y[n]$ as a linear combination of a finite number of past outputs, the present input and a finite number of past inputs. The model for each output channel y_i is given by the equation

$$y_i[n] = \sum_{k=1}^{n_{\text{ARX}}} a_{ik} y_i[n-k] + \sum_{k=0}^{n_{\text{ARX}}} \boldsymbol{B}_{ik}\boldsymbol{u}[n-k] \quad \text{for } i = 1, 2, \ldots, p. \tag{2.21}$$

The ARX model order n_{ARX} is a hyper-parameter that needs to be set before estimating the other parameters; this sub-problem in known as the model order identification problem. There are several heuristics such as the AIC and BIC that estimate

the model quality taking model complexity in to account that can be used in model selection. Once the model order is chosen the parameters $A_{il} \in \mathbb{R}$ $B_{il} \in \mathbb{R}^{1\times m}$ can be estimated. A common approach is by solving the least-squares problem (Ljung (1999); Söderström and Stoica (1989)) and is the method used here.
The frequency response of a stable ARX model for output index i is given by

$$[G_{\mathrm{ARX}}(\omega)]_i = \frac{\sum_{l=0}^{n_{\mathrm{ARX}}} \boldsymbol{B}_{il} e^{-j\omega l}}{\sum_{l=1}^{n_{\mathrm{ARX}}} a_{il} e^{-j\omega l}}. \tag{2.22}$$

2.3 Complex Random Variables

We can use the methods described in the previous section to calculate frequency function estimates. Since we use a window of size N to calculate them there will be variations due to noise, non-linearities and state before the window. We can quantify this behaviour by assuming that the frequency function follows some distribution under original (normal) conditions. The common choice of assuming a Normal distribution works well and any deviations can be handled easily. Since the frequency function is complex the Normal distribution needs to be extended for complex values. A complex random variable $\tilde{x}$ is defined as $\tilde{x} = u + jv$, where u and v are the real and imaginary parts, and are both real random variables on the same probability space. They will generally not be independent and have a joint probability density function p_{uv}. The mean is defined as

$$\mathrm{E}\left[\tilde{x}\right] \triangleq \mathrm{E}\left[u\right] + j\,\mathrm{E}\left[v\right], \tag{2.23}$$

where the expectation is with respect to the marginal PDF of u and v. The variance is defined as

$$\mathrm{var}(\tilde{x}) \triangleq \mathrm{E}\left[|\tilde{x} - \mathrm{E}\left[(\tilde{x}\right]|^2\right], \tag{2.24}$$

which reduces to

$$\mathrm{var}(\tilde{x}) = \mathrm{E}\left[|\tilde{x}|^2\right] - |\,\mathrm{E}\left[\tilde{x}\right]|^2, \tag{2.25}$$

The covariance between univariate $\tilde{x}$, $\tilde{y}$, is defined as

$$\mathrm{cov}(\tilde{x}, \tilde{y}) \triangleq \mathrm{E}\left[(\tilde{x} - \mathrm{E}\left[\tilde{x}\right])(\tilde{y} - \mathrm{E}\left[\tilde{y}\right])^*\right], \tag{2.26}$$

where * is the complex conjugate.
To simplify the distribution, and reduce the number of parameters needed, we assume the real and complex parts are circularly symmetric. For a circularly symmetric normal random variable the real and imaginary components are independent with equal variance. We can write this as a standard 2-dimensional Normal random variable

$$\begin{bmatrix} u \\ v \end{bmatrix} \sim \mathcal{N}\left(\begin{bmatrix} \mu_u \\ \mu_v \end{bmatrix}, \begin{bmatrix} \sigma^2/2 & 0 \\ 0 & \sigma^2/2 \end{bmatrix}\right), \tag{2.27}$$

or in complex form defining $\tilde{x} = u + jv$, $\mu_{\tilde{x}} = \mu_u + j\mu_v$

$$\tilde{x} \sim \mathcal{CN}(\mu_{\tilde{x}}, \sigma^2) \tag{2.28}$$

where $\mathcal{CN}$ denotes the normal Gaussian distribution. The probability density function (PDF) of $\tilde{x}$ has the following shape:

$$p(\tilde{x}) = \frac{1}{\pi\sigma^2} e^{-\frac{|\tilde{x}-\mu_{\tilde{x}}|^2}{\sigma^2}} \tag{2.29}$$

according to Kay 1993. For a non-circularly-symmetric treatment see Picinbono 1996.

2.3.1 Multivariate Case

Since the frequency function estimates are for MIMO systems and are estimated at multiple frequencies we need to further extend our treatment to the multivariate complex case. The multivariate circularly symmetric case is defined by the expected value, and the real valued covariance matrix $\boldsymbol{A}$ and real valued cross covariance matrix $\boldsymbol{B}$.

$$\begin{bmatrix} \boldsymbol{u} \\ \boldsymbol{v} \end{bmatrix} \sim \mathcal{N}\left(\begin{bmatrix} \boldsymbol{\mu}_u \\ \boldsymbol{\mu}_v \end{bmatrix}, \frac{1}{2} \begin{pmatrix} \boldsymbol{A} & -\boldsymbol{B} \\ \boldsymbol{B} & \boldsymbol{A} \end{pmatrix} \right) \tag{2.30}$$

where $\boldsymbol{A}$ and $\boldsymbol{B}$ can be calculated as

$$\begin{aligned} \frac{1}{2}\boldsymbol{A} &= E[(\boldsymbol{u}-\boldsymbol{\mu}_u)(\boldsymbol{u}-\boldsymbol{\mu}_u)^T] = E[(\boldsymbol{v}-\boldsymbol{\mu}_v)(\boldsymbol{v}-\boldsymbol{\mu}_v)^T] \\ \frac{1}{2}\boldsymbol{B} &= E[(\boldsymbol{v}-\boldsymbol{\mu}_v)(\boldsymbol{u}-\boldsymbol{\mu}_u)^T] = -E[(\boldsymbol{u}-\boldsymbol{\mu}_u)(\boldsymbol{v}-\boldsymbol{\mu}_v)^T]. \end{aligned}$$

We note that since $\begin{bmatrix} \boldsymbol{A} & -\boldsymbol{B} \\ \boldsymbol{B} & \boldsymbol{A} \end{bmatrix}$ is a covariance matrix it is symmetric; hence, $\boldsymbol{A}$ is symmetric ($\boldsymbol{A} = \boldsymbol{A}^T$) and $\boldsymbol{B}$ is skew symmetric ($\boldsymbol{B} = -\boldsymbol{B}^T$).
Let $\tilde{\boldsymbol{x}} = \boldsymbol{u} + j\boldsymbol{v}$, $\tilde{\boldsymbol{\mu}} = \boldsymbol{\mu}_u + j\boldsymbol{\mu}_v$, and $\boldsymbol{\Gamma} = \boldsymbol{A} + j\boldsymbol{B}$, then

$$\tilde{x} \sim \mathcal{CN}(\tilde{\boldsymbol{\mu}}, \boldsymbol{\Gamma}) \tag{2.31}$$

with the PDF

$$p(\tilde{\boldsymbol{x}}) = \frac{1}{\pi^n \det(\boldsymbol{\Gamma})} e^{-(\tilde{\boldsymbol{x}}-\tilde{\boldsymbol{\mu}})^H \boldsymbol{\Gamma}^{-1}(\tilde{\boldsymbol{x}}-\tilde{\boldsymbol{\mu}})}, \tag{2.32}$$

where ^{H} is the Hermitian (conjugate) transpose, Kay 1993. We note that Γ is a Hermitian positive definite matrix since $\boldsymbol{\Gamma}^H = \boldsymbol{A}^H - j\boldsymbol{B}^H = \boldsymbol{A} + j\boldsymbol{B} = \boldsymbol{\Gamma}$.

2.4 Statistical results

To be able to compare and quantify how close objects are there needs to be some function that measures the distance between them. In Euclidean space the distance metric is the standard $\mathrm{d}(x, y) = \|x - y\|$. To be able to quantify how close a sample $\boldsymbol{x}$ (of the frequency function) is to the probability distribution M of the frequency function a distance function is needed that handle these objects.
The Mahalanobis Distance $D(\boldsymbol{x}) \triangleq \sqrt{(\boldsymbol{x}-\boldsymbol{\mu})^T \boldsymbol{\Sigma}^{-1} (\boldsymbol{x}-\boldsymbol{\mu})}$ measures the distance of a sample $\boldsymbol{x}$ to a distribution M that has mean $\boldsymbol{\mu} = E[M]$ and a positive definite covariance $\boldsymbol{\Sigma} = \mathrm{cov}(M)$. Since the square root is a strictly increasing monotonic

function any ordering $\tau_1 < \tau_2 < \ldots < \tau_j < \ldots$ is preserved $\sqrt{\tau_1} < \sqrt{\tau_2} < \ldots < \sqrt{\tau_j} < \ldots$ (Rudin 1976); thus, we can drop the square root.
The Mahalanobis distance has a close relationship to hypothesis testing of the mean and is a common metric in statistical process monitoring, for example see R. A. Johnson and Wichern 2002.
The Mahalanobis distance can be extended for circularly symmetric complex distributions having mean $\tilde{\boldsymbol{\mu}}$ and positive definite variance $\boldsymbol{\Gamma}$

$$D_M^2(\tilde{\boldsymbol{x}}) \triangleq (\tilde{\boldsymbol{x}} - \tilde{\boldsymbol{\mu}})^H \boldsymbol{\Gamma}^{-1} (\tilde{\boldsymbol{x}} - \tilde{\boldsymbol{\mu}}). \tag{2.33}$$

Since $\boldsymbol{\Gamma}$ is Hermitian and positive definite, its inverse is also positive definite. Therefore, the complex extension to the Mahalanobis distance always take non-negative values.
Since the mean and covariance of the frequency function is unknown, the sample mean $\hat{\boldsymbol{\mu}}$ and sample covariance $\boldsymbol{S}$ needs to be used instead. If we assume that covariance $\boldsymbol{\Gamma}$ of the frequency function is diagonal, i.e. all complex values of the frequency function are independent and circularly complex. Then $\boldsymbol{\Gamma}$ can be written as

$$\boldsymbol{\Gamma} = \operatorname{diag}(\sigma_1^2, \sigma_2^2, \ldots, \sigma_{mpq}^2), \tag{2.34}$$

where m is the number of input signals, p is the number of output signals, and q is the number of frequencies where the frequency function is estimated. The mean and variance can then be estimated independently for each element i as

$$\begin{aligned} [\hat{\boldsymbol{\mu}}]_i &\triangleq \frac{1}{k} \sum_{k=1}^{k} [\boldsymbol{x}_k]_i \quad i = 1, 2, \ldots, mpq \\ \hat{\sigma}_i^2 &= \frac{1}{k-1} \sum_{k=0}^{k-1} ([\boldsymbol{x}_k]_i - [\hat{\boldsymbol{\mu}}]_i)^* ([\boldsymbol{x}_k]_i - [\hat{\boldsymbol{\mu}}]_i) \\ \boldsymbol{s} &= \operatorname{diag}(\hat{\sigma}_1^2, \hat{\sigma}_2^2, \ldots, \hat{\sigma}_{mpq}^2) \end{aligned} \tag{2.35}$$

where $[\hat{\boldsymbol{\mu}}]_i$ is the i^{th} element in the vector $\hat{\boldsymbol{\mu}}$.
We can define a similar statistic—which we denote the T-statistic using the sample mean and covariance as

$$T = k(\boldsymbol{x} - \hat{\boldsymbol{\mu}})^H \boldsymbol{S}^{-1} (\boldsymbol{x} - \hat{\boldsymbol{\mu}}) \tag{2.36}$$

for some factor k. This is closely related to Hoteling's T^2 statistic and Control Charts see e.g. R. A. Johnson and Wichern 2002.
In the univariate case the sample variance follows a scaled χ^2-distribution, Hoteling's T^2 statistic follows a F-distribution. Later in the text this will be relevant when setting the detection limits will be important. We will use the quantile function also called the inverse cumulative distribution function. It specifies the minimum x such that a random sample lies below x is p ($\mathrm{P}(X \leq x) = p$). Therefore knowing the distribution of the T-statistic is very helpful.
In the following Lemmas and Theorem we show that the T-statistic follows a F-distribution with known parameters. We first show that for univariate circularly symmetric complex Normal distribution with samples $x', x_1, \ldots, x_K$ the random

variable defined by $t = K/(K+1)|x' - \hat{\mu}|^2/\hat{\sigma}^2$ follows a $F(2, 2K-2)$ distribution. Further, we show that a sum of i.i.d. F-distributions are also F-distributed. Lastly, we show that the random variable T defined in Equation (2.36) also follows a F-distribution with known parameters. The results hold when $\boldsymbol{S}$ is diagonal, if it is not diagonal there are only results when $\boldsymbol{\mu}$ and $\boldsymbol{\Gamma}$ are known.

Lemma 1. *Let $x', x_1, \ldots, x_K$ be i.i.d. from $\mathcal{CN}(\mu, \sigma^2)$, with $\mu \in \mathbb{C}$, $\sigma^2 \in \mathbb{R}$ and let $\hat{\mu}$ be the sample mean and $\hat{\sigma}^2$ be the sample variance and the statistic t defined as*

$$\begin{aligned} \hat{\mu} &\triangleq \frac{1}{K}\sum_{k=1}^{K} x_k, \quad \hat{\sigma}^2 \triangleq \frac{1}{K-1}\sum_{k=1}^{K} |x_k - \hat{\mu}|^2 \\ t &= \frac{K}{K+1}\frac{|x' - \hat{\mu}|^2}{\hat{\sigma}^2} \end{aligned} \tag{2.37}$$

Then the statistic t has a $F(2, 2K-2)$ distribution.

Proof. First we note that if $z \sim \mathcal{CN}(0, \sigma^2)$ then the real and imaginary part of z are i.i.d. $\mathcal{N}(0, \sigma^2/2)$, a normal distribution, Kay 1993.
Clearly $(x' - \hat{\mu}) \sim \mathcal{CN}(0, \frac{K+1}{K}\sigma^2)$ and hence

$$t_1 = \frac{2K|x' - \hat{\mu}|^2}{\sigma^2(K+1)} \sim \chi^2_2 \tag{2.38}$$

has chi-squared distribution with 2 degrees of freedom (since the magnitude squared is the sum of the squared real and imaginary parts). From Equation (2.27) we see that $\hat{\sigma}^2$ can be interpreted as the sum of the sample variance estimate of the real and imaginary parts respectively. Since the sample covariance based on K samples from a Gaussian distribution has $K-1$ degrees of freedom, the sample covariance based on K samples from a complex Gaussian distribution will have $2K-2$ degrees of freedom and we conclude that the statistic

$$t_2 = \frac{2K-2}{\sigma^2}\hat{\sigma}^2 \sim \chi^2_{2K-2} \tag{2.39}$$

i.e. a chi-squared distribution of $2K-2$ degrees of freedom. Since sample mean and sample covariance are independent for the normal distribution this property is carried over to the complex normal distribution and hence it follows that t_1 and t_2 are independent since $(x' - \hat{\mu})$ is independent of $\hat{\sigma}^2$. The result now follows since $t = \frac{t_1/2}{t_2/(2K-2)}$. See e.g. Grimmett and Stirzaker 2001 for details of the F-distribution. □

The next Lemma is a technical result that allows us to transform a F-distribution to a β'-distribution. Which we then can leverage to show that sums of F-distributions are F-distributed.

Lemma 2. *Let $X \sim F(2\alpha, 2\beta)$, and define $Y = \frac{\alpha}{\beta}X$. Then $Y \sim \beta'(\alpha, \beta)$ i.e. has a beta prime distribution with parameters α, β*

Proof. Since

$$\begin{aligned} P(Y \leq y) = P(\frac{\alpha}{\beta}X \leq y) = P(X \leq \frac{\alpha}{\beta}y) = \\ \int_0^{\frac{\alpha}{\beta}y} \frac{(\frac{\alpha}{\beta})^\alpha x^{\alpha-1}(1 + \frac{\alpha}{\beta}x)^{-\beta-\alpha}}{B(\alpha, \beta)}\mathrm{d}x \underset{z=\frac{\alpha}{\beta}x}{=} \int_0^y \frac{z^{\alpha-1}(1+z)^{-\alpha-\beta}}{B(\alpha, \beta)}\mathrm{d}z \end{aligned} \tag{2.40}$$

where we used the probability density function of the F-distribution Grimmett and Stirzaker 2001, and a change of variable. We remark that the CDF of Y follows a $\beta'(\alpha, \beta)$-distribution (Steutel and Harn 2003). □

In the following Lemma we show that a sum of n i.i.d. F-distributed random variables is also F-distributed. This is an important result since it gives a closed form solution of the distribution of the T-values.

Lemma 3. *Assume the variables $t_1, t_2, \ldots, t_n$ are i.i.d. from $F(2a, 2b)$, $a, b > 0$. Then*

$$T' = \frac{a}{b} \sum_{i=1}^{n} t_i \tag{2.41}$$

is distributed as $\beta'(\gamma, \delta)$, and

$$T = \frac{a\delta}{b\gamma} \sum_{i=1}^{n} t_i \tag{2.42}$$

is distributed as $F(2\gamma, 2\delta)$ with parameters

$$\begin{aligned} \gamma &= \frac{an(a(b-2)n + a + (b-1)^2)}{(b-1)(a+b-1)} \\ \delta &= \frac{a((b-2)n+2) + (b-1)b}{a+b-1} \\ c &= \frac{a\delta}{b\gamma} \end{aligned} \tag{2.43}$$

Proof. We apply Lemma 2 on t_i, which are $F(2a, 2b)$ distributed, therefore $\frac{a}{b} t_i \sim \beta'(a, b)$. Furthermore, the Beta-prime distribution is infinitely divisible and self-decomposable; specifically, this means that a sum of n i.i.d. Beta-prime distributions is also Beta-prime Distributed. See (Steutel and Harn 2003) (p.413) for more information. Since $T' \sim \beta'(\gamma, \delta)$, we can use the above result again and get that $T = \frac{\gamma}{\delta} T' \sim F(2\gamma, 2\delta)$, where we use that $a, b > 0$ implies that $\gamma, \delta > 0$ □

Let us now consider the independent multivariate circularly symmetric complex case.

Theorem 1. *Let $\boldsymbol{x}, \boldsymbol{x}_1, \ldots, \boldsymbol{x}_K \sim \mathcal{CN}(\boldsymbol{\mu}, \boldsymbol{\Gamma})$, with $\boldsymbol{\mu} \in \mathbb{C}^n$, $\boldsymbol{\Gamma} \in \mathbb{C}^{n \times n}$, $\boldsymbol{\Gamma}$ diagonal, and let*

$$\begin{aligned} \hat{\boldsymbol{\mu}} &\triangleq \frac{1}{K} \sum_{k=1}^{K} \boldsymbol{x}_k \\ [\boldsymbol{S}]_{i,j} &\triangleq \begin{cases} \frac{1}{K-1} \sum_{k=1}^{K} |[\boldsymbol{x}_k]_i - [\hat{\boldsymbol{\mu}}]_i|^2 & \text{for } i = j \\ 0 & \text{otherwise} \end{cases} \end{aligned} \tag{2.44}$$

and

$$T \triangleq c \frac{K}{K+1} (\boldsymbol{x}' - \hat{\boldsymbol{\mu}})^H \boldsymbol{S}^{-1} (\boldsymbol{x}' - \hat{\boldsymbol{\mu}}) \tag{2.45}$$

Then T has a $F(2\gamma, 2\delta)$ distribution. The parameters c, γ and δ are defined in Lemma 3

Proof. The statistic T can be written as a sum of n $F(2, 2K-2)$ random variables

$$T(\boldsymbol{x}, \boldsymbol{x}_1, \ldots, \boldsymbol{x}_k) = c\frac{K}{K+1}\sum_{i=1}^{n}\frac{|[\boldsymbol{x}]_i - [\hat{\boldsymbol{\mu}}]_i|^2}{\hat{s}_i^2} \tag{2.46}$$

since we assumed a diagonal covariance matrix. We now apply Lemma 1 to show that each term in the sum is $F(2, 2K-2)$ distributed. Finally we use Lemma 3 with $n = n$, $a = 1$, $b = K-1$ to show that the sum is also F-distributed $T \sim F(2\gamma, 2\delta)$. □

2.5 Detection theory

Since we are interested in detecting when something has changed, i.e. we want to know whether a sample $\boldsymbol{x}$ is from a known distribution $\mathcal{CN}(\boldsymbol{\mu}, \boldsymbol{\Gamma})$, using the estimated $\hat{\boldsymbol{\mu}}$ and $\boldsymbol{S}$ for comparison, or not. We can re-formulate the problem as a binary hypothesis testing problem. Where H_0 corresponds to the system is in its original state, and H_1 when the state has changed, e.g. a fault has been injected.

$$\begin{aligned} H_0 &: \boldsymbol{x} \sim \mathcal{CN}(\boldsymbol{\mu}, \boldsymbol{\Gamma}) \\ H_1 &: \boldsymbol{x} \nsim \mathcal{CN}(\boldsymbol{\mu}, \boldsymbol{\Gamma}) \end{aligned} \tag{2.47}$$

To discriminate between the two hypothesis we define the T-statistic as

$$T(\boldsymbol{x}, E_0) := c(\boldsymbol{x} - \hat{\boldsymbol{\mu}})^H \boldsymbol{S}^{-1}(\boldsymbol{x} - \hat{\boldsymbol{\mu}}) = c\frac{K}{K+1}\sum_{i=1}^{n}\frac{|[\boldsymbol{x}]_i - [\hat{\boldsymbol{\mu}}]_i|^2}{\hat{s}_i^2} \tag{2.48}$$

where the sample mean $\hat{\boldsymbol{\mu}}$ and sample variance $\boldsymbol{S}$ are estimated using the training data denoted $E_0 = \{\boldsymbol{x}_k : \boldsymbol{x}_k \sim \mathcal{CN}(\boldsymbol{\mu}, \boldsymbol{\Gamma})\}_{k=0}^{K-1}$. Furthermore, the T-statistic has a known F-distribution according to Theorem 1.
We reject H_0 if the statistic $T(\boldsymbol{x}, E_0)$ is larger than the detection threshold λ. And the test becomes: Reject H_0 for H_1 if

$$T(\boldsymbol{x}, E_0) \geq \lambda. \tag{2.49}$$

We now have a binary detector, so that for every sampled T we can make a decision whether the sample affirms or rejects the null hypothesis H_0. Instead of setting λ directly we can use the knowledge that the T-values are $F(2\gamma, 2\delta)$ distributed. By using the quantile function $F_{(2\gamma,2\delta)}(1-\alpha) = \inf\{t \in \mathbb{R} : \mathrm{P}(T(\boldsymbol{x}, E_0) \geq t) = \alpha\}$ we can set the detection limit $\lambda = F_{(2\gamma,2\delta)}(1-\alpha)$ so that the probability that $T(\boldsymbol{x}, E_0)$ is larger than λ is α. The detector now becomes:

$$\begin{aligned} H_0 &: \quad T(\boldsymbol{x}, E_0) < F_{(2\gamma,2\delta)}(1-\alpha) \\ H_1 &: \quad T(\boldsymbol{x}, E_0) \geq F_{(2\gamma,2\delta)}(1-\alpha) \end{aligned} \tag{2.50}$$

The performance of a binary detector can be characterised in several different ways. In principle there are four different cases:

1. The data $\boldsymbol{x}$ is from H_0 and the detector selects H_0: a true negative
2. The data $\boldsymbol{x}$ is from H_1 and the detector selects H_0: a false negative
3. The data $\boldsymbol{x}$ is from H_1 and the detector selects H_1: a true positive

4. The data $\boldsymbol{x}$ is from H_0 and the detector selects H_1: a false positive
These conditional probabilities are linked pairwise as

$$\begin{aligned} \mathrm{P}(T(\boldsymbol{x}, E_0) < \lambda | H_0) &= 1 - \mathrm{P}(T(\boldsymbol{x}, E_0) \geq \lambda | H_0) \\ \mathrm{P}(T(\boldsymbol{x}, E_0) < \lambda | H_1) &= 1 - \mathrm{P}(T(\boldsymbol{x}, E_0) \geq \lambda | H_1) \end{aligned} \tag{2.51}$$

Often a detector is described by the false positive rate $\mathrm{P}(T(\boldsymbol{x}, E_0) \geq \lambda | H_0)$ (FPR) which is also known as the probability of false alarm and the the true positive rate $\mathrm{P}(T(\boldsymbol{x}, E_0) \geq \lambda | H_1)$ (TPR). The parameter α in Equation (2.50) is therefore also the false positive rate. Another common way is to use the sensitivity = 1- FPR and the specificity = 1-TPR.
By using different frequency function estimation methods (LRM, ARX and ETFE) to calculate $\boldsymbol{x}$ from the the same data, we will get different but comparable detectors. For our use-case we expect to se orders of magnitude more samples that come from the H_0 hypothesis, i.e. the system is in its original state. Therefore, it is important to set α low enough that the detections (reject H_0) is not dominated by false positives. The false positive rate (FPR) of a detector with detection threshold λ is defined under the H_0 hypothesis:

$$\mathrm{FPR}(\lambda) = \mathrm{P}(T > \lambda | H_0) = \mathrm{P}(T > F_{(2\gamma, 2\delta)}(1 - \alpha)) = \alpha. \tag{2.52}$$

Thus, we can easily choose the false positive rate before any measurements are taken. Contrarily, the True Positive Rate (TPR) is defined under the H_1 hypothesis. Under H_1 the distribution of T is unknown, as it depends on the fault location and the severity of the fault; therefore, it can only be estimated using data.
One way to compare detectors is to use the same FPR (α) for all detectors being evaluated. One choice we call the Oracle detector chooses the smallest λ such that the estimated false positive rate is zero for the given training data.
Let $h_\lambda(G_0, E_0)$ count the number of positives for some data set $G_0 = \{\boldsymbol{x}_k : \boldsymbol{x}_k \sim \mathcal{CN}(\boldsymbol{\mu}, \Gamma)\}_{k=0}^{R-1}$ with detection threshold λ. If G_0 is a H_0 data set the estimated false positive rate will be conditional on E_0:

$$\hat{\mathrm{FPR}}(\lambda) = \frac{h_\lambda(G_0, E_0)}{R} \tag{2.53}$$

Furthermore, if $G_1 = \{\boldsymbol{x}_k : \boldsymbol{x}_k \nsim \mathcal{CN}(\boldsymbol{\mu}, \boldsymbol{\Gamma})\}_{k=0}^{M-1}$ is a H_1 data set the true positive rate can be estimated as

$$\hat{\mathrm{TPR}}(\lambda) = \frac{h_\lambda(G_1, E_0)}{M} \tag{2.54}$$

If estimating the $\hat{\mathrm{FPR}}$ using T-values calculated using the same training data E_0 but independent $\boldsymbol{x}$, we have estimated the false positive rate conditional to E_0.
If we instead assume that $\tilde{\boldsymbol{x}} \sim \mathcal{CN}(\boldsymbol{\mu}, \boldsymbol{\Gamma})$, with $\boldsymbol{\mu}$ and $\boldsymbol{\Gamma}$ known, we have that

$$\tilde{T}(\boldsymbol{x}) := c(\boldsymbol{x} - \boldsymbol{\mu})^H \boldsymbol{\Gamma}^{-1} (\boldsymbol{x} - \boldsymbol{\mu}) \sim \chi^2_{2mpq} \tag{2.55}$$

since it will simply be a sum of $2mpq$ squared i.i.d. Normal distributions.
We can now define some additional objects that are useful when comparing and analysing detectors. We can define the receiver operating characteristic curve (ROC) as the curve drawn by

$$(x, y) = (\hat{\mathrm{FPR}}(\lambda), \hat{\mathrm{TPR}}(\lambda)), \quad \lambda \in \mathbb{R}. \tag{2.56}$$

using some detector h. We note that the curve will always start at $(0, 0)$, be monotonically increasing and always end at (1,1). Furthermore, we call the area under the ROC the AUC:

$$\mathrm{AUC} = \int_0^1 \mathrm{TPR}(\mathrm{FPR}^{-1}(p))\mathrm{d}p. \tag{2.57}$$

From the properties of the ROC it is obvious that the value of AUC $\in [0, 1]$, where a value of one indicates a perfect detector, one half—one without predictive power, and zero—one that always makes the wrong choice.

3
Method

The detection method we will use is composed from the parts in the previous chapter: a frequency function estimate $\boldsymbol{x}$ that is calculated from a window of N samples using either LRM, ARX or ETFE, from this estimate the sample of T-statistic is calculated and compared to the detection threshold of the detector. Thereby, classifying the state of the vehicle at this point in time as either fault-free (H_0) or faulty (H_1). Finally, a set E_0 of frequency function estimates are used to calculate the parameters $\hat{\mu}$ and $\hat{S}$ in the statistical model.
This approach differs from change-point methods, such as S. Liu et al. (2013), because they are adaptive methods and will not catch slow changes to the system. Secondly, the method uses a non-parametric approach with an interpretable intermediary step (frequency function) that can give additional information of the location of the changed component. See Spilios D. Fassois and Fotis P. Kopsaftopoulos (2013) and F. P. Kopsaftopoulos and S. D. Fassois (2013) for parametric frequency function methods.

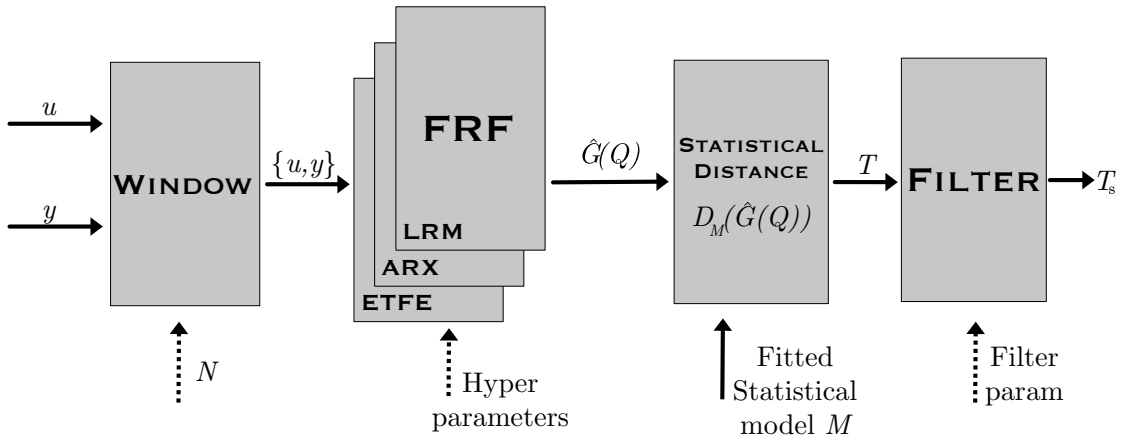

Figure 3.1: Parts of the proposed method.

To use the detector described in the the previous chapter there are multiple details to expand; an conceptual overview is given in Figure 3.1. Firstly, the m input signals and p output signals are sampled at a rate of f_s (Hz). They can be represented as the discrete signals $\boldsymbol{u}[n]$ and $\boldsymbol{y}[n]$ where n is a time-index. A frequency function estimate is calculated on N samples of the input and output signals $\{\boldsymbol{y}[n-i], \boldsymbol{u}[n-i]\}_{i=0}^{N-1}$ and estimated on the frequencies in the set $\mathcal{Q}$

$$\boldsymbol{x} = \left\{\hat{G}(\omega) : \omega \in \mathcal{Q}\right\} \tag{3.1}$$

where $\hat{G}(\omega)$ is estimated using either LRM, ARX or ETFE. The detector uses the LRM method, but the ARX and ETFE methods are used for comparison. The frequency function estimate $\boldsymbol{x}$, and the training data E_0 is used to calculate $T(\boldsymbol{x}, E_0)$ which is compared to the chosen detection threshold λ. The detector then either rejects H_0 or affirms it. This is then interpreted as the vehicle either having a mechanical fault or being fault-free.
The magnitude of the T-values encode how far the frequency function is from H_0 and original state. Large T-values are much more significant; furthermore, the cumulative density function (CDF) of the F-distribution can be used to get the likelihood of $\boldsymbol{x}$ given H_0. Since we are using windows with N samples which are sampled at f_s Hz, it takes N/f_s seconds to replace all samples in the window. To further improve the detector's sensitivity the T-values can be low-pass filtered, e.g. using a moving average filter as illustrated in Figure 3.1.
The choice of a normal distribution of the frequency function is motivated by (Kay 1993) and the following thought experiment. Assume that the output of the system is measured with an additive white normal noise term, i.e. let $v[n] \sim \mathcal{N}(0, \sigma_v^2)$ and

$$y[n] = \sum_{k=0}^{\infty} g(k)u[n-k] + v[n]. \tag{3.2}$$

After taking the DFT (of size N) on both sides we arrive at

$$\begin{aligned} Y[m] = G(\omega_m)U[m] + V[m] = G(\omega_m)U[m] + \sum_{k=0}^{N-1} v[k]e^{-j\frac{2\pi m}{N}k} \Leftrightarrow \\ \frac{Y[m]}{U[m]} = G(\omega_m) + \frac{V[m]}{U[m]} \end{aligned} \tag{3.3}$$

where the last term $V[m]$ is a linear combination normal distributed variables, which is also normally distributed. Note that the noise term is scaled by the inverse of the input. Therefore if the inputs are not sufficiently exited at a given frequency, the estimated frequency function may be dominated by noise at this frequency.
Deviations from the assumptions, of a linear system and the frequency function distribution being circularly symmetric complex normal with diagonal covariance, will reduce the sensitivity of the detector either due to correlations or larger than expected variations under hypothesis H_0. The variability will also increase from noise, unobserved inputs and non–observable system states. This will also mean that setting the detection threshold using the F-distribution will be too restrictive in some cases, which will result in a higher than expected false positive rate. The problem can easily be overcome using Bootstrap methods to calculate the detector threshold at a chosen false positive rate α, or by using T-values under H_0.

3.1 Frequency function

The codomain of the frequency function is the space of complex matrices $\mathbb{C}^{p\times m}$. Whereas, its domain is the frequencies $\mathcal{Q}$ which need to be chosen when defining

the detector. The frequency function estimate $\boldsymbol{x}$ is equivalent to the the estimate of the frequency function evaluated at $\mathcal{Q}$ and is used interchangeably:

$$\boldsymbol{x} = \left\{\hat{G}(\omega) : \omega \in \mathcal{Q}\right\} \tag{3.4}$$

Consider a sinusoidal signal with frequency f, by the Sampling theorem (Proakis and Manolakis 2007) it can only be unambiguously reconstructed if the sample rate $f_s > 2f$. Therefore for a sample rate of 1000 Hz we can only accurately reconstruct signals with frequency less than 500 Hz. Therefore, the frequency function should only be estimated below $f_s/2$ Hz.
Secondly, the physical properties of the system should to be taken in to account. Where are the modal frequencies of the mechanical structure? In a car the important modal frequencies are bellow 100 Hz; therefore, we can further prune the frequency interval. The frequencies in the set $\mathcal{Q}$ can be arbitrary, but usually, for simplicity, they are a subset of the DFT frequencies

$$\mathcal{Q} \subseteq \left\{\omega_m = \frac{2\pi m}{N}\right\}_{m=0}^{N-1}.$$

The normalised frequencies ω (rad/sample) can be converted to the analog frequencies as $f = \omega f_s/(2\pi)$. A choice used in the thesis are the first 26 frequencies of the DFT of length 256. At a sample rate of 1000 Hz, they are equally spaced from zero to 100 Hz.

$$\left\{\frac{if_s}{256}\right\}_{i=1}^{26} \tag{3.5}$$

3.2 Statistical model

The statistical model M is defined using estimated values of $\boldsymbol{\mu}$ and $\boldsymbol{\Gamma}$ that are found during a training phase $E_0 = \{\boldsymbol{x}_k : \boldsymbol{x}_x \sim \mathcal{CN}(\boldsymbol{\mu}, \boldsymbol{\Gamma})\}_{k=0}^{K-1}$, where $\boldsymbol{x}_k$ is collected during window k. Furthermore, assuming that each window has length N and are independent. We can estimate the sample mean $\hat{\mu}$ and sample covariance $\hat{S}$ using Equation (2.44) and reproduced here:

$$\begin{aligned}
\hat{\boldsymbol{\mu}} &\triangleq \frac{1}{K}\sum_{k=1}^{K}\boldsymbol{x}_k \\
[\boldsymbol{S}]_{i,j} &\triangleq \begin{cases} \frac{1}{K-1}\sum_{k=1}^{K}|[\boldsymbol{x}_k]_i - [\hat{\boldsymbol{\mu}}]_i|^2 & \text{for } i = j \\ 0 & \text{otherwise} \end{cases}
\end{aligned}$$

The T-value is also a random variable that depends both on the random variable $\boldsymbol{x}$ and the K random variables in E_0. The T-value is defined in Equation (2.48)

$$T(\boldsymbol{x}, E_0) := k(\boldsymbol{x} - \hat{\boldsymbol{\mu}})^H \boldsymbol{S}^{-1}(\boldsymbol{x} - \hat{\boldsymbol{\mu}}) \sim F(2\gamma, 2\delta);$$

furthermore, is distributed as a F-distribution according to Theorem 1.

3.3 LRM, ARX and ETFE estimators and their hyper-parameters

The frequency function is estimated using one of the three methods LRM, ARX and ETFE. The ARX and ETFE methods are included as comparative methods. The ARX model (MIMO) is a commonly used parametric model in System Identification (Söderström and Stoica 1989) and is widely used in the change-point detection literature Michèle Basseville and Nikiforov (1993); Yamanishi and Takeuchi (2002); F. P. Kopsaftopoulos and S. D. Fassois (2013). And for estimating the frequency function (Proakis and Manolakis 2007). The ARX method is parametric since the it assumes a global structure on the frequency function, as defined in Equation (2.22). The ARX method's hyper-parameter is the ARX model order that governs how many past inputs and outputs are used to estimate the current output of the system. We chose to investigate the ARX method with hyper-parameters in the range 2–29, to cover a wide range of values.
The SISO ETFE method is easily derived from the literature e.g. (Proakis and Manolakis (2007) p.326) and (Ljung 1999). Expanding it to the MIMO case is trivial. However, estimating the (cross) power density spectrum is more involved. The commonly used periodogram estimate is not consistent, i.e. it does not converge to the true spectrum (Proakis and Manolakis 2007). The three classical non-parametric methods to estimate the power density spectrum are the Bartlett method, the Welch method (Welch 1967) and the Blackman and Turkey method. They all work by averaging the power density of multiple shorter sequences each with length N_{ETFE} taken from the window of size N. According to Proakis and Manolakis (2007) the methods perform similarly. The Welch method was chosen since the python package scipy routine CSD used this method.
The DTFT of a signal on a finite window, can be analysed using the DFT. Let $x[n]$ be a sufficiently well behaved signal, and we are interested in analysing the behaviour of the DFT. Since the DFT operates on a finite sequence, it will be equivalent to analysing it using a window function $w[n]$ (Proakis and Manolakis (2007) p. 963). Our new signal $\tilde{x}[n]$ is defined as

$$\tilde{x}[n] = x[n]w[n] = \begin{cases} x[n], & 0 \leq n \leq N-1 \\ 0, & \text{otherwise} \end{cases} \tag{3.6}$$

Moving to the frequency domain using the DTFT we have that $\tilde{X}(\omega) = W(\omega) * X(\omega)$ where the frequency domain of the sampled signal is the convolution between the original signal and the windowing function $W(\omega)$. The presence of the windowing function causes sidelobes and smearing of the original power spectrum which is known as spectral leakage (Proakis and Manolakis 2007). This problem can be ameliorated by choosing windowing functions with better properties than the rectangular window. The rectangular window (also known as `boxcar`) has the highest frequency resolution but also very large spectral leakage. Better and common choices are the Hanning-window (`hann`) which has reasonably low spectral leakage. The Kaiser 14 window is recommended by the maintainers of scipy as a good general purpose window. The flat-top (`flattop`) window is used when the amplitude of the signal is

most important. See Heinzel, Rüdiger, and Schilling (2002) and Solomon (1991) for a deeper treatment of windowing functions.
The LRM method works by estimating a rational function in the neighbourhood of each frequency. The size of the neighbourhood we call the bandwidth and is be controlled by the parameter N_w, and can be converted to analog frequencies as $(2N_w + 1)f_s/N$ (Hz). The LRM method sets a lower bound on N_w, in Equation (2.20), so that the least-squares fitting of the multiple input single output (MISO) rational function has a unique solution. The second parameter n_{LRM} is the degree of the local rational function.

4
Results

4.1 Vehicle tests at Hällered Proving ground

Several measurement segments were collected from an instrumented light vehicle (Volvo XC60). Segments were collected when the vehicle drove over several road surfaces namely 'Belgian Pavé', Patched Asphalt' and regular smooth asphalt, and with different states of fault introduced. One training set (E_0) of windows without faults was put aside and used to fit the nominal model M according to Section 3.2, for each road surface. The remaining segments where used to calculate T-values for segments with and without faults. Only the detector using the LRM-based frequency function estimate was used on this data set.

Instrumentation Triaxial accelerometers, with sample rate of 1 kHz, where fitted to the following places in the vehicle as output channels

- Front part of subframe; left, right and mid (9 channels)
- Front Strut Tower; left and right (6 channels)
- Driver Seat rail (3 channels)
- Damper fork, vertical only; left and right (2 channels)
- Rear part of subframe, center (3 channels)

The following sensors where used as input channels

- Front wheel knuckle joint, left and right (6 channels)

Fault The car was modified so that the air pressure in the front left air suspension could be controlled by a valve during operation of the vehicle. This allowed creating measurement segments characterised by faults that appear both gradually and abruptly. The valve could be opened releasing the air pressure either slowly or quickly. Closing the valve restored the pressure in the suspension.

Detector parameters The accelerometer channels where split into input and output channels. The left and right knuckle joint channels (a total of six channels) where chosen as the inputs since vibrations from the road travel through them before reaching other parts of the vehicle. The remaining 23 channels where taken as outputs signals from the system. From discussions with engineers at Volvo Cars the frequency region of interest are the low frequencies as they correspond to the important modal frequencies of the system of rigid bodies. Therefore, we chose to estimate the frequency function in the interval 0 to 100 Hz. Twenty-six equally spaced frequencies where chosen based on the FFT of length 256, see Equation (3.5).

The analysis window size was chosen as $N = 4096$, which approximately corresponds to a 4 seconds long measurement window. The number of frequency points and the measurement window was judged to have a good balance.

We note that at each frequency the frequency function is a complex matrix of shape 23×6. In all the mechanical state is described by 3588 complex values. The statistical model of the baseline state M has $26 = 3588$ complex values corresponding to the mean of the frequency function at every frequency; furthermore it has 3588 real valued variables corresponding to the variance of the frequency function. The mean and variance are calculated according to Equation (2.44).

The hyper-parameters used with the LRM estimator where $n = 3$ and $N_w = 30$. The choice fell on these after analysing the detector quality in Results 4.2.

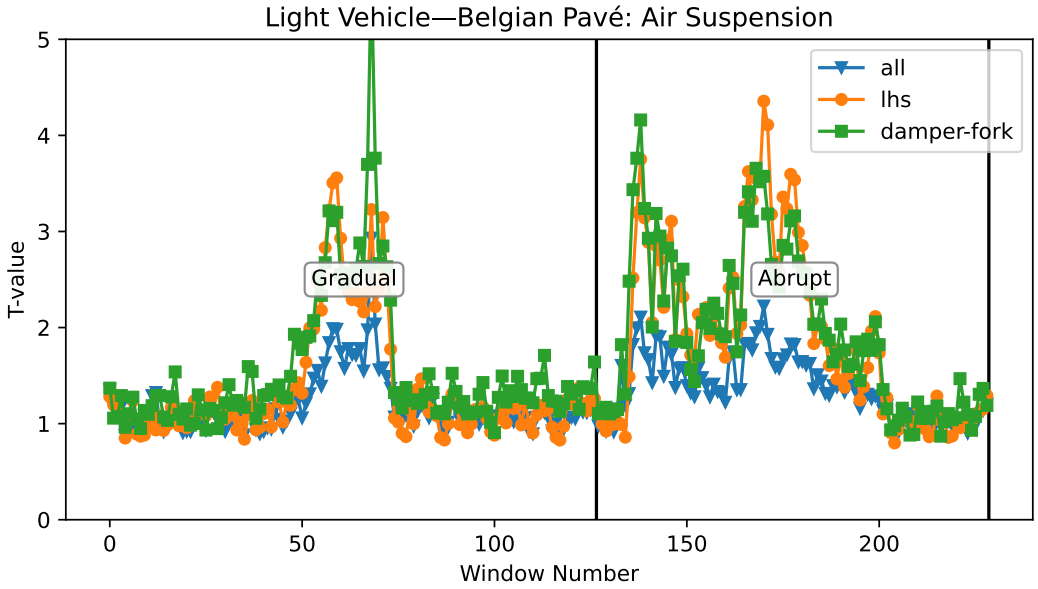

Figure 4.1: Plot of the T values for two segments driven on Belgian Pavé. Gradual: gradual introduction of fault in air suspension; Abrupt: abrupt introduction of fault. Window size: $N = 4096$.

Training phase The statistical model M for the Belgian Pavé was fitted on 28 independent frequency function estimates, each being an interval of 4096 data points from the baseline, corresponding to an length of about 4 seconds. The baseline data was sampled when driving on a Belgian Pavé obstacle on the Hällered proving ground; furthermore, the data presented in the plots where also collected at the same obstacle (and same car) but later during the day. The Patched asphalt model was fitted on 33 independent frequency function estimates using the same interval size. The data was collected at the Patched Asphalt obstacle at Hällered proving ground. The regular asphalt model used 21 independent estimates with the same interval size. Each frequency function estimate took about one half of an second to calculate on a modern laptop, well bellow the interval length of 4 seconds.

Results In the following graphs we have plotted the calculated T-values on a XC60 driving over the different road surfaces. A nominal model is fitted for each road surface. The calculated T-values are plotted for three different sets of channels. The `all`-set include all channels. The `lhs`-set include the sensors front left *Strut Tower*, front left *Subframe* and left *Damper Fork* in total seven channels as outputs and the sensor at left *knuckle joint* (three channels) as inputs. The `damper-fork`-set include the *Damper Fork* (2 channels) channels as outputs and the inputs are all six knuckle joint channels.

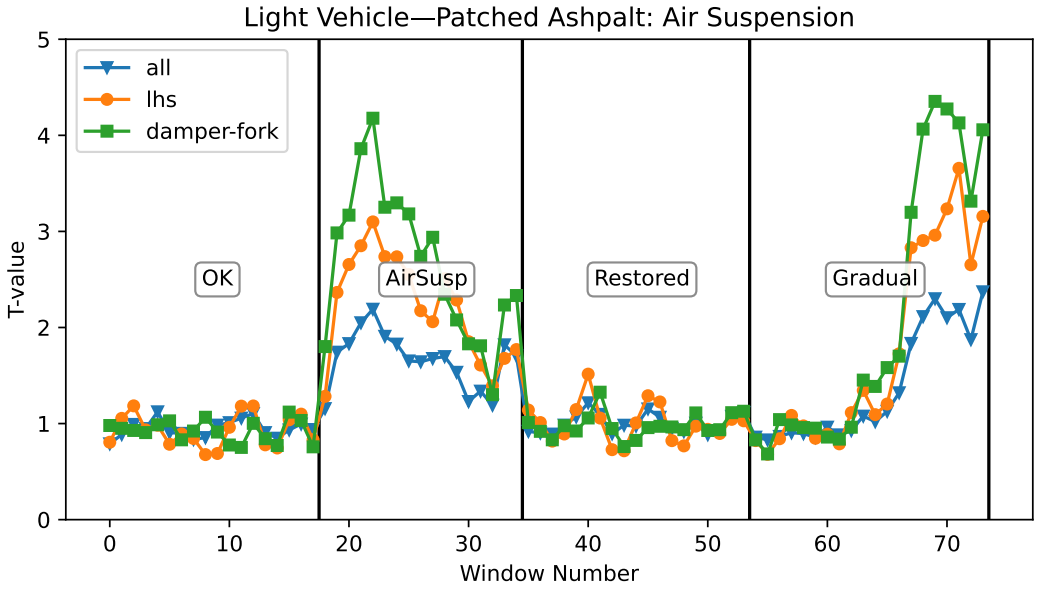

Figure 4.2: Plot of the T-values from segments on Patched Asphalt. OK: segment with no faults; AirSusp: fault in air suspension; Restored: state after fault restored; Gradual: gradual introduction of fault in air suspension. Window size: $N = 4096$

The results from when the vehicle was driven over Belgian Pavé is presented in Figure 4.1. The air was first released gradually from the suspension and then restored to its original state. Then the air was released abruptly and restored again.
We note that both before and after the two events the T-values lie in the range $[.8, 1.5]$. When the error is slowly introduced we see that the T-values gradually start to rise above the previous range. For the full set of channels (`all`) the new range is about $[1.5, 2]$, clearly above the error-free range. When looking at the channels on the left-hand side (`lhs`) and those around the damper-fork the T-values take on more extreme values closer to 4. Several other channel subsets where created, but they where not reported here as they behaved similarly to `all`. We note that the Change introduced was letting out air in the front-left suspension.
In Figure 4.2 the setup is the same as reported in Figure 4.1, except that the road surface was switched to patched asphalt. Again the the T-values for the original state is around one, and the range of the T-value with the state change is roughly $[2, 4]$. We see similar results for the channel subsets `lhs` and `damper-fork`.
Finally, in Figure 4.3 the same setup is again used as in Figure 4.1, but the road surface is now regular asphalt. The range of T during the original state is also

around $[.8, 1.5]$; whereas, the range with the changed state is about $[1.1, 2.6]$. It is less than on the previous road surfaces but still significant.

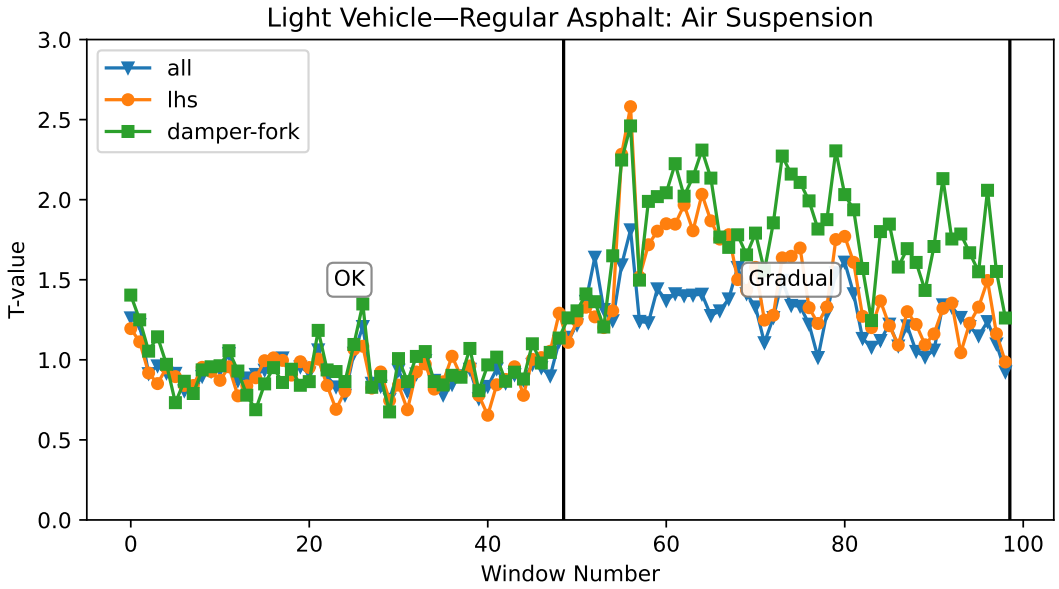

Figure 4.3: Plot of the T-values from segments on regular asphalt. OK: segment with no faults; Gradual: gradual introduction of faults in air suspension.

Clearly, the method works well for detecting errors for a diverse range of road surfaces. By eyeballing the signals, a limit can easily be chosen for an almost perfect detector. The results from when the vehicle was driven over Patched Asphalt show that the differences between the T-values calculated from the original state (H_0) and the changed state (H_1) data sets are smaller than when driving over Belgian Pavé.

4.2 Comparison of Estimation Methods

In the previous section the results for a specific parameterisation of the LRM method where presented. The goal here is to present a comparison between the different frequency function estimation methods and hyper-parameterisations of them. Therefore, instead of plotting the calculated T-values when the system is in its original state (H_0) and in its changed state (H_1), the result figures are split into two parts. The upper subfigure shows the 25^{th}, 50^{th} and 75^{th} quantiles of the T-value as the edges of coloured boxes. When the system is in its original state the line and boxes are coloured green, and when the system's state has changed the colour is orange red.
In the lower subfigure plots the AUC value and the TPR of the Oracle detector for each hyper-parameter choice of the estimation methods. They were calculated using Equations (2.56) and (2.57). The AUC is represented by the grey area, and the Oracle TPR as the red line. The hyper-parameterisations were chosen to cover the a range of reasonable choices. With the application in mind it is clear that the detector must have a low false-positive rate as an alarm will halt the operation of the vehicle.

4.2.1 Multi-Body Simulations XC90

A state of the art Multi-Body simulation system with roughly 2000 degrees of freedom was used to simulate the behaviour of a Volvo XC90 during different types of mechanical faults. The speed of the simulated car was around 40 km/h, two more passes where made at 36 km/h and 44 km/h ($\pm 10\%$). The simulations with vehicle speeds 36 km/h and 44 km/h were used to train the statistical model M. Whereas, the simulation at 40 km/h and the simulations with introduced faults where used to calculate the T-values.

Instrumentation The positioning of the sensors was based on capturing as much of the vehicle movements while still being able to place the sensor there on a real car. The choice fell on 4 symmetrical points on the front sub-frame of the vehicle denoted A-D and illustrated in Figure 4.4, and the front wheel centers. At those points the acceleration in the forward and lateral direction, as they were more significant than the vertical acceleration, was sampled at 1000 Hz. The Multi-Body simulation has high fidelity for frequency components below 100 Hz.

- Front wheel centers, left and right (4 channels)
- Subframe, points A-D (8 channels)

Faults Two faults where investigated, the first was a loose ball joint at the front left knuckle joint, point E in Figure 4.4. It was modelled as a bushing element with bi-linear translational stiffness and without rotational stiffness. The second fault was a degradation in a front left-side bushing, marked E in Figure 4.4. The stiffness was reduced to 75%, 50% and 25% of its original values in three different simulations.

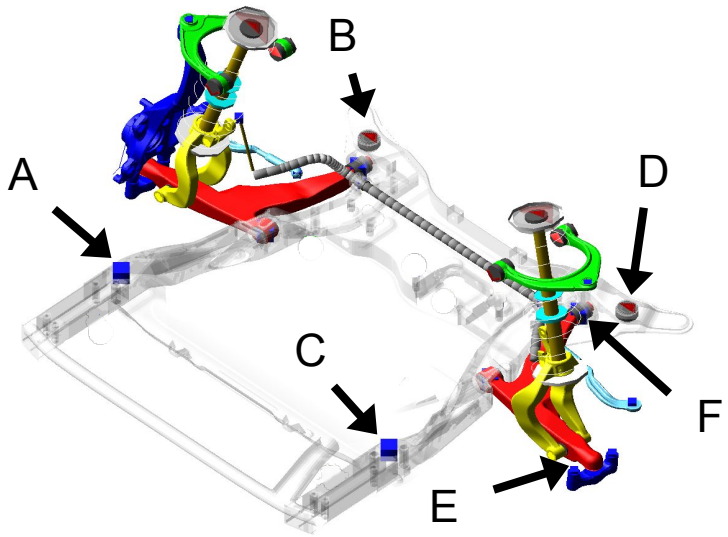

Figure 4.4: Placement of the four measurement points A-D, measuring acceleration in the forward and lateral directions. The two faults are the loose ball joint at E, and the damaged bushing at point F.

Detector parameters The four channels from the front wheel centers where chosen as the inputs to the system. The remaining eight channels from the sub-frame where the outputs. The frequency function is estimated at the 26 equally spaced frequencies less than 100 Hz, see Equation (3.5). The interval was chosen due to limitations in the simulation and more importantly the majority of the modal frequencies lie in this range. At each frequency the frequency function is a 8×4 matrix.
The size of the analysis window was one parameter that we chose to investigate its impact. The window sizes 512 (1/2 s), 1024 (1 s), 2048 (2 s) and 8192 (8 s) samples where chosen to span a wide range of window sizes.
The ETFE methods hyper-parameters that where varied was the internal window length n_{ETFE} and the windowing function used when estimating the cross-spectral density $\Phi_{xy}(\omega)$. The windowing functions come from thp python package Scipy, `boxcar` corresponds to the standard rectangular window, `hann` is the commonly used hann-window, `flattop` is useful for estimating the amplitude accurately (Heinzel, Rüdiger, and Schilling 2002), and `kaiser`14 is another commonly used windowing function.
The ARX model order (n_{ARX}) was varied from 2 to 29. The LRM-method's hyper-parameters the order of the local polynomial n_{LRM} varied from two to six, with the parameter being N_w the minimum allowed or double that according to Equation (2.20).

4.2.2 Investigating the window size N

In this experiment we chose to investigate the effect on the sample window size N that is used to estimate the frequency function. The fault chosen to illustrate the effect is the bushing fault with 25% remaining stiffness, a moderately difficult

fault to detect. The only difference is the length of the sample window N. When increasing the sample window N the ETFE method can accommodate larger internal windowing functions (n_{ETFE}). The results for window sizes 512, 2048 and 8192 are shown here, the remaining are in the appendix.

Results

In general an increase in the window size will result in improvements of the detector and this held true for all methods. In Figure 4.5 the window size is 512 samples. At this length (1/2 s) the calculated T-values from the original and with a bushing fault are practically indiscernible by every metric and for every hyper-parameterisation of the estimators. In the upper figure the distributions lie on top of each other, the major difference is the maximum T-value of the original state. The AUC hovers around 1/2 and the Oracle TPR is zero or close to it, i.e. the detectors are not performing better than random chance.
When we increase the window size to 2 seconds (2048 samples) in Figure 4.5, we see that the T-values for the changed system has risen significantly. The AUC values lie around .6, which is still very poor for detectors, but better than before. Further increasing the window size to 8192 samples in Figure 4.7, we start to see some spread in the detectors. We first note that the LRM method with N_w with double the theoretical minimum consistently perform the best for most choices of the local order n_{LRM}, it is only when the order becomes larger that 5 that the Oracle TPR falls to low values. Otherwise the LRM method consistently outperforms the other methods in that metric. Especially the parameterisation $n_{\text{LRM}} = 3$ and $N_w = 40$ that has a AUC around .975 and an Oracle TPR of around .70, which is significantly better than all other methods and parameterisations. The ETFE methods come second with fair performance with internal window sizes 256, and 512. The ARX method is significantly more variable, with low order (n_{ARX}) performing the best, but still worse that the ETFE methods. The hyper-parameterisation $n_{\text{ARX}} = 4$ is a close third when looking at the AUC metric, but is only a third of the second best Oracle True Positive Rate.

4.2.3 Averaging of T-values

To further improve performance at the expense of the speed the detector detects changes, one can average several T-values in a moving average filter. Here we averaged the T-values from the previous experiment with window size 8192 with an moving average of 10 denoted MA(10) in Figure 4.8.

Results

After applying the moving average to the detectors from Figure 4.7, the detectors' AUC and Oracle TPR values increased, as presented in Figure 4.8, regardless of the previous values; i.e. the best detectors improved similarly in absolute values to those with lower Oracle TPR values. This resulted in one hyper-parameter choice ($N_w = 40$, $n_{\text{LRM}} = 3$) being a perfect detector with an AUC and Oracle detector's

TPR value of one. The other LRM methods also show large improvement as does the ETFE and ARX methods.

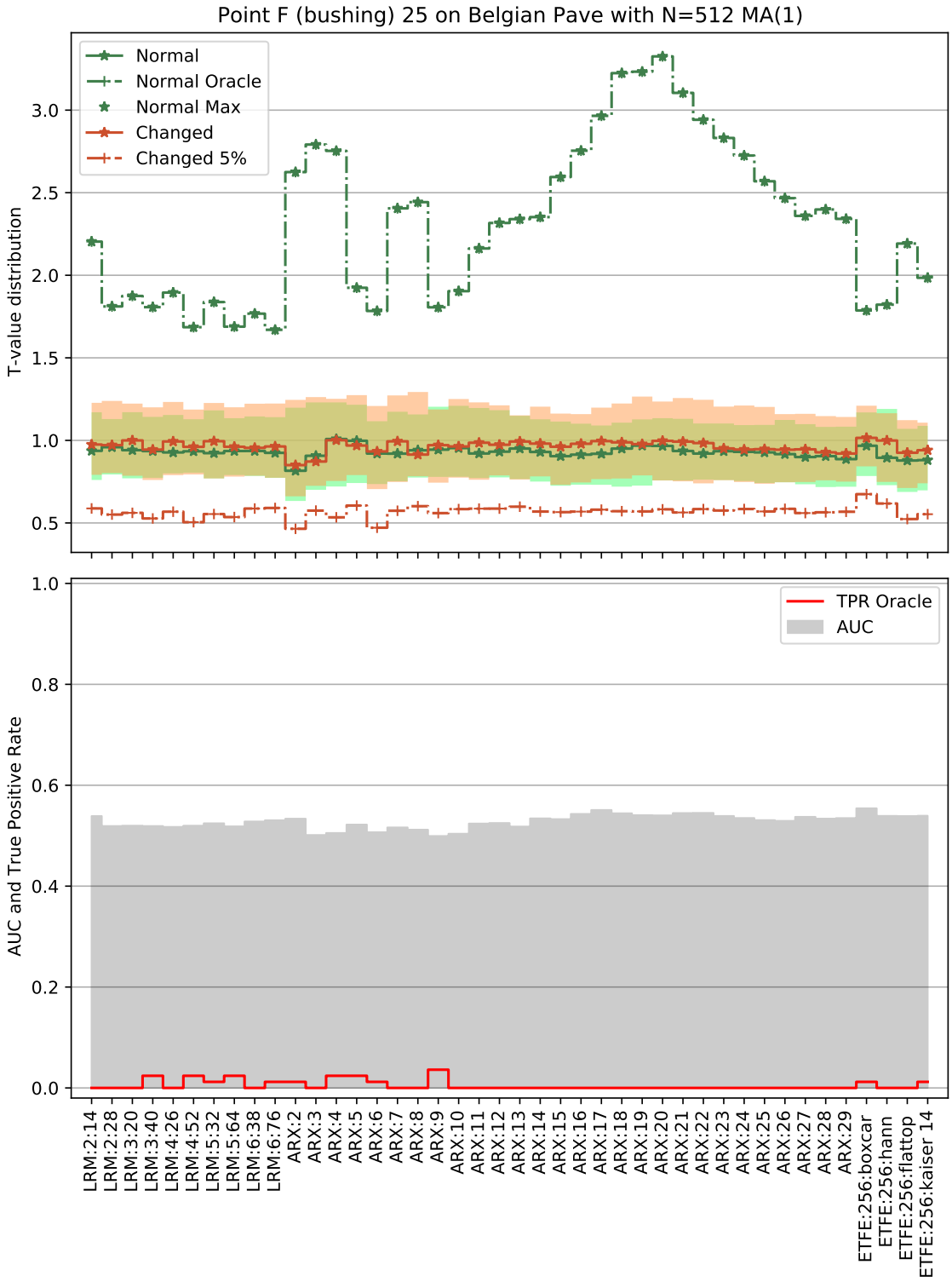

Figure 4.5: MBS simulation with fault being a bushing with 25% remaining stiffnes, using a window size of 512 samples.

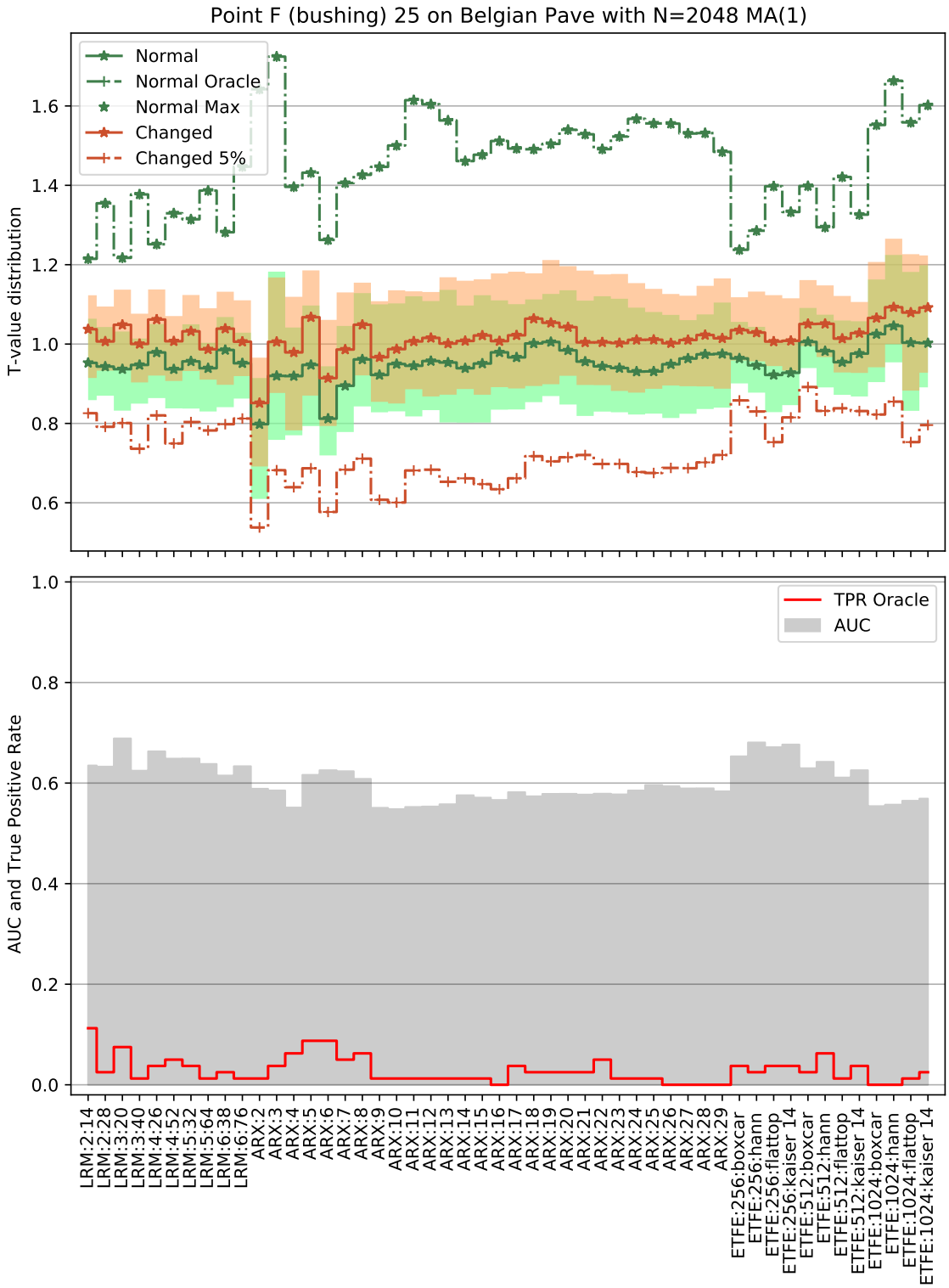

Figure 4.6: MBS simulation with fault being a bushing with 25% remaining stiffnes, using a window size of 2048 samples.

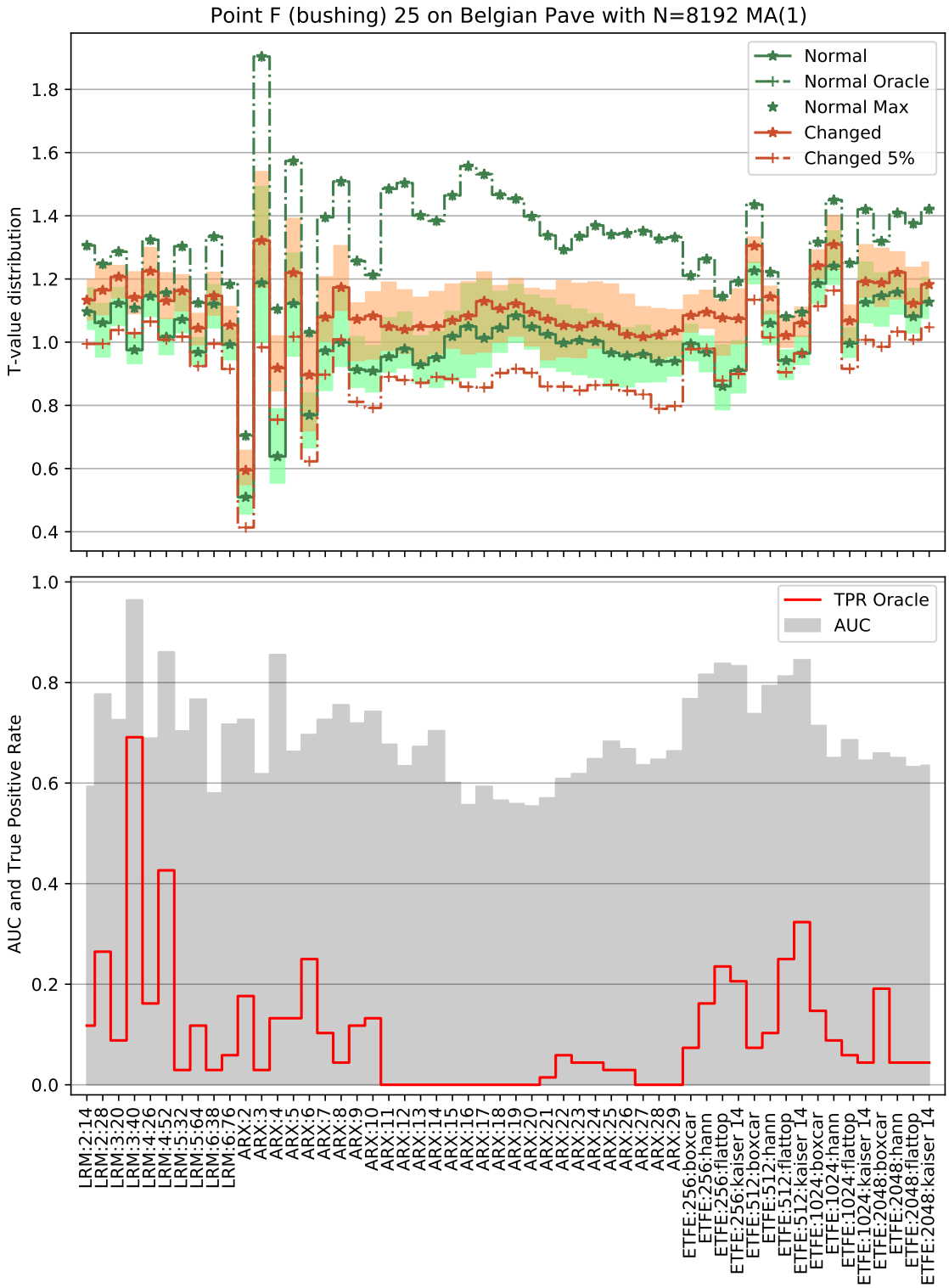

Figure 4.7: MBS simulation with fault being a bushing with 25% remaining stiffnes, using a window size of 8192 samples.

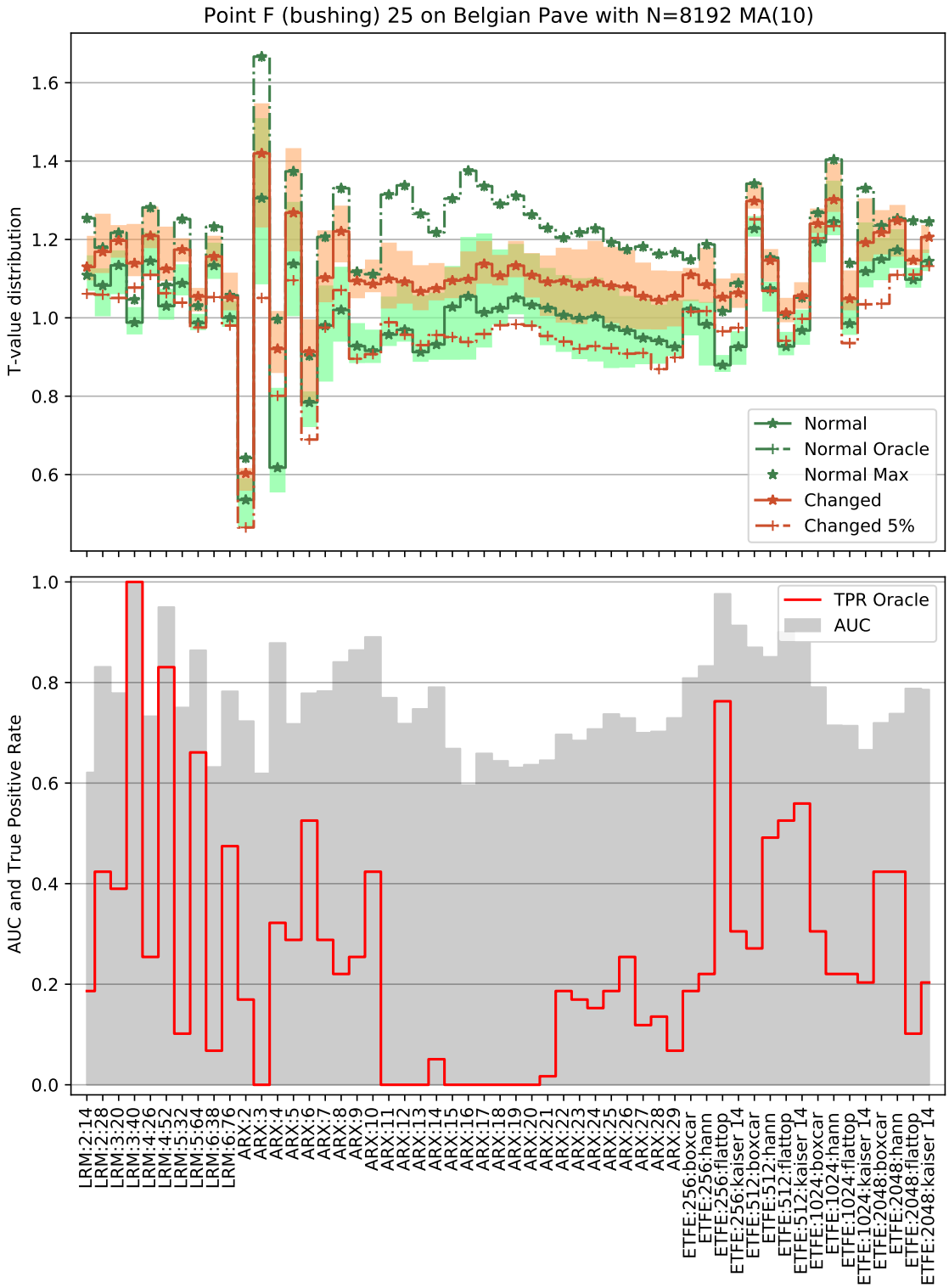

Figure 4.8: 75% degradation in bushing F, in the MBS simulated data set with window size N=8192, with a moving average of 10.

4.2.4 Window size of knuckle joint

We continue the investigation on how the window size influences the detectors by changing the fault to the knuckle joint explained earlier. The results are presented for window sizes 1024 and 2048. Detectors on window sizes shorter or longer either perform poorly or there is little differentiation between the methods and hyper-parameterisations.

Results

The first result is presented in Figure 4.9 where the window size is 1024. There we see that the LRM method performs consistently the best for N_w double the the minimum value, and the local polynomial order n_{LRM} lower than five. This is especially clear in the Oracle TPR values which are among the best. The AUC values of all the hyper-parameterisations the LRM method have consistently the highest values. The ARX method has some hyper-parameterisations, namely model order (n_{ARX}) eight and nine, that are equally good as the LRM hyper-parameterisations. However, the other choices of n_{ARX} have a maximum value of the T-values under the original (H_0) state, that results in poor values of the Oracle TPR. The AUC values are also a few tenths lower than the LRM values. The ETFE method also performs fair, without much difference in the hyper-parameter choices, except that shorter internal windows n_{ETFE} perform better. Generally, better than a random ARX, but significantly worse that the best methods (LRM and ARX).
After increasing the window size to 2048 and keeping everything else the same, the performance of all methods have improved significantly. There is not much variation in the different LRM methods, they all have the consistently highest AUC values and on par with the best of the ARX method ($n_{\text{ARX}} = 9$) and the best ETFE hyper parameterisations ($n_{\text{ETFE}} = 256$) and windowing methods `boxcar` and `hann`. We note that the best windowing methods are different than when analysing the bushing fault. The Oracle TPR reinforces the AUC results where the LRM method performs consistent and at the top, whereas select hyper-parameterisations of ARX and ETFE perform equally well.

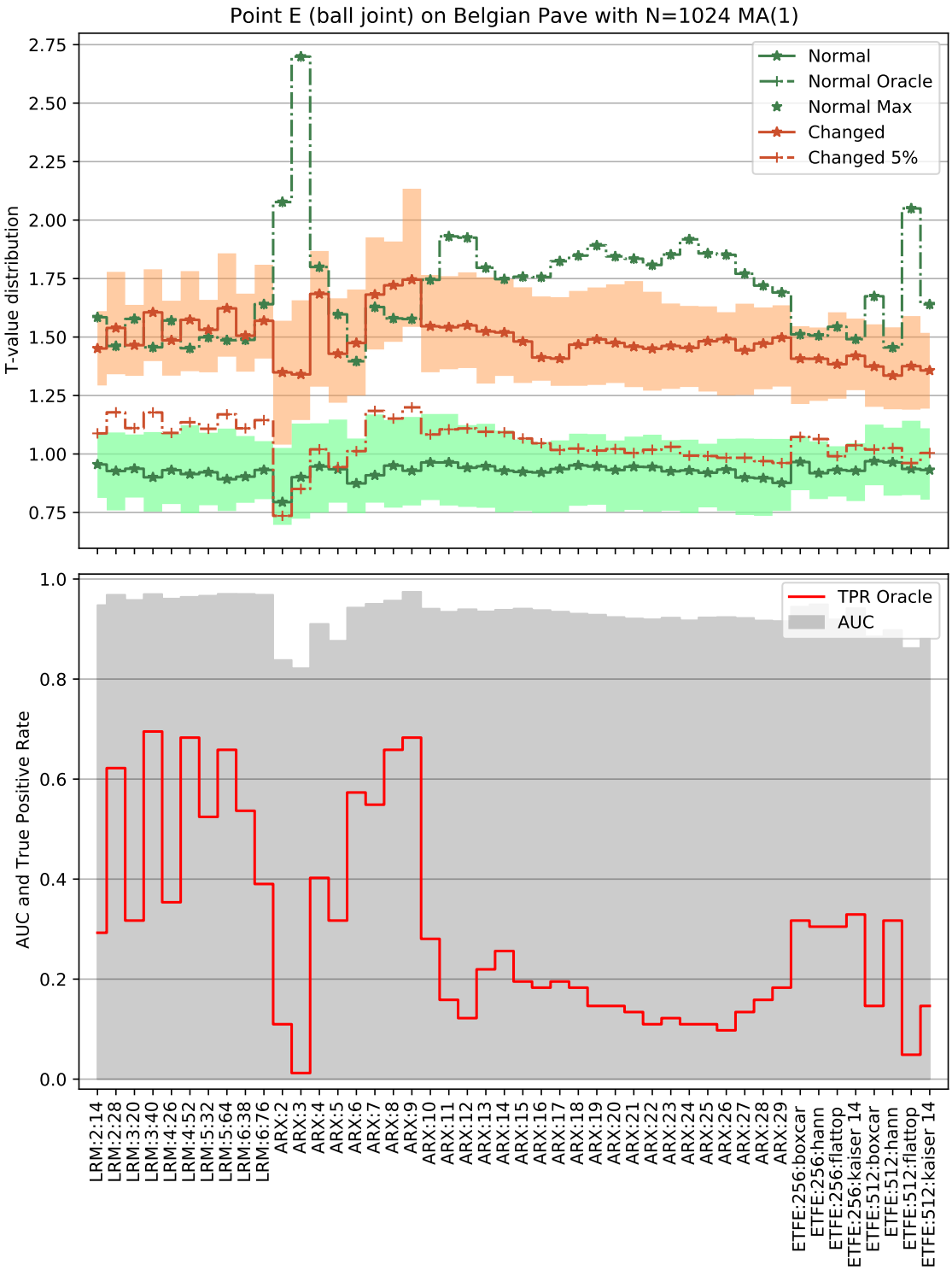
Point E (ball joint) on Belgian Pave with N=1024 MA(1)
T-value distribution
Normal
Normal Oracle
Normal Max
Changed
Changed 5%
AUC and True Positive Rate
TPR Oracle
AUC
LRM:2:14
LRM:2:28
LRM:3:20
LRM:3:40
LRM:4:26
LRM:4:52
LRM:5:32
LRM:5:64
LRM:6:38
LRM:6:76
ARX:2
ARX:3
ARX:4
ARX:5
ARX:6
ARX:7
ARX:8
ARX:9
ARX:10
ARX:11
ARX:12
ARX:13
ARX:14
ARX:15
ARX:16
ARX:17
ARX:18
ARX:19
ARX:20
ARX:21
ARX:22
ARX:23
ARX:24
ARX:25
ARX:26
ARX:27
ARX:28
ARX:29
ETFE:256:boxcar
ETFE:256:hann
ETFE:256:flattop
ETFE:256:kaiser 14
ETFE:512:boxcar
ETFE:512:hann
ETFE:512:flattop
ETFE:512:kaiser 14

Figure 4.9

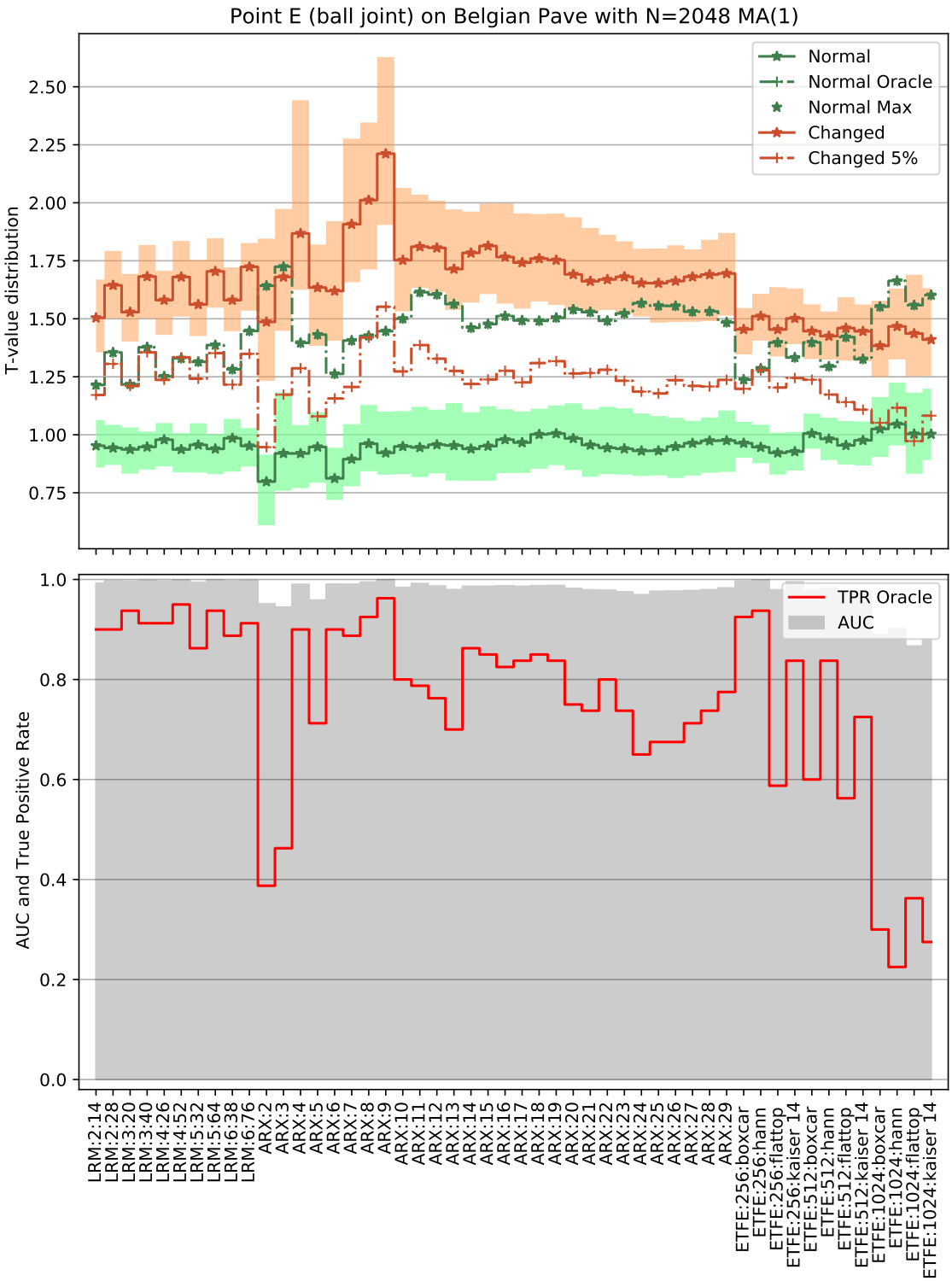
Point E (ball joint) on Belgian Pave with N=2048 MA(1)
Normal
Normal Oracle
Normal Max
Changed
Changed 5%
T-value distribution
2.50
2.25
2.00
1.75
1.50
1.25
1.00
0.75
TPR Oracle
AUC
AUC and True Positive Rate
1.0
0.8
0.6
0.4
0.2
0.0
LRM:2:14
LRM:2:28
LRM:3:20
LRM:3:40
LRM:4:26
LRM:4:52
LRM:5:32
LRM:5:64
LRM:6:38
LRM:6:76
ARX:2
ARX:3
ARX:4
ARX:5
ARX:6
ARX:7
ARX:8
ARX:9
ARX:10
ARX:11
ARX:12
ARX:13
ARX:14
ARX:15
ARX:16
ARX:17
ARX:18
ARX:19
ARX:20
ARX:21
ARX:22
ARX:23
ARX:24
ARX:25
ARX:26
ARX:27
ARX:28
ARX:29
ETFE:256:boxcar
ETFE:256:hann
ETFE:256:flattop
ETFE:256:kaiser 14
ETFE:512:boxcar
ETFE:512:hann
ETFE:512:flattop
ETFE:512:kaiser 14
ETFE:1024:boxcar
ETFE:1024:hann
ETFE:1024:flattop
ETFE:1024:kaiser 14

Figure 4.10

4.3 Investigating behaviour of the LRM hyper-parameter N_w LRM

The LRM method has two hyper-parameters, the order of the local polynomial denoted n_{LRM} and the local window size N_w. The local window size N_w is defined in Equation (2.18) and counts the number of frequency bins above and below the chosen frequency where the frequency function is estimated. The LRM method uses the DFT of the input and output signals to fit the local rational model. As N_w counts the number of frequency bins whose width is given by

$$f_{\text{res}} = \frac{f_s}{N}. \tag{4.1}$$

By doubling the the window size N, the bin width is halved (Heinzel, Rüdiger, and Schilling 2002). Therefore, when doubling the window size N the local window size N_w can also be doubled to keep the same bandwidth when using the LRM method. In Figures 4.7, 4.8 and 4.9, we see that the AUC and Oracle TPR drops significantly when the N_w parameter takes on a small value.
In Figure 4.7 the LRM method with hyper-parameterisation $n_{\text{LRM}} = 3$, $N_w = 20$ has a bandwidth of 5 Hz, a AUC value of .75 and a Oracle TPR of about .1. However, when doubling the bandwidth to 10 Hz, both the AUC and the Oracle TPR increase to .975 and .65 respectively. Which makes this the best performing detector. The fault analysed is the bushing fault with 25% remaining stiffness and window sizes of 4096 and 8192 samples, and $n_{\text{LRM}} = 3$ is kept constant while N_w is changed. We note that the spacing between the frequency function estimates is about 3.9 Hz, see Equation (3.5).

Results

When the window size is 4096, the LRM method reaches its first maximum of the AUC and Oracle TPR with values of .78 and .32 respectively around $N_w = 21$ as shown in Figure 4.11. This corresponds to roughly twice the minimum possible value of N_w and a bandwidth of 10 Hz. Further increasing the local window size (N_w) the Oracle TPR oscillates some but in never reaches those values again, before flattening out just above zero. The AUC reaches its maximum again around when N_w is 40 and 51, before smoothing out to a value around .7.
Increasing the window size to 8192 samples in Figure 4.12, the AUC and Oracle TPR reaches its maximum value at roughly the double the value of N_w, but still around the same bandwidth of 10 Hz. But the maximum values of the AUC and Oracle TPR have increased to .97 and .78 respectively. We also note that the peak is quite wide with bandwidths between 8.7 and 11.7 still being significantly better than the others. Further increases of N_w slightly lower the AUC, whereas the Oracle TPR is reduced significantly more. If we compare these values to the ARX and the ETFE estimators in Figure 4.7, we see that if we choose N_w reasonably large we will almost certainly choose an estimator that will perform better—with respect to AUC and Oracle TPR—than the best ARX an ETFE method.

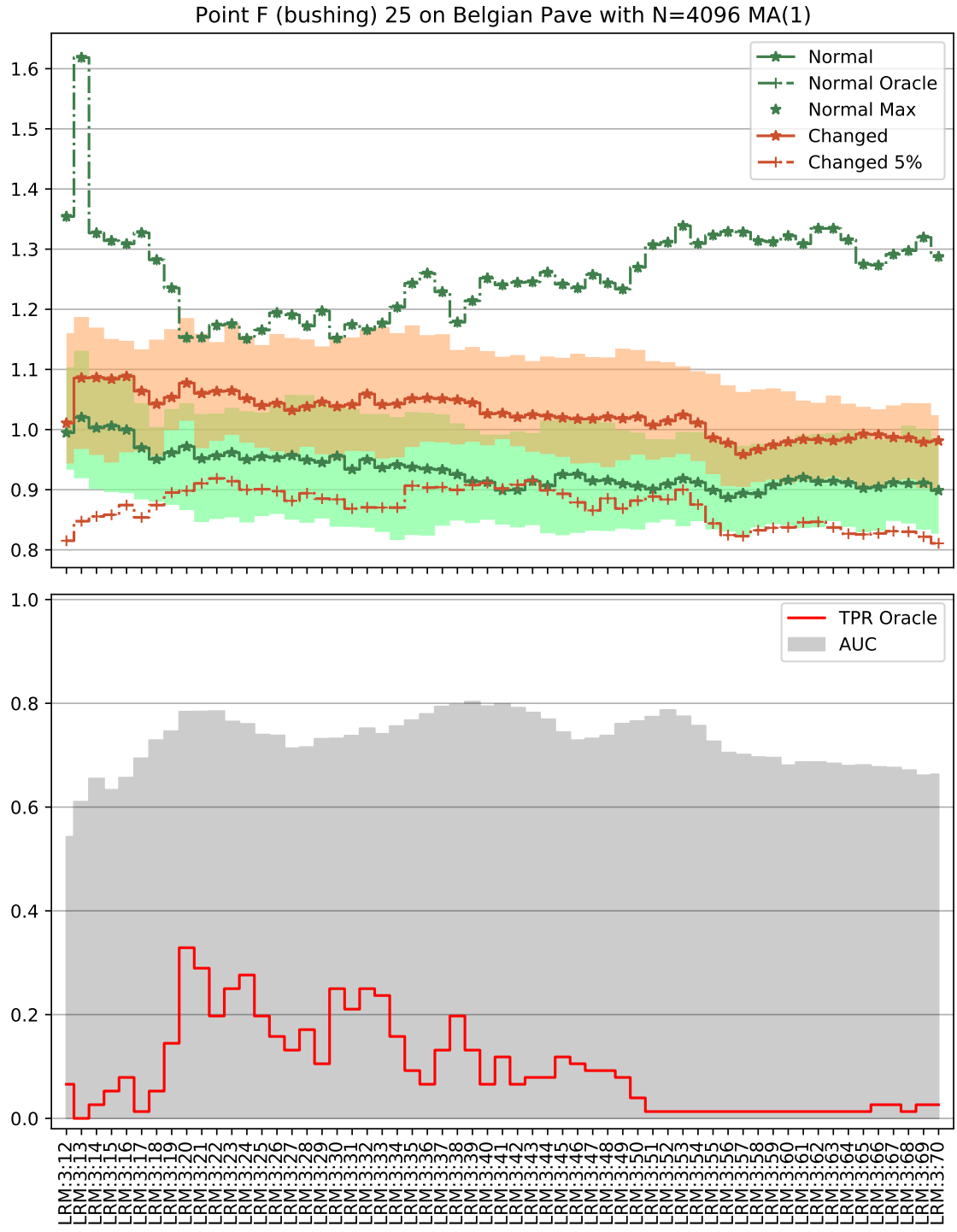

Figure 4.11: MBS simulated data on Belgian Pave comparing error free with Bushing F at 25 % stiffness. Results when varying N_w: between 12 and 70, using the LRM method with $n_{\text{LRM}} = 3$ fixed and a window size of 4096.

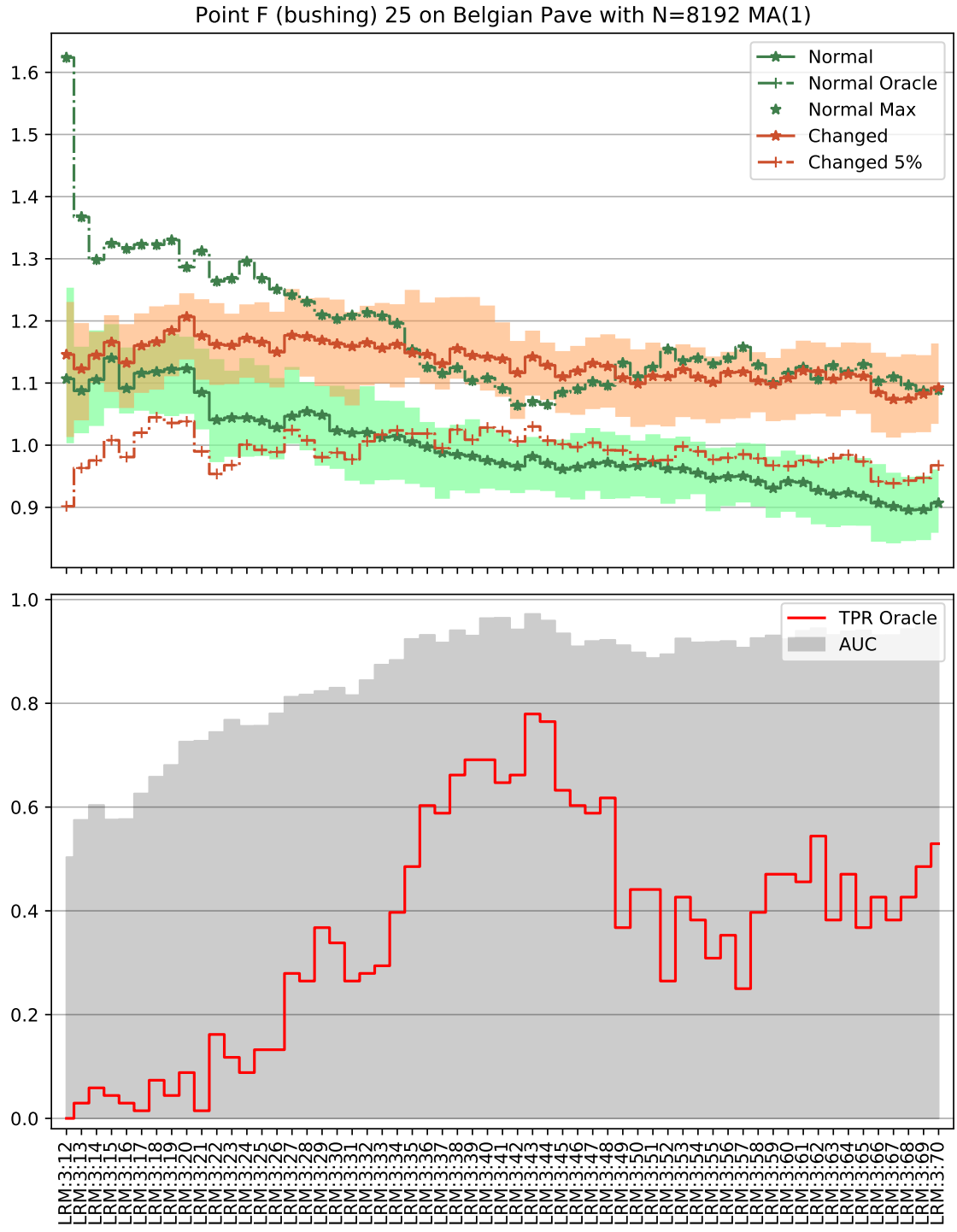

Figure 4.12: MBS simulated data on Belgian Pave showin Bushing F at 25 % stiffness. Results when varying N_w: between 12 and 70, using the LRM method with $n_{\text{LRM}} = 3$ fixed and a window size of 8192.

Figure 4.13: Picture of the measuring setup in the lab, whence the measurements where taken from.

4.4 Vehicle life-cycle test

This data set was collected from one of Volvo Cars life-cycle tests where a front damper failed unexpectedly during the test cycle. Three segments, each roughly 46 seconds long, were collected early in the test before the damper failed were deemed being in the original state (H_0). Three more segments were collected after the damper failed and became the changed (H_1) data. The life-cycle test was performed in a lab where a Volvo XC60 was mounted by its wheel hubs to a hydraulic test rig that simulate simulate driving. During this test it was simulating driving over Belgian Pavé.

Instrumentation Four accelerometers where mounted in the corners of the cars frame, four more where placed in the four wheel hubs. They measured acceleration in only the vertical direction and where sampled at a rate of 512 Hz.

- Front frame, left and right (2)
- Rear frame, left and right (2)
- Front wheel hubs, left and right (2)
- Rear wheel hubs, left and right (2)

Fault During the life-cycle test one of the front dampers failed unexpectedly.

Detector Parameters The system was defined with the four wheel hub channels as the inputs and the remaining four channels from the subframe as the outputs. Again the frequencies of interest are the low modal frequencies, and the frequency function was estimated at 26 equally spaced frequencies between 2 and 52 Hz according to

$$\mathcal{Q} = \left\{ \frac{i f_s}{256} \right\}_{i=1}^{26} \approx \{2, 4, \ldots, 50, 52\} \text{ Hz} \quad \text{at } f_s = 512 \text{ Hz} \tag{4.2}$$

where each value of the frequency function is a 4×4 matrix.
The results for window size 512 samples (1 s) is presented here, the results for longer windows is omitted since the detectors performed too well, e.g. see Figure A.43 in the Appendix.

Training phase The statistical model M was fitted using 72 frequency function estimates taken from two of the three early segments (H_0). The last segment in the original state was used to calculate the H_0 T-values and the remaining three changed segments to calculate the H_1 T-values.

Results In this experiment the LRM and ARX methods performed similarly; both having very high AUC and high Oracle TPR values. The results are presented in Figure 4.14. There were three perfect detectors; namely, ARX methods with order three, four and five. They also had by far the largest separation between the T-values from the data sets H_0 and H_1. Most of the hyper-parameterisations less that $n_{\text{ARX}} \leq 20$ performed on par with the LRM methods', whose AUC lie around .98 and Oracle TPR of .87. The ETFE methods performed poorly in comparison, but using the `flattop` and `kaiser(14)` windowing functions made the ETFE perform somewhat better.

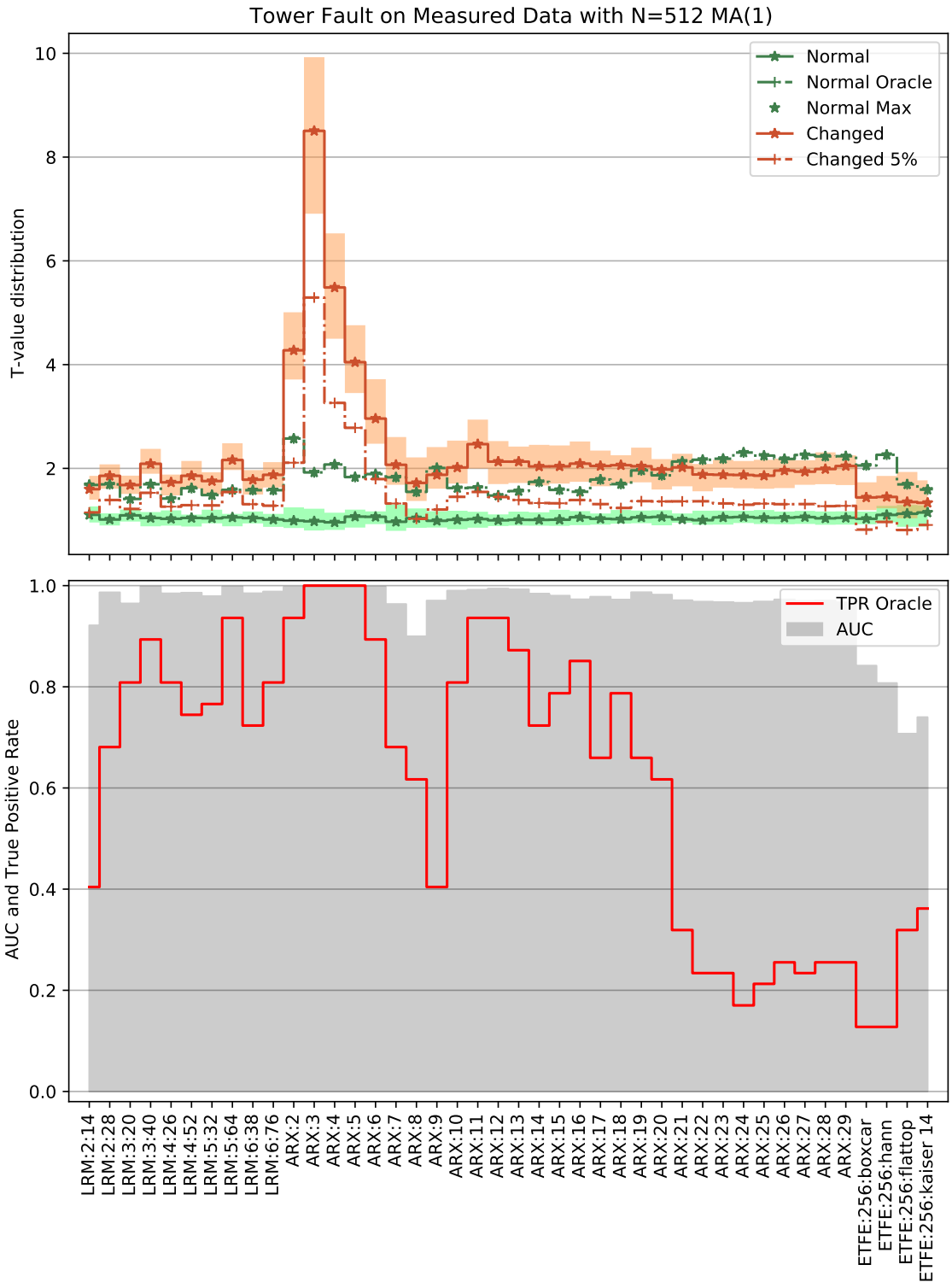

Figure 4.14: Plot of the T-values, AUC and Oracle TPR collected in a lab from a Volvo XC60, for a wide range of hyper-parameterisations of the LRM, ARX and ETFE methods.

5

Conclusion and Discussion

5.1 Summary

The detection method investigated in this thesis works well in most cases, the only exception is when the change is subtile which is the case for the bushing with a small degradation. Furthermore, the type of excitation matters less than expected. In Section 4.1 we investigated how different road surfaces influence the detection model. Driving over Belgian Pavé is an uneven and bumpy ride, ensuring that there is a lot of energy to excite the system. The two road surfaces Belgian Pavé and Patched Asphalt in Section 4.1 have H_1 T-values about two to four times the ones from the original system. Compared to when driving over Regular Asphalt in the same setup those T-values are only about one and a half to two times larger. However, the spread of the T-values in the original system is less than when driving over either Patched Asphalt and Belgian Pavé. The reasons are likely three-fold; firstly, some changes in the system happen at regions that is not excited much when driving over regular asphalt; secondly, the operating region when driving over regular asphalt is smaller and should be more linear than when driving over Belgian Pavé; lastly, the noise term $V[m]$ is higher since the input excitation is small, see Equation (3.3) for a brief treatment.

The results from Section 4.2.2 and 4.2.4 showed that increasing the window size N improved all detectors. The LRM detectors seemed to improve more on average then the ARX and ETFE detectors, but the best ARX hyper-parameterisation usually performed similarly. By increasing the window size N enough it seems to be possible to get a good detector for most faults. The fault bushing with 75% remaining stiffness resisted detection even with the window size at 8192 (8s) samples. Further increases in the window size was not possible due to the limited data available.

The LRM method seems to be robust with respect to the hyper-parameter choices as long as sensible choices are made around the local model order n_{LRM} and bandwidth parameter N_w. Local model order of three to five performed the best with order three often outperforming all other detectors. This is a reasonable choice since we are using the estimated local rational function to improve the estimate at one frequency and not the surrounding frequencies. It also ties closely to the bandwidth parameter N_w which determines the size of the region to fit the local rational model. It is similar to a smoothing problem in which the bandwidth and local model order are closely coupled. In Section 4.3 we saw that the best performing bandwidth with $n_{\text{LRM}} = 3$ is roughly 10 Hz that is $N_w = 21$ when the window size is 4096 samples and $N_w = 43$ when it is 8192 samples. We also note that the detector performance

is not that sensitive to the N_w parameter ± 5. In the bushing experiment with 25% remaining stiffness at $N = 8192$, the LRM detectors with $N_w = 43 \pm 5$ (Figure 4.12) by far outperform all the ARX and ETFE detectors (Figure 4.7).

The LRM method also performs preferable to the ARX and ETFE methods in that the best (analysed) hyper-parameterisations does not change when changing the faults, window size or even the experimental setup. In all results the LRM method with hyper-parameterisation $n_{\text{LRM}} = 3$ and $N_w = 40$ performed the best or among the best. Of course, as Section 4.3 showed the detector can be fine-tuned to perform better. On that data set the best performing detector had $N_w = 43$. The ARX method showed much more dependence on the model order n_{ARX}, which is reasonable since it controls the degrees of freedom in the frequency function. In the experiment with the bushing at 25% stiffness (Section 4.2.2) the best ARX detectors had model orders of five or six, whereas for the knuckle joint (Section 4.2.4) the best where in the range six to nine. Lastly, in Section 4.4 (life-cycle test) the best performing detectors had model orders two to six. The same argument can be made for the ETFE method where in the bushing experiment and the life-cycle test the best used either a flat-top or a kaiser window and local window size (N_{ETFE}) of 256 or 512. In the ball-joint experiment the rectangular window (`boxcar`) and the Hann-window performed the best, also with a local window size of 256.

5.2 Discussion

Choice of input and output signals

The treatment of how to choose the optimal input and output signals has not been given much weight in this thesis. Mainly, because we wanted a general and easy to use sensor setup; therefore, we tried to place the sensors in strategic positions so we would capture the major mechanical behaviour of the vehicle. This meant using the wheel centers, or points close by as inputs since the input vibrations from the road will travel there first. The output sensors were mainly placed on the subframe, a major structural component, or other easy to reach places in the vehicle. If we assume that the vehicle can be represented as a LTI-system

$$\begin{aligned} \boldsymbol{x}[n+1] &= \boldsymbol{A}\boldsymbol{x}[n] + \boldsymbol{B}\boldsymbol{u}[n] \\ \boldsymbol{y}[n] &= \boldsymbol{C}\boldsymbol{x}[n] + \boldsymbol{D}\boldsymbol{u}[n] + \boldsymbol{v}[n] \end{aligned}$$

then the choice of input and output signals is equivalent to choosing the matrices $\boldsymbol{B}$, $\boldsymbol{C}$ and $\boldsymbol{D}$, which influence the controllability and observability of the system and limits the precision and accuracy of any reconstruction of the system (Kailath 1980). However, as we saw in the Results the method works well for the different systems and choices of input and output signals.

For a deeper treatment of placing sensors optimally the article M. Basseville, A. Benveniste, Moustakides, et al. (1987) is a good start.

Statistical model

The distribution of the frequency function $G(\omega)$ is assumed to be Normally distributed and independent in both frequency and the elements of the matrix $G(\omega)$. This is a very strong assumption especially with respect to the ARX model where the parameter A and B are fitted in time domain and then the frequency response is then calculated as

$$[G_{\text{ARX}}(\omega)]_i = \frac{\sum_{l=0}^{n_{\text{ARX}}} \boldsymbol{B}_{i,l} e^{-j\omega l}}{\sum_{l=1}^{n_{\text{ARX}}} A_{i,l} e^{-j\omega l}}.$$

The LRM model also suffers from correlation between the estimated frequency points since the surrounding points are used to fit the rational function. This might be a smaller problem than expected since the modal frequencies of the system gives most of the relevant information when performing damage detection (Doebling et al. (1996);M. Basseville, A. Benveniste, Gach-Devauchelle, et al. (1993)).
For examples changes in the modal frequencies will often have large effect since small changes of the modal frequency can have a large impact on the estimated frequency function.
If we would like to include correlations in the frequency dimension then we can use the estimated covariance $\boldsymbol{S}$ on the training data. If we continue using the T-statistic from this article we are interested in the estimated precision matrix $\boldsymbol{S}^{-1}$ rather than the covariance matrix. There are robust methods for estimating the precision matrix in high-dimensional data settings see for example Cai, W. Liu, and Luo (2011) and Öllerer and Croux (2015).
If we instead would like to compare the prior distribution to the present distribution there are several ways forward. It is straight forward to use either the Hellinger distance or the Kullback-Liebler divergence under a Normality assumption. These metrics have a simple closed form solution involving the covariance matrices. However, if the number of samples is again small compared to the dimension, the sample covariance may be poorly conditioned or even singular. There are covariance estimators such as the Optimal Linear Shrinkage (Ledoit and Wolf 2004) that perform well even when the sample size is small.
We also note that instead of the raw signals we can see the frequency function estimate as a new signal; we can then use change-point methods such as the *cumulative sum* (Michèle Basseville and Nikiforov 1993) or a *relative density* method from e.g. S. Liu et al. (2013) to perform the change detection. We simply note that the frequency function estimate is simply a transformation from the input and output signal space to the space of discrete frequency response functions, which encodes desirable properties of the system.
Secondly, the Normality assumption is probably too restrictive due to heavy tails in the frequency function distribution. If the detection limit set by Equation (2.50) is too restrictive, one can use data from when the system is in its original state (H_0) to collect T-values which can then be used to set the new detector limit λ.

Notes on Computational Complexity

The majority of the computational cost when calculating each T-value lies in the frequency function estimate. The three frequency function estimates all have differ-

ent complexities. The ETFE method is dominated by the repeated application of the Fast Fourier Transform which has a log-linear complexity with respect to the window size.
In the ARX method for each output channel we solve a least-squares problem with $c = (m + 1)n_{\text{ARX}}$ parameters and $N - n_{\text{ARX}}$ observations for p output channels; therefore, the complexity of the ARX method is $\mathcal{O}(p(N - n_{\text{ARX}})c^2)$.
The LRM method also solves a least squares problem for each output channel, but also for each frequency $\omega \in \mathcal{Q}$; the least squares problem has $c = (n_{\text{LRM}}+1)(m+1)+ n_{\text{LRM}}$ parameters and N_w observations. A unique property of the LRM method's complexity is the linear complexity on the number of frequencies $|\mathcal{Q}|$; $\mathcal{O}(|\mathcal{Q}|pN_wc^2)$.
In the investigated cases the LRM method performed significantly faster than the ARX method, in the MBS data set with $N = 8192$ the LRM method took on average 100 ms to calculate one T-value, compare this to the ARX 1000 ms and the ETFE 40 ms. Reducing the window size to $N = 2048$ the LRM method took 100 ms, the ARX method took 400 ms and the ETFE method took on average 20 ms to calculate one T-value. Therefore, when using longer windows the LRM method scales with the number of frequencies in $\mathcal{Q}$ rather than the window size N. This is a major benefit since the number of frequencies is often much fewer than the window size. In these experiments the $\mathcal{Q}$ has had 26 elements compared to the 8192 samples in the most often used window size N.

5.3 Conclusion

The results show that the detector is able to detect the injected faults under a multitude of conditions; such as different road surfaces, injected faults and sensor placements; thereby, showing a robustness of the detector. Furthermore, the LRM method, used to estimate the frequency function, is the best performing (with the ARX method) and the most robust to hyper-parameter choices; additionally, the computational complexity of the LRM method is favourable compared to the ARX method, and is dominated by a linear scaling in the number of frequencies in $\mathcal{Q}$. Experimental results show that the LRM-based method computes T-values significantly faster than the ARX-based method, allowing for online-systems with quick sampling rates of the system state.
The global T-value is a good indicator whether something has changed in the system; although, it does not confer much information about the location of the change, it can be rectified by analysing T-values calculated from subsets of the input and output channels. The subset T-values, as shown in Section 4.1, close to the fault are often larger and more prominent than less relevant subsets and the global T-value; thereby, narrowing down the location of the fault.
Since the detector uses a training period to learn the behaviour of the system the necessary requirements, of a working detector on a new vehicle, are sensible sensor placements and a computer with an implemented detector.

Bibliography

Adams, Ryan Prescott and David J. C. MacKay (2007). *Bayesian Online Changepoint Detection*. arXiv: 0710.3742 [stat.ML].

Alcala, Carlos F. and S. Joe Qin (2009). "Reconstruction-Based Contribution for Process Monitoring". In: *Automatica* 45.7, pp. 1593–1600. DOI: 10.1016/j.automatica.2009.02.027. URL: https://doi.org/10.1016/j.automatica.2009.02.027.

Basseville, M., A. Benveniste, B. Gach-Devauchelle, et al. (1993). "In Situ Damage Monitoring in Vibration Mechanics: Diagnostics and Predictive Maintenance". In: *Mechanical Systems and Signal Processing* 7.5, pp. 401–423. DOI: 10.1006/mssp.1993.1023. URL: https://doi.org/10.1006/mssp.1993.1023.

Basseville, M., A. Benveniste, G. Moustakides, et al. (1987). "Optimal Sensor Location for Detecting Changes in Dynamical Behavior". In: *IEEE Transactions on Automatic Control* 32.12, pp. 1067–1075. DOI: 10.1109/tac.1987.1104501. URL: https://doi.org/10.1109/tac.1987.1104501.

Basseville, Michèle, Albert Benveniste, et al. (2006). "Subspace-Based Algorithms for Structural Identification, Damage Detection, and Sensor Data Fusion". In: *EURASIP Journal on Advances in Signal Processing* 2007.1, p. 069136. DOI: 10.1155/2007/69136. URL: https://doi.org/10.1155/2007/69136.

Basseville, Michèle and Igor V. Nikiforov (1993). *Detection of Abrupt Changes: Theory and Application*. Prentice-Hall.

Brincker, Rune and Carlos E. Ventura (2015). "Time Domain Identification". In: *Introduction to Operational Modal Analysis*. John Wiley & Sons, Ltd. Chap. 9, pp. 239–260. ISBN: 9781118535141. DOI: https://doi.org/10.1002/9781118535141.ch9. eprint: https://onlinelibrary.wiley.com/doi/pdf/10.1002/9781118535141.ch9. URL: https://onlinelibrary.wiley.com/doi/abs/10.1002/9781118535141.ch9.

Cai, Tony, Weidong Liu, and Xi Luo (2011). "A Constrained ℓ_1 minimization Approach To Sparse Precision Matrix Estimation". In: *Journal of the American Statistical Association* 106.494, pp. 594–607. DOI: 10.1198/jasa.2011.tm10155. URL: https://doi.org/10.1198/jasa.2011.tm10155.

Doebling, S.W. et al. (May 1996). "Damage identification and health monitoring of structural and mechanical systems from changes in their vibration characteristics: A literature review". In: DOI: 10.2172/249299. URL: http://dx.doi.org/10.2172/249299.

Fassois, Spilios D. and Fotis P. Kopsaftopoulos (2013). "Statistical Time Series Methods for Vibration Based Structural Health Monitoring". In: *CISM International Centre for Mechanical Sciences, Courses and Lectures*. Vol. 542, pp. 209–264. DOI:

10.1007/978-3-7091-1390-5_4. URL: http://link.springer.com/10.1007/978-3-7091-1390-5%7B%5C_%7D4.

Garnett, R. et al. (2010). "Sequential Bayesian Prediction in the Presence of Changepoints and Faults". In: *The Computer Journal* 53.9, pp. 1430–1446. DOI: 10.1093/comjnl/bxq003. URL: https://doi.org/10.1093/comjnl/bxq003.

Grimmett, G and D Stirzaker (2001). *Probability and random processes*. 3rd. Oxford: Oxford University Press.

Gustafsson, F. (1996). "The Marginalized Likelihood Ratio Test for Detecting Abrupt Changes". In: *IEEE Transactions on Automatic Control* 41.1, pp. 66–78. DOI: 10.1109/9.481608. URL: https://doi.org/10.1109/9.481608.

– (2007). "Statistical Signal Processing Approaches To Fault Detection". In: *Annual Reviews in Control* 31.1, pp. 41–54. DOI: 10.1016/j.arcontrol.2007.02.004. URL: https://doi.org/10.1016/j.arcontrol.2007.02.004.

Heinzel, Gerhard, Albrecht Rüdiger, and Roland Schilling (2002). "Spectrum and spectral density estimation by the Discrete Fourier transform (DFT), including a comprehensive list of window functions and some new at-top windows". In: URL: http://hdl.handle.net/11858/00-001M-0000-0013-557A-5.

Idé, Tsuyoshi and Koji Tsuda (Apr. 2007). "Change-Point Detection using Krylov Subspace Learning". In: *Proceedings of the 2007 SIAM International Conference on Data Mining*, nil. DOI: 10.1137/1.9781611972771.54. URL: https://doi.org/10.1137/1.9781611972771.54.

Johnson, Richard Arnold and Dean W. Wichern (2002). *Applied multivariate statistical analysis*. 6th ed. Prentice hall Upper Saddle River, NJ.

Johnson, Timothy J and Douglas E Adams (Sept. 2002). "Transmissibility as a Differential Indicator of Structural Damage". In: *Journal of Vibration and Acoustics* 124.4, pp. 634–641. ISSN: 1048-9002. DOI: 10.1115/1.1500744. URL: https://doi.org/10.1115/1.1500744.

Kailath, T (1980). *Linear Systems*. Englewood Cliffs, New Jersey: Prentice-Hall.

Kawahara, Yoshinobu and Masashi Sugiyama (2012). "Sequential Change-Point Detection Based on Direct Density-Ratio Estimation". In: *Statistical Analysis and Data Mining* 5.2, pp. 114–127. DOI: 10.1002/sam.10124. URL: https://doi.org/10.1002/sam.10124.

Kawahara, Yoshinobu, Takehisa Yairi, and Kazuo Machida (Oct. 2007). "Change-Point Detection in Time-Series Data Based on Subspace Identification". In: *Seventh IEEE International Conference on Data Mining (ICDM 2007)*, pp. 559–564. DOI: 10.1109/icdm.2007.78. URL: https://doi.org/10.1109/icdm.2007.78.

Kay, S M (1993). *Fundamentals of Statistical Signal Processing - Estimation Theory*. Prentice Hall.

Kopsaftopoulos, F. P. and S. D. Fassois (2010). "Vibration based health monitoring for a lightweight truss structure: Experimental assessment of several statistical time series methods". In: *Mechanical Systems and Signal Processing* 24.7, pp. 1977–1997. ISSN: 08883270. DOI: 10.1016/j.ymssp.2010.05.013. URL: http://dx.doi.org/10.1016/j.ymssp.2010.05.013.

– (2013). "A functional model based statistical time series method for vibration based damage detection, localization, and magnitude estimation". In: *Mechanical Systems and Signal Processing* 39.1-2, pp. 143–161. ISSN: 08883270. DOI: 10.1016/

j.ymssp.2012.08.023. URL: http://dx.doi.org/10.1016/j.ymssp.2012.08.023.

Ledoit, Olivier and Michael Wolf (2004). "A Well-Conditioned Estimator for Large-Dimensional Covariance Matrices". In: *Journal of Multivariate Analysis* 88.2, pp. 365–411. DOI: 10.1016/s0047-259x(03)00096-4. URL: https://doi.org/10.1016/s0047-259x(03)00096-4.

Liu, Song et al. (2013). "Change-point detection in time-series data by relative density-ratio estimation". In: *Neural Networks* 43, pp. 72–83. ISSN: 0893-6080. DOI: 10.1016/j.neunet.2013.01.012. URL: https://www.sciencedirect.com/science/article/pii/S0893608013000270.

Ljung, L (1999). *System Identification: Theory for the User*. second. Englewood Cliffs, New Jersey: Prentice-Hall.

McKelvey, T (Dec. 2000). "On the Finite Length DFT of Input-Output Signals of Multivariable Linear Systems". In: *Proc.of 39th Conference on Decision and Control*. Vol. 5. Sydney, Australia, pp. 5190–5191.

McKelvey, T and G Guerin (2012). "Non-parametric frequency response estimation using a local rational model". In: *Proc. 16th IFAC Symposium on System Identification*. IFAC. Brussels, Belgium.

McKelvey, T., D. McKelvey, and P. Nordberg (2021). "A Multivariate Local Rational Modeling Approach for Detection of Structural Changes in Test Vehicles". In: *IFAC-PapersOnLine* 54.7. 19th IFAC Symposium on System Identification SYSID 2021, pp. 79–84. ISSN: 2405-8963. DOI: 10.1016/j.ifacol.2021.08.338.

McKelvey, Tomas and Guillaume Guérin (2012). "Non-Parametric frequency response estimation using a local rational model1". In: *IFAC Proceedings Volumes* 45.16. 16th IFAC Symposium on System Identification, pp. 49–54. ISSN: 1474-6670. DOI: https://doi.org/10.3182/20120711-3-BE-2027.00299. URL: http://www.sciencedirect.com/science/article/pii/S147466701537926X.

Mevel, L. et al. (2002). "Blind Subspace-Based Eigenstructure Identification Under Nonstationary Excitation Using Moving Sensors". In: *IEEE Transactions on Signal Processing* 50.1, pp. 41–48. DOI: 10.1109/78.972480. URL: https://doi.org/10.1109/78.972480.

Moskvina, Valentina and Anatoly Zhigljavsky (2003). "An Algorithm Based on Singular Spectrum Analysis for Change-Point Detection". In: *Communications in Statistics - Simulation and Computation* 32.2, pp. 319–352. DOI: 10.1081/sac-120017494. URL: https://doi.org/10.1081/sac-120017494.

Öllerer, Viktoria and Christophe Croux (2015). "Robust High-Dimensional Precision Matrix Estimation". In: *Modern Nonparametric, Robust and Multivariate Methods*. Modern Nonparametric, Robust and Multivariate Methods. Springer International Publishing, pp. 325–350. DOI: 10.1007/978-3-319-22404-6_19. URL: https://doi.org/10.1007/978-3-319-22404-6_19.

Picinbono, B. (1996). "Second-Order Complex Random Vectors and Normal Distributions". In: *IEEE Transactions on Signal Processing* 44.10, pp. 2637–2640. DOI: 10.1109/78.539051. URL: https://doi.org/10.1109/78.539051.

Pintelon, R. et al. (2011). "Improved (non-)parametric identification of dynamic systems excited by periodic signals—The multivariate case". In: *Mechanical Systems and Signal Processing* 25.8, pp. 2892–2922. ISSN: 0888-3270. DOI: 10.1016/

j.ymssp.2010.10.019. URL: http://www.sciencedirect.com/science/article/pii/S0888327011000744.

Proakis, John G. and Dimitris G. Manolakis (2007). *Digital Signal Processing: Principles, Algorithms and Appleciations*. 4th ed. Prentice Hall International.

Qin, S. Joe (2012). "Survey on data-driven industrial process monitoring and diagnosis". In: *Annual Reviews in Control* 36.2, pp. 220–234. ISSN: 1367-5788. DOI: https://doi.org/10.1016/j.arcontrol.2012.09.004. URL: https://www.sciencedirect.com/science/article/pii/S1367578812000399.

Rudin, Walter (1976). *Principles of Mathematical Analysis*. 3rd ed. McGraw-Hill Publishing.

Söderström, Torsten and Petre Stoica (1989). *System Identification*. 1st ed. Prentice Hall International.

Solomon Jr, O M (Dec. 1991). "PSD computations using Welch's method. [Power Spectral Density (PSD)]". In: *U.S. Department of Energy, Office of Scientific and Technical Information*. DOI: 10.2172/5688766. URL: https://www.osti.gov/biblio/5688766.

Steutel, Fred W. and Klaas van Harn (2003). *Infinite Divisibility of Probability Distributions on the Real Line*. CRC Press. DOI: 10.1201/9780203014127.

Sugiyama, Masashi, Taiji Suzuki, and Takafumi Kanamori (2012). "Density-Ratio Matching Under the Bregman Divergence: a Unified Framework of Density-Ratio Estimation". In: *Annals of the Institute of Statistical Mathematics* 64.5, pp. 1009–1044. DOI: 10.1007/s10463-011-0343-8. URL: https://doi.org/10.1007/s10463-011-0343-8.

Sugiyama, Masashi, Taiji Suzuki, Shinichi Nakajima, et al. (2008). "Direct Importance Estimation for Covariate Shift Adaptation". In: *Annals of the Institute of Statistical Mathematics* 60.4, pp. 699–746. DOI: 10.1007/s10463-008-0197-x. URL: https://doi.org/10.1007/s10463-008-0197-x.

Voorhoeve, Robbert, Annemiek van der Maas, and Tom Oomen (2018). "Non-parametric identification of multivariable systems: A local rational modeling approach with application to a vibration isolation benchmark". In: *Mechanical Systems and Signal Processing* 105, pp. 129–152. ISSN: 10961216. DOI: 10.1016/j.ymssp.2017.11.044.

Welch, P. (1967). "The use of fast Fourier transform for the estimation of power spectra: A method based on time averaging over short, modified periodograms". In: *IEEE Transactions on Audio and Electroacoustics* 15.2, pp. 70–73. DOI: 10.1109/TAU.1967.1161901.

Yamanishi, Kenji and Jun-ichi Takeuchi (2002). "A Unifying Framework for Detecting Outliers and Change Points from Non-Stationary Time Series Data". In: *Proceedings of the Eighth ACM SIGKDD International Conference on Knowledge Discovery and Data Mining*. KDD '02. Edmonton, Alberta, Canada: Association for Computing Machinery, pp. 676–681. ISBN: 158113567X. DOI: 10.1145/775047.775148. URL: https://doi.org/10.1145/775047.775148.

Yin, S. et al. (2014). "A Review on Basic Data-Driven Approaches for Industrial Process Monitoring". In: *IEEE Transactions on Industrial Electronics* 61.11, pp. 6418–6428. DOI: 10.1109/TIE.2014.2301773. URL: https://ieeexplore.ieee.org/document/6717991.

A

Appendix 1

A.1 MBS: ball joint gap

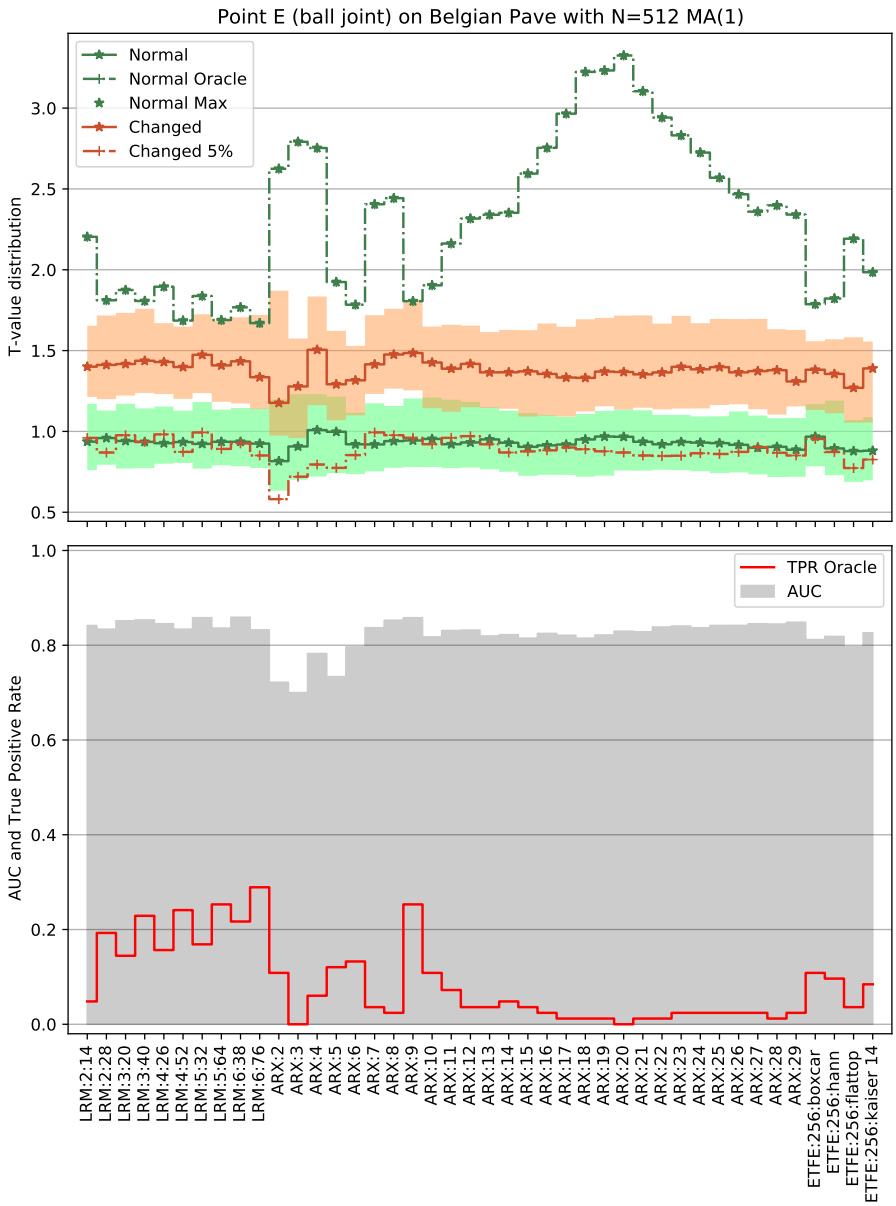

Figure A.1

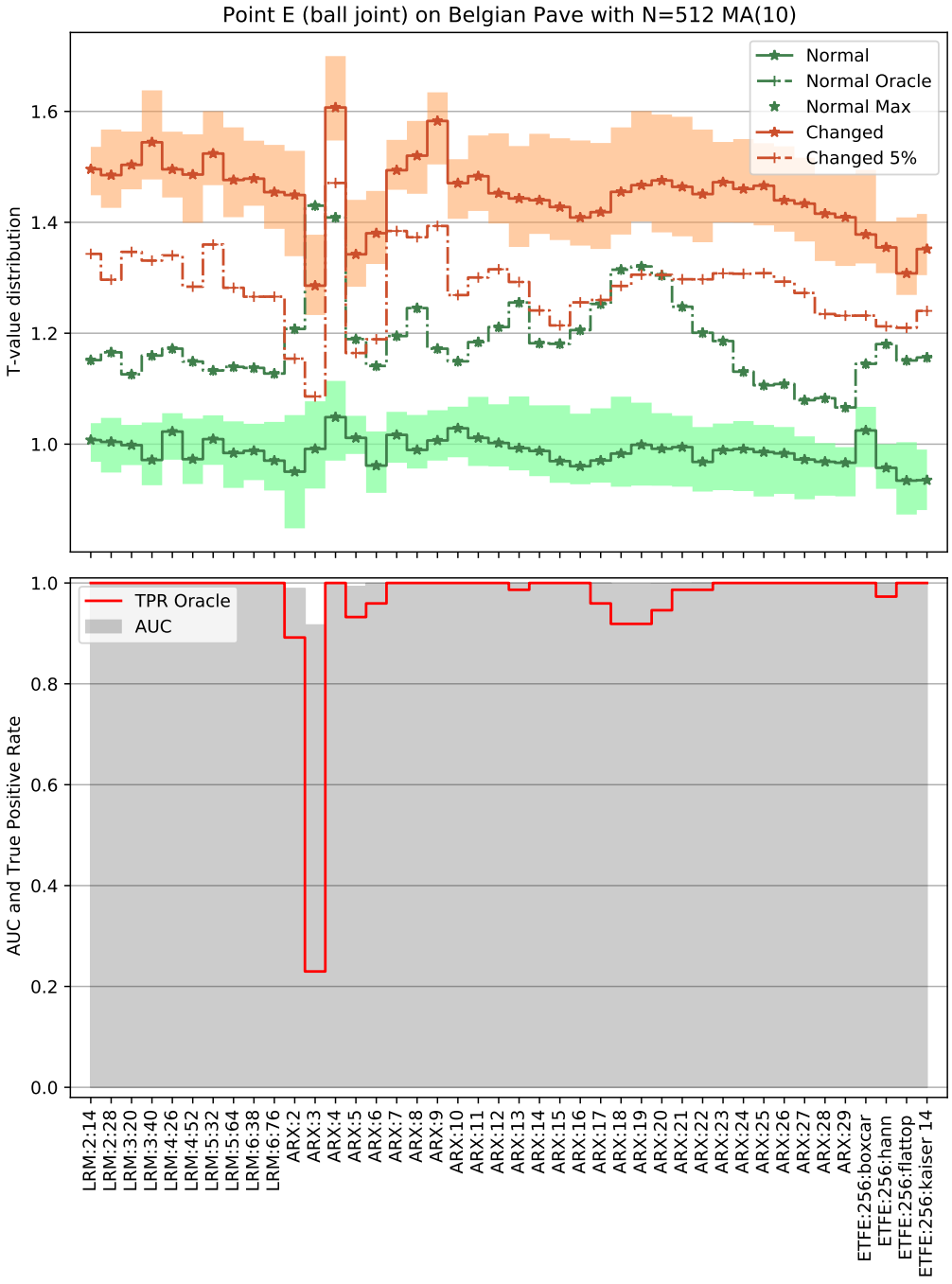
Point E (ball joint) on Belgian Pave with N=512 MA(10)
Normal
Normal Oracle
Normal Max
Changed
Changed 5%
T-value distribution
1.6
1.4
1.2
1.0
TPR Oracle
AUC
AUC and True Positive Rate
0.8
0.6
0.4
0.2
0.0
LRM:2:14
LRM:2:28
LRM:3:20
LRM:3:40
LRM:4:26
LRM:4:52
LRM:5:32
LRM:5:64
LRM:6:38
LRM:6:76
ARX:2
ARX:3
ARX:4
ARX:5
ARX:6
ARX:7
ARX:8
ARX:9
ARX:10
ARX:11
ARX:12
ARX:13
ARX:14
ARX:15
ARX:16
ARX:17
ARX:18
ARX:19
ARX:20
ARX:21
ARX:22
ARX:23
ARX:24
ARX:25
ARX:26
ARX:27
ARX:28
ARX:29
ETFE:256:boxcar
ETFE:256:hann
ETFE:256:flattop
ETFE:256:kaiser 14

Figure A.2

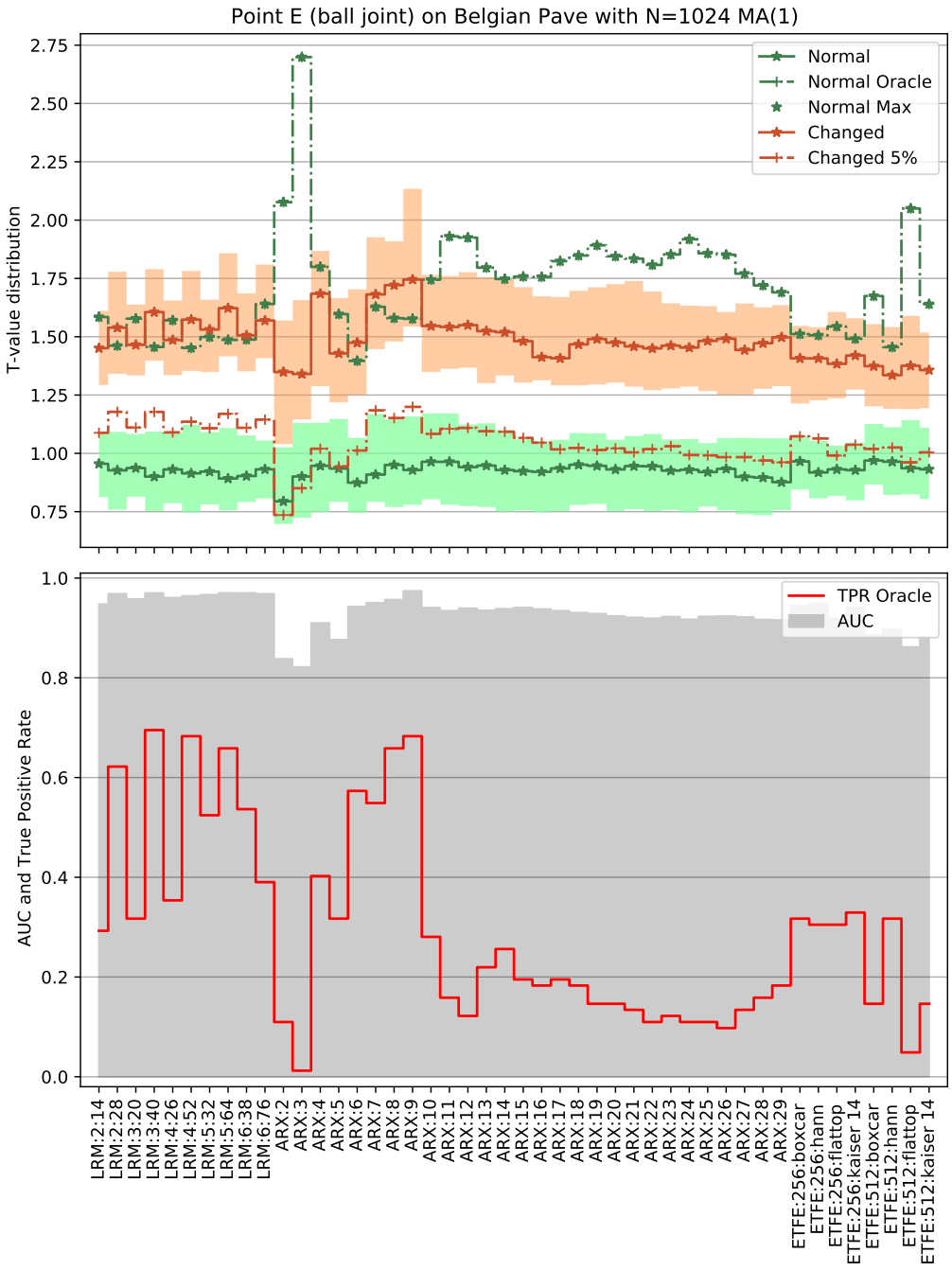
Point E (ball joint) on Belgian Pave with N=1024 MA(1)
T-value distribution
Normal
Normal Oracle
Normal Max
Changed
Changed 5%
AUC and True Positive Rate
TPR Oracle
AUC
LRM:2:14
LRM:2:28
LRM:3:20
LRM:3:40
LRM:4:26
LRM:4:52
LRM:5:32
LRM:5:64
LRM:6:38
LRM:6:76
ARX:2
ARX:3
ARX:4
ARX:5
ARX:6
ARX:7
ARX:8
ARX:9
ARX:10
ARX:11
ARX:12
ARX:13
ARX:14
ARX:15
ARX:16
ARX:17
ARX:18
ARX:19
ARX:20
ARX:21
ARX:22
ARX:23
ARX:24
ARX:25
ARX:26
ARX:27
ARX:28
ARX:29
ETFE:256:boxcar
ETFE:256:hann
ETFE:256:flattop
ETFE:256:kaiser 14
ETFE:512:boxcar
ETFE:512:hann
ETFE:512:flattop
ETFE:512:kaiser 14

Figure A.3

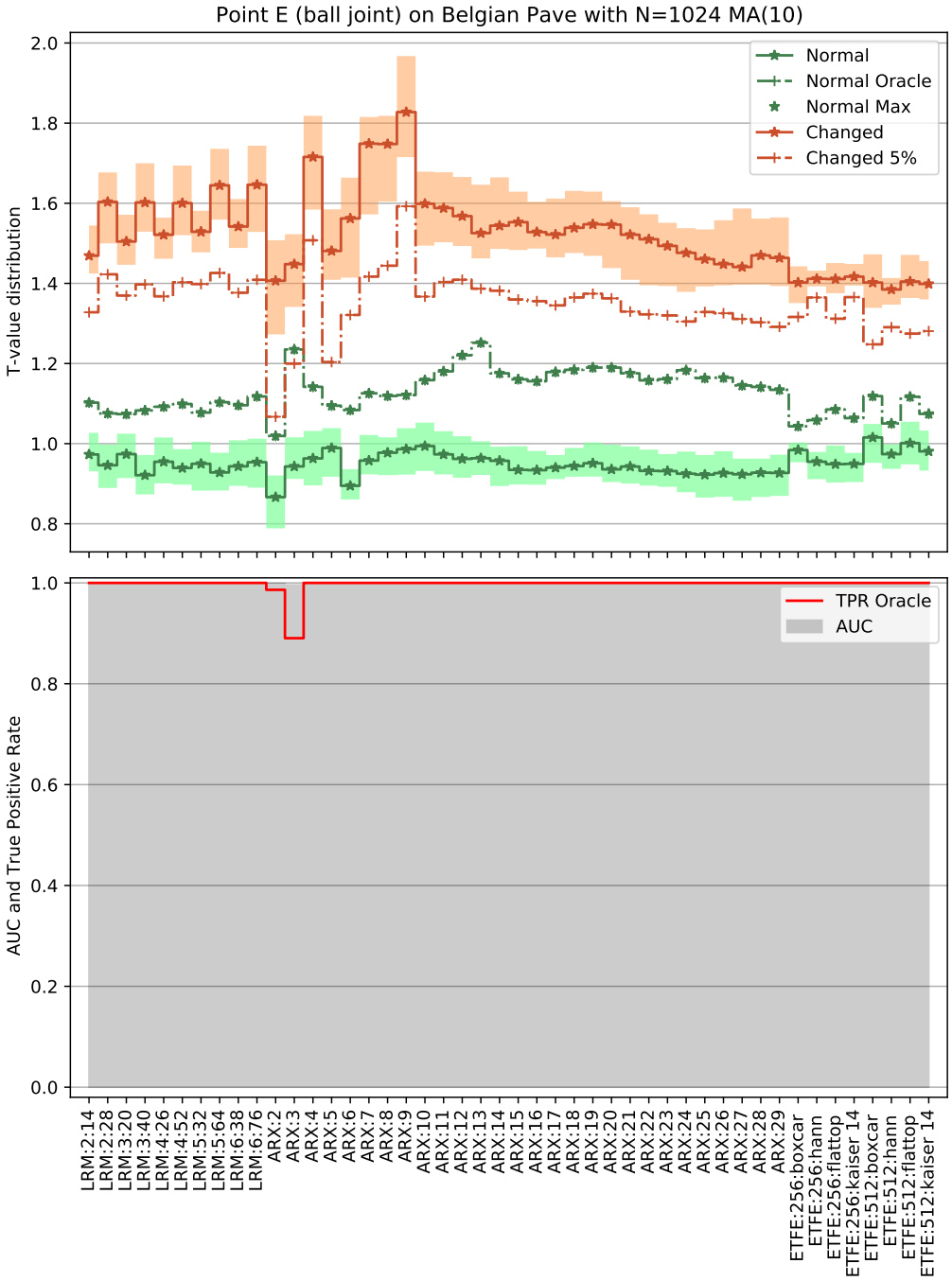
Point E (ball joint) on Belgian Pave with N=1024 MA(10)
T-value distribution
Normal
Normal Oracle
Normal Max
Changed
Changed 5%
AUC and True Positive Rate
TPR Oracle
AUC
LRM:2:14
LRM:2:28
LRM:3:20
LRM:3:40
LRM:4:26
LRM:4:52
LRM:5:32
LRM:5:64
LRM:6:38
LRM:6:76
ARX:2
ARX:3
ARX:4
ARX:5
ARX:6
ARX:7
ARX:8
ARX:9
ARX:10
ARX:11
ARX:12
ARX:13
ARX:14
ARX:15
ARX:16
ARX:17
ARX:18
ARX:19
ARX:20
ARX:21
ARX:22
ARX:23
ARX:24
ARX:25
ARX:26
ARX:27
ARX:28
ARX:29
ETFE:256:boxcar
ETFE:256:hann
ETFE:256:flattop
ETFE:256:kaiser 14
ETFE:512:boxcar
ETFE:512:hann
ETFE:512:flattop
ETFE:512:kaiser 14

Figure A.4

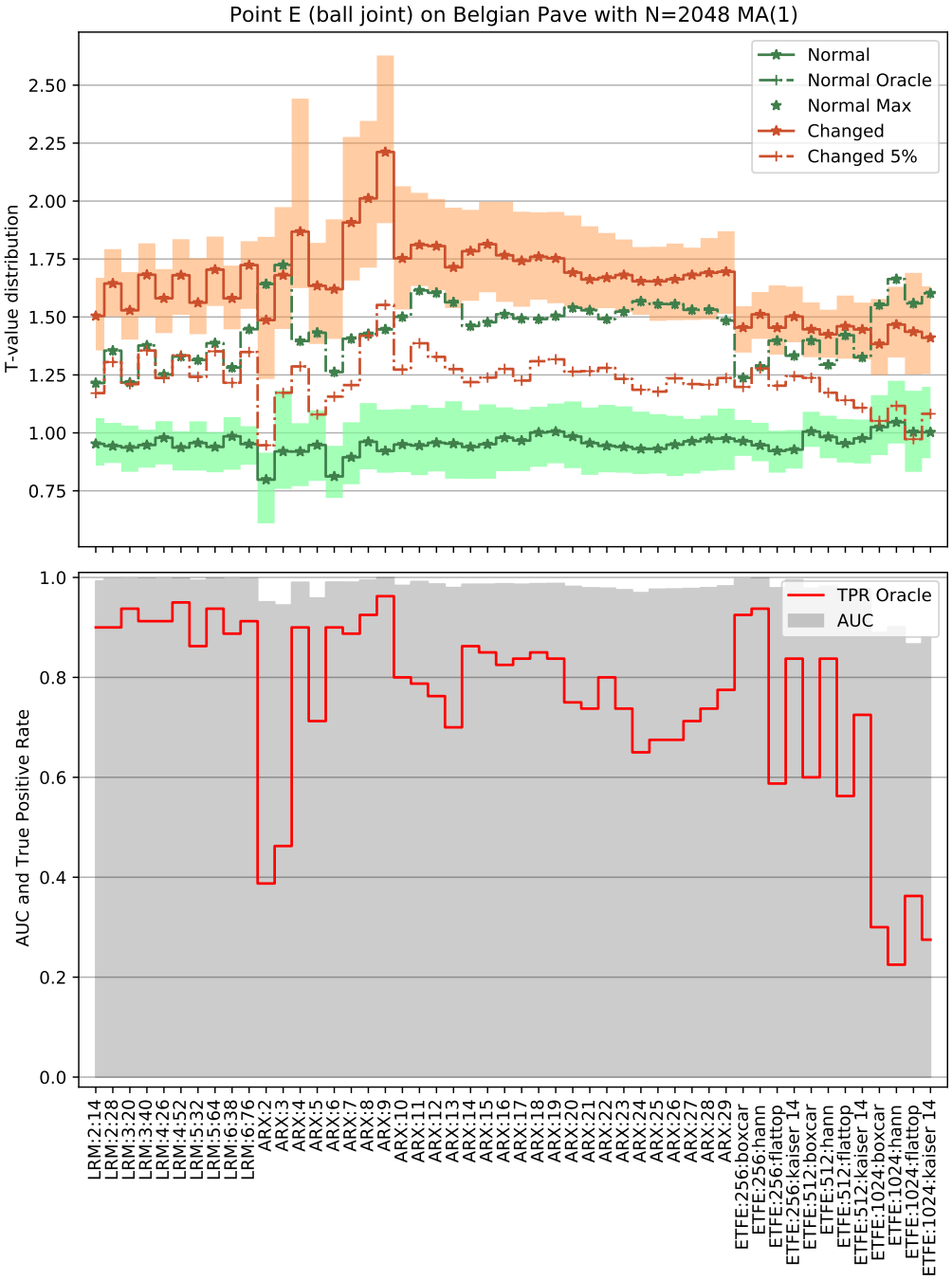
Point E (ball joint) on Belgian Pave with N=2048 MA(1)
Normal
Normal Oracle
Normal Max
Changed
Changed 5%
T-value distribution
2.50
2.25
2.00
1.75
1.50
1.25
1.00
0.75
TPR Oracle
AUC
AUC and True Positive Rate
1.0
0.8
0.6
0.4
0.2
0.0
LRM:2:14
LRM:2:28
LRM:3:20
LRM:3:40
LRM:4:26
LRM:4:52
LRM:5:32
LRM:5:64
LRM:6:38
LRM:6:76
ARX:2
ARX:3
ARX:4
ARX:5
ARX:6
ARX:7
ARX:8
ARX:9
ARX:10
ARX:11
ARX:12
ARX:13
ARX:14
ARX:15
ARX:16
ARX:17
ARX:18
ARX:19
ARX:20
ARX:21
ARX:22
ARX:23
ARX:24
ARX:25
ARX:26
ARX:27
ARX:28
ARX:29
ETFE:256:boxcar
ETFE:256:hann
ETFE:256:flattop
ETFE:256:kaiser 14
ETFE:512:boxcar
ETFE:512:hann
ETFE:512:flattop
ETFE:512:kaiser 14
ETFE:1024:boxcar
ETFE:1024:hann
ETFE:1024:flattop
ETFE:1024:kaiser 14

Figure A.5

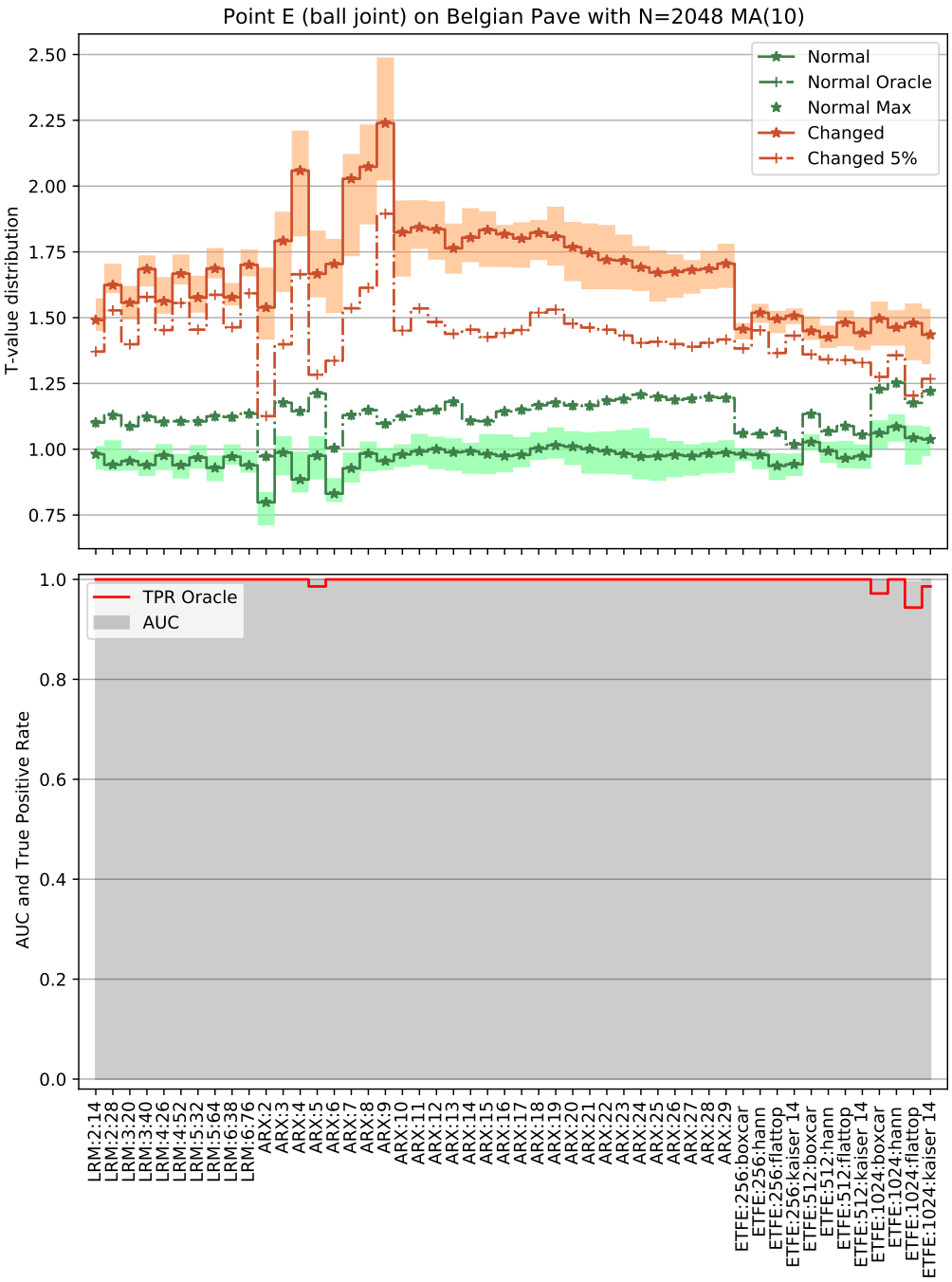
Point E (ball joint) on Belgian Pave with N=2048 MA(10)
T-value distribution
Normal
Normal Oracle
Normal Max
Changed
Changed 5%
AUC and True Positive Rate
TPR Oracle
AUC
LRM:2:14
LRM:2:28
LRM:3:20
LRM:3:40
LRM:4:26
LRM:4:52
LRM:5:32
LRM:5:64
LRM:6:38
LRM:6:76
ETFE:256:boxcar
ETFE:256:hann
ETFE:256:flattop
ETFE:256:kaiser 14
ETFE:512:boxcar
ETFE:512:hann
ETFE:512:flattop
ETFE:512:kaiser 14
ETFE:1024:boxcar
ETFE:1024:hann
ETFE:1024:flattop
ETFE:1024:kaiser 14

Figure A.6

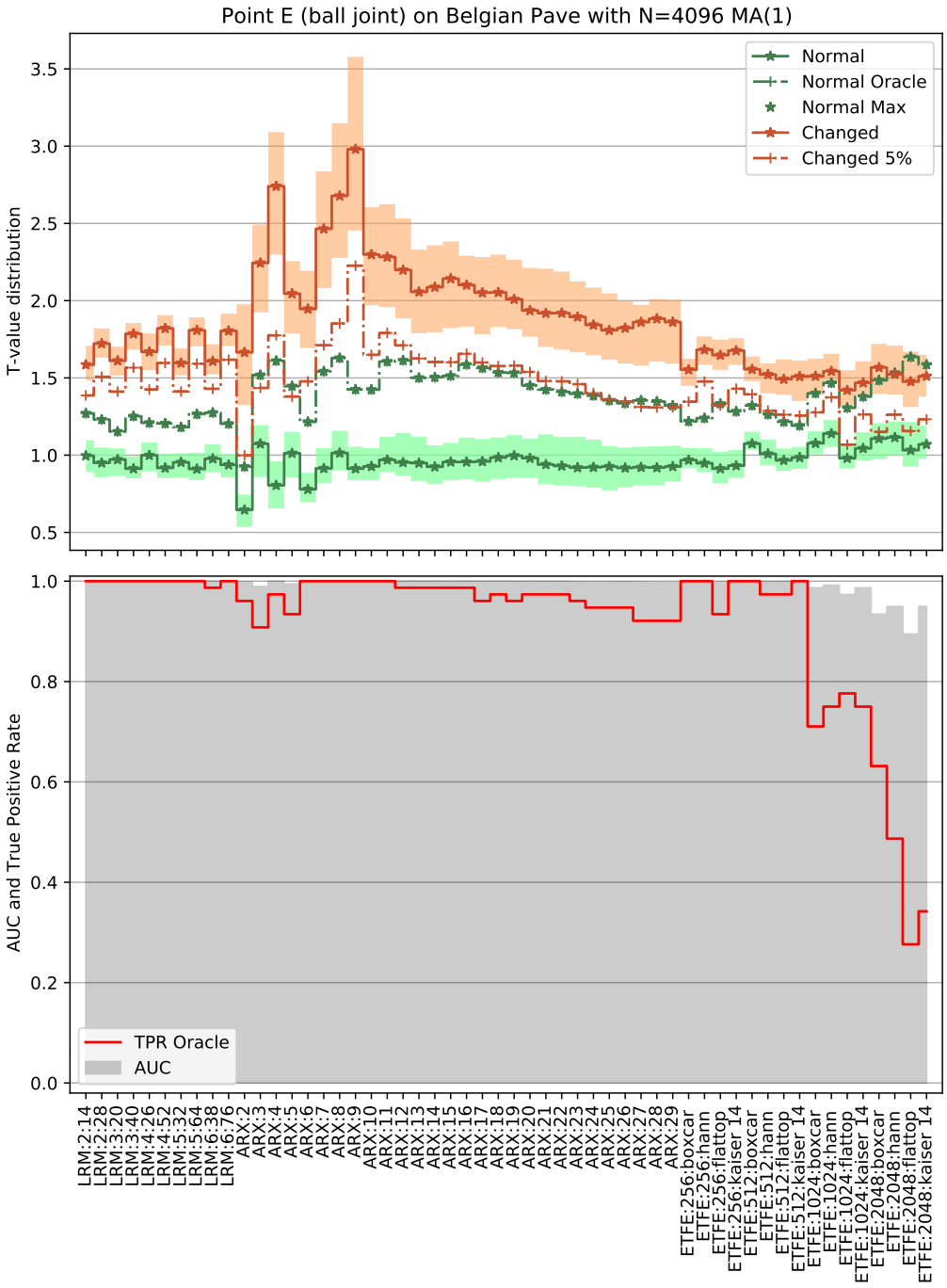
Point E (ball joint) on Belgian Pave with N=4096 MA(1)
Normal
Normal Oracle
Normal Max
Changed
Changed 5%
T-value distribution
AUC and True Positive Rate
TPR Oracle
AUC
LRM:2:14
LRM:2:28
LRM:3:20
LRM:3:40
LRM:4:26
LRM:4:52
LRM:5:32
LRM:5:64
LRM:6:38
LRM:6:76
ARX:2
ARX:3
ARX:4
ARX:5
ARX:6
ARX:7
ARX:8
ARX:9
ARX:10
ARX:11
ARX:12
ARX:13
ARX:14
ARX:15
ARX:16
ARX:17
ARX:18
ARX:19
ARX:20
ARX:21
ARX:22
ARX:23
ARX:24
ARX:25
ARX:26
ARX:27
ARX:28
ARX:29
ETFE:256:boxcar
ETFE:256:hann
ETFE:256:flattop
ETFE:256:kaiser 14
ETFE:512:boxcar
ETFE:512:hann
ETFE:512:flattop
ETFE:512:kaiser 14
ETFE:1024:boxcar
ETFE:1024:hann
ETFE:1024:flattop
ETFE:1024:kaiser 14
ETFE:2048:boxcar
ETFE:2048:hann
ETFE:2048:flattop
ETFE:2048:kaiser 14

Figure A.7

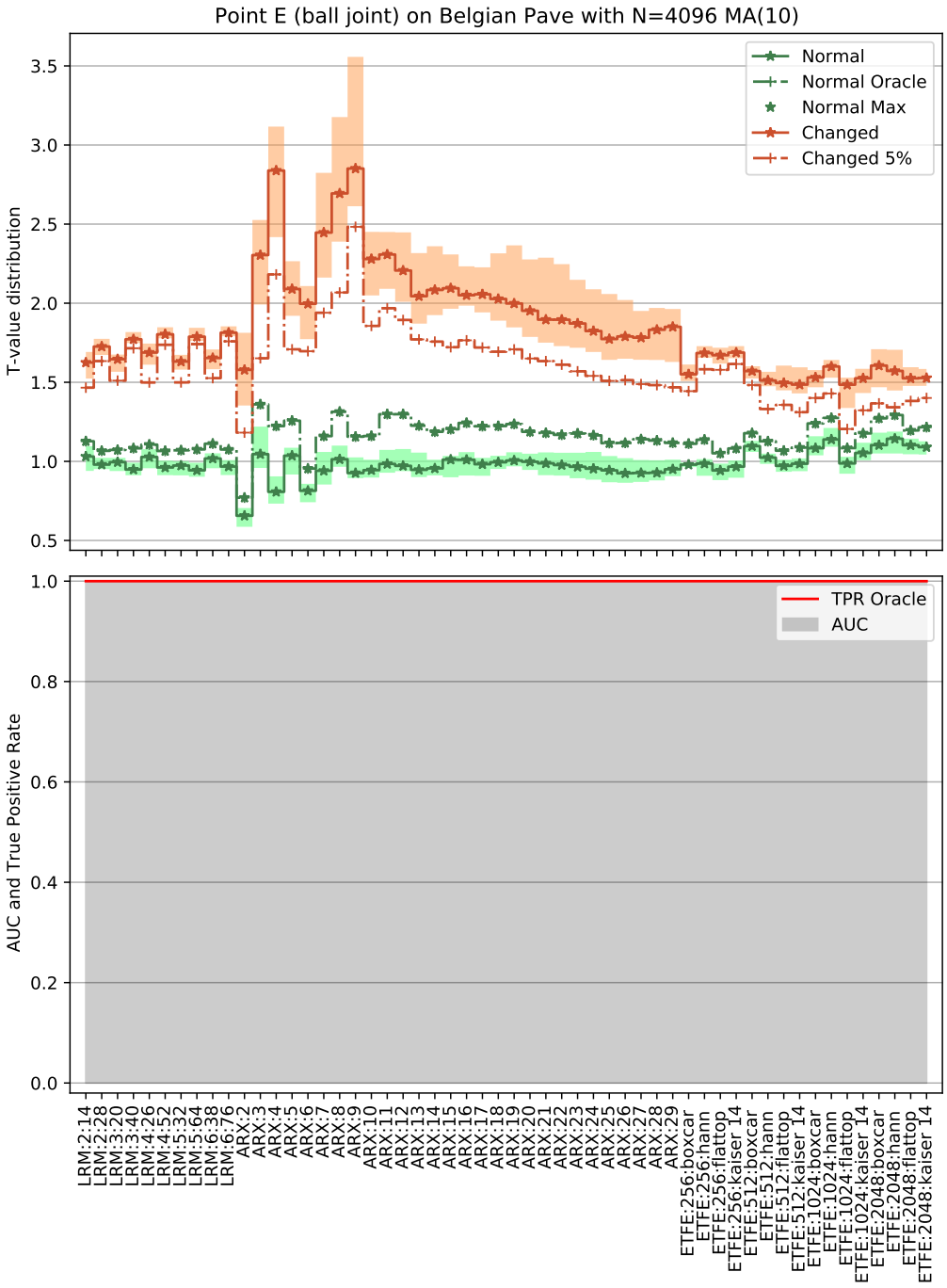
Point E (ball joint) on Belgian Pave with N=4096 MA(10)
Normal
Normal Oracle
Normal Max
Changed
Changed 5%
T-value distribution
3.5
3.0
2.5
2.0
1.5
1.0
0.5
TPR Oracle
AUC
AUC and True Positive Rate
1.0
0.8
0.6
0.4
0.2
0.0
LRM:2:14
LRM:2:28
LRM:3:20
LRM:3:40
LRM:4:26
LRM:4:52
LRM:5:32
LRM:5:64
LRM:6:38
LRM:6:76
ARX:2
ARX:3
ARX:4
ARX:5
ARX:6
ARX:7
ARX:8
ARX:9
ARX:10
ARX:11
ARX:12
ARX:13
ARX:14
ARX:15
ARX:16
ARX:17
ARX:18
ARX:19
ARX:20
ARX:21
ARX:22
ARX:23
ARX:24
ARX:25
ARX:26
ARX:27
ARX:28
ARX:29
ETFE:256:boxcar
ETFE:256:hann
ETFE:256:flattop
ETFE:256:kaiser 14
ETFE:512:boxcar
ETFE:512:hann
ETFE:512:flattop
ETFE:512:kaiser 14
ETFE:1024:boxcar
ETFE:1024:hann
ETFE:1024:flattop
ETFE:1024:kaiser 14
ETFE:2048:boxcar
ETFE:2048:hann
ETFE:2048:flattop
ETFE:2048:kaiser 14

Figure A.8

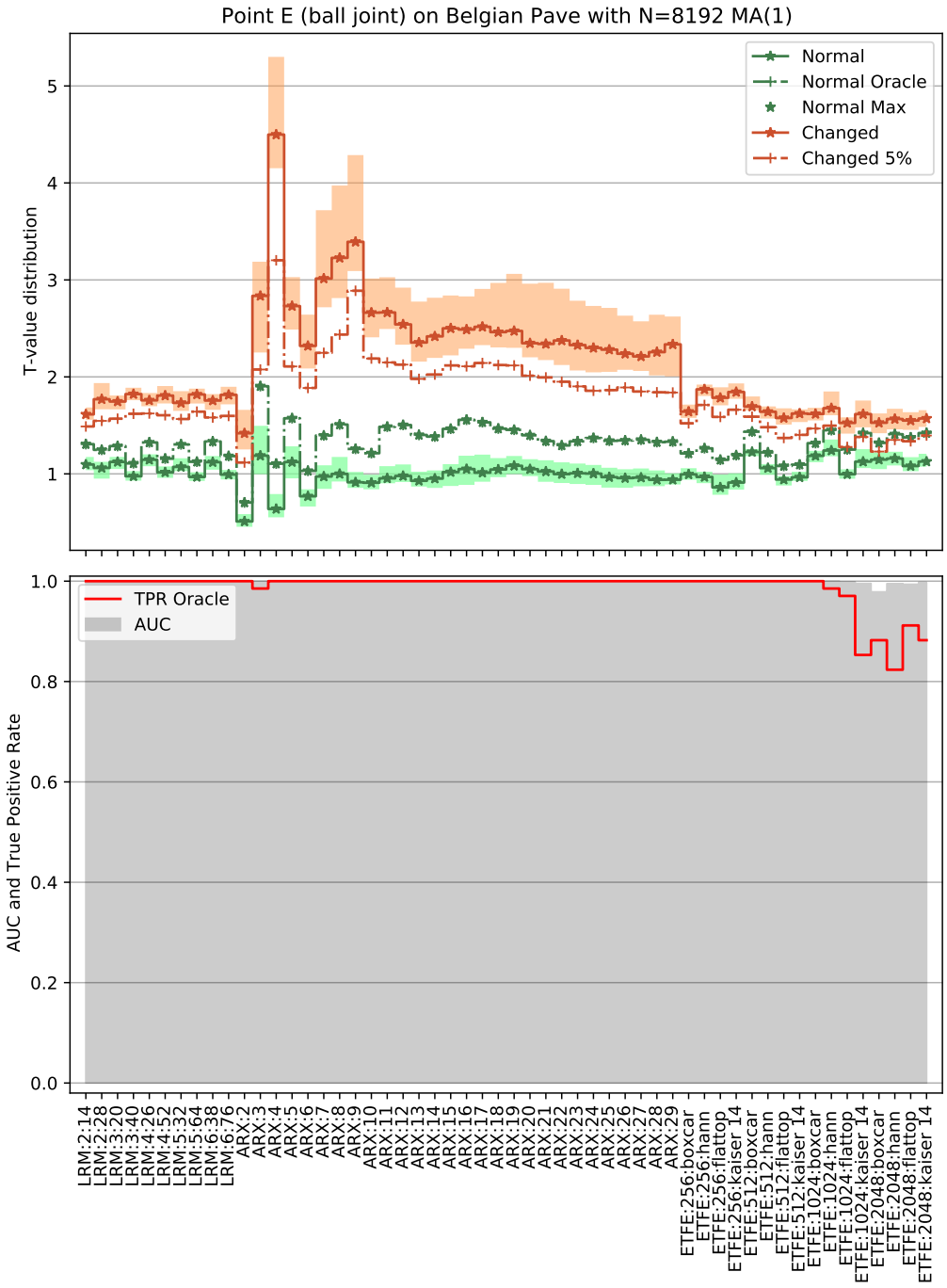
Point E (ball joint) on Belgian Pave with N=8192 MA(1)
Normal
Normal Oracle
Normal Max
Changed
Changed 5%
T-value distribution
TPR Oracle
AUC
AUC and True Positive Rate
LRM:2:14
LRM:2:28
LRM:3:20
LRM:3:40
LRM:4:26
LRM:4:52
LRM:5:32
LRM:5:64
LRM:6:38
LRM:6:76
ARX:2
ARX:3
ARX:4
ARX:5
ARX:6
ARX:7
ARX:8
ARX:9
ARX:10
ARX:11
ARX:12
ARX:13
ARX:14
ARX:15
ARX:16
ARX:17
ARX:18
ARX:19
ARX:20
ARX:21
ARX:22
ARX:23
ARX:24
ARX:25
ARX:26
ARX:27
ARX:28
ARX:29
ETFE:256:boxcar
ETFE:256:hann
ETFE:256:flattop
ETFE:256:kaiser 14
ETFE:512:boxcar
ETFE:512:hann
ETFE:512:flattop
ETFE:512:kaiser 14
ETFE:1024:boxcar
ETFE:1024:hann
ETFE:1024:flattop
ETFE:1024:kaiser 14
ETFE:2048:boxcar
ETFE:2048:hann
ETFE:2048:flattop
ETFE:2048:kaiser 14

Figure A.9

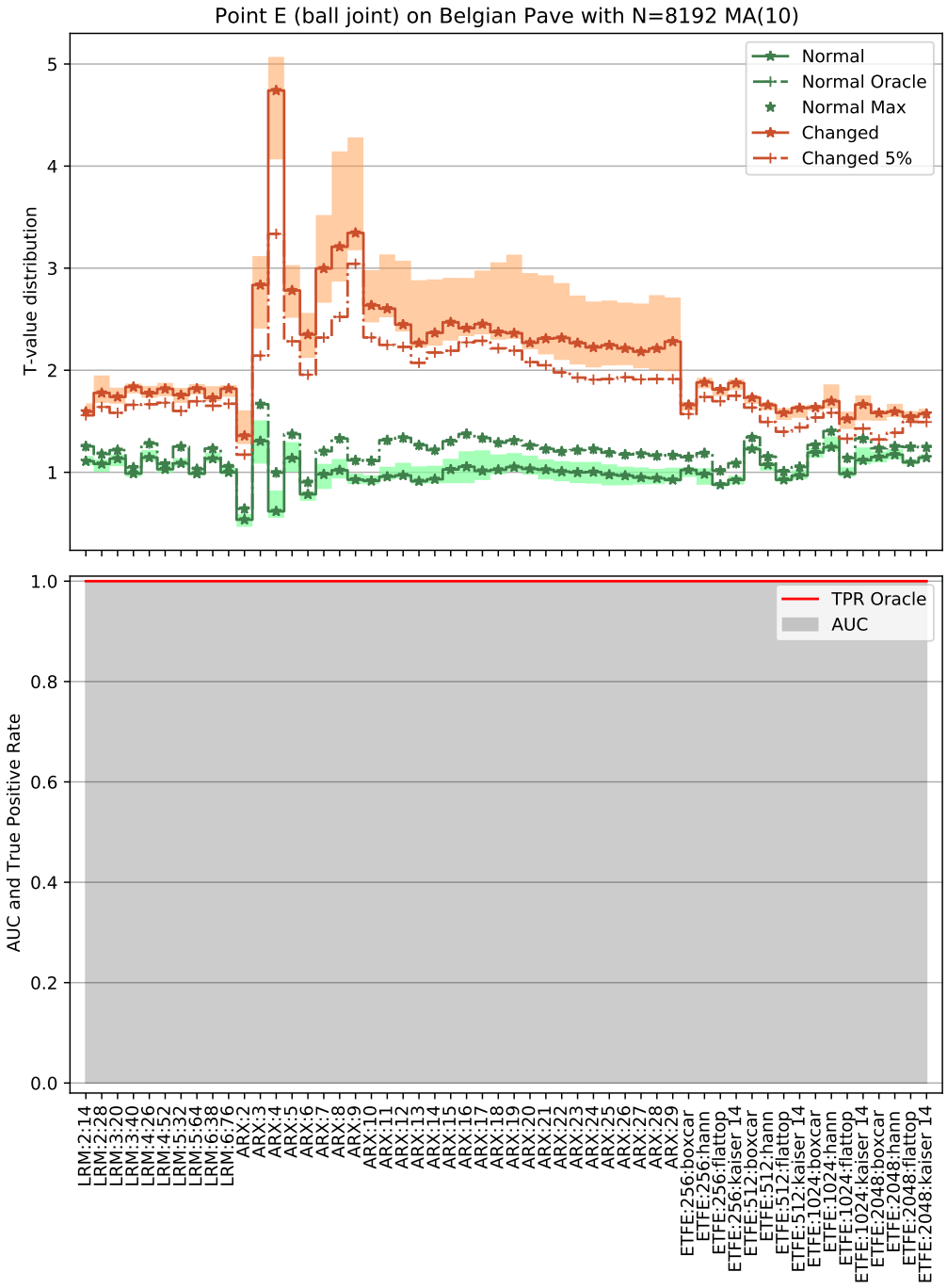
Point E (ball joint) on Belgian Pave with N=8192 MA(10)
T-value distribution
Normal
Normal Oracle
Normal Max
Changed
Changed 5%
AUC and True Positive Rate
TPR Oracle
AUC
LRM:2:14
LRM:2:28
LRM:3:20
LRM:3:40
LRM:4:26
LRM:4:52
LRM:5:32
LRM:5:64
LRM:6:38
LRM:6:76
ARX:2
ARX:3
ARX:4
ARX:5
ARX:6
ARX:7
ARX:8
ARX:9
ARX:10
ARX:11
ARX:12
ARX:13
ARX:14
ARX:15
ARX:16
ARX:17
ARX:18
ARX:19
ARX:20
ARX:21
ARX:22
ARX:23
ARX:24
ARX:25
ARX:26
ARX:27
ARX:28
ARX:29
ETFE:256:boxcar
ETFE:256:hann
ETFE:256:flattop
ETFE:256:kaiser 14
ETFE:512:boxcar
ETFE:512:hann
ETFE:512:flattop
ETFE:512:kaiser 14
ETFE:1024:boxcar
ETFE:1024:hann
ETFE:1024:flattop
ETFE:1024:kaiser 14
ETFE:2048:boxcar
ETFE:2048:hann
ETFE:2048:flattop
ETFE:2048:kaiser 14

Figure A.10

A.2 MBS: bushing 75% residual stiffness

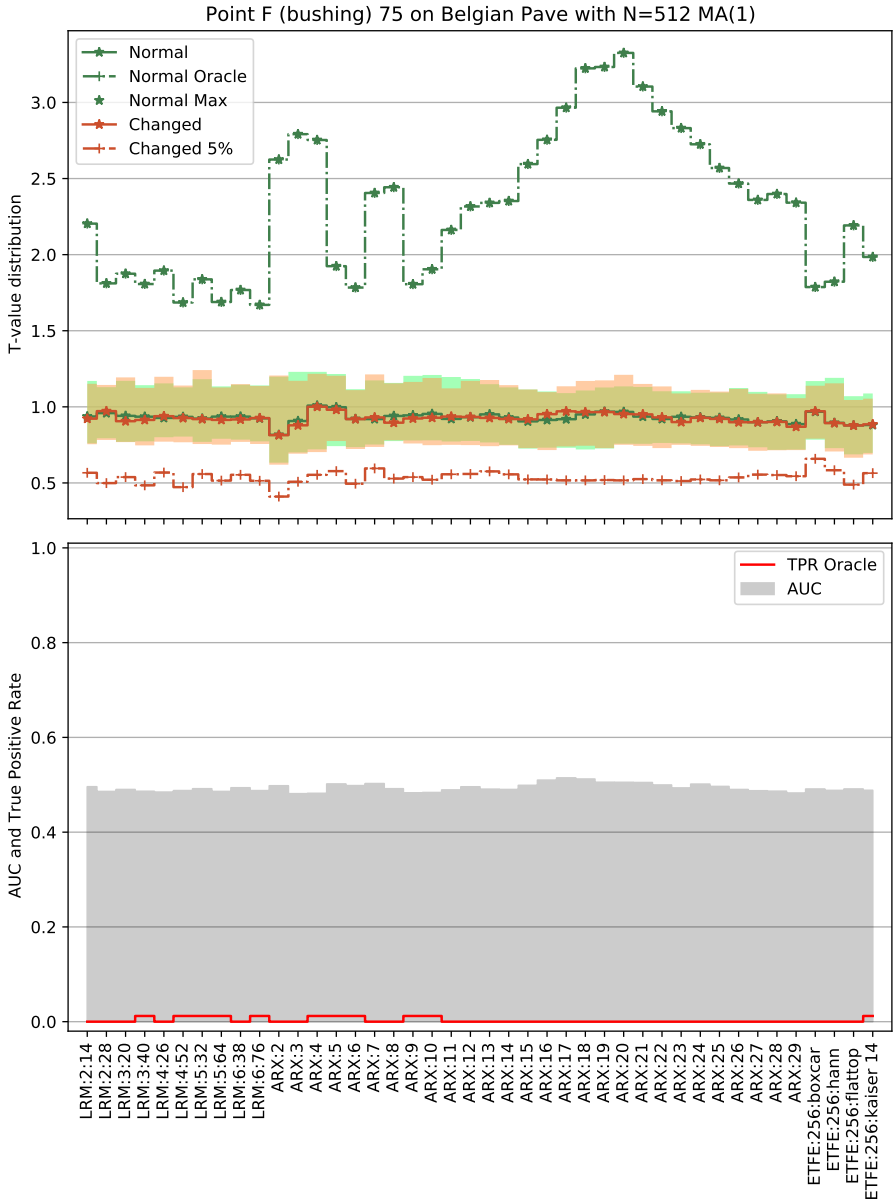

Figure A.11

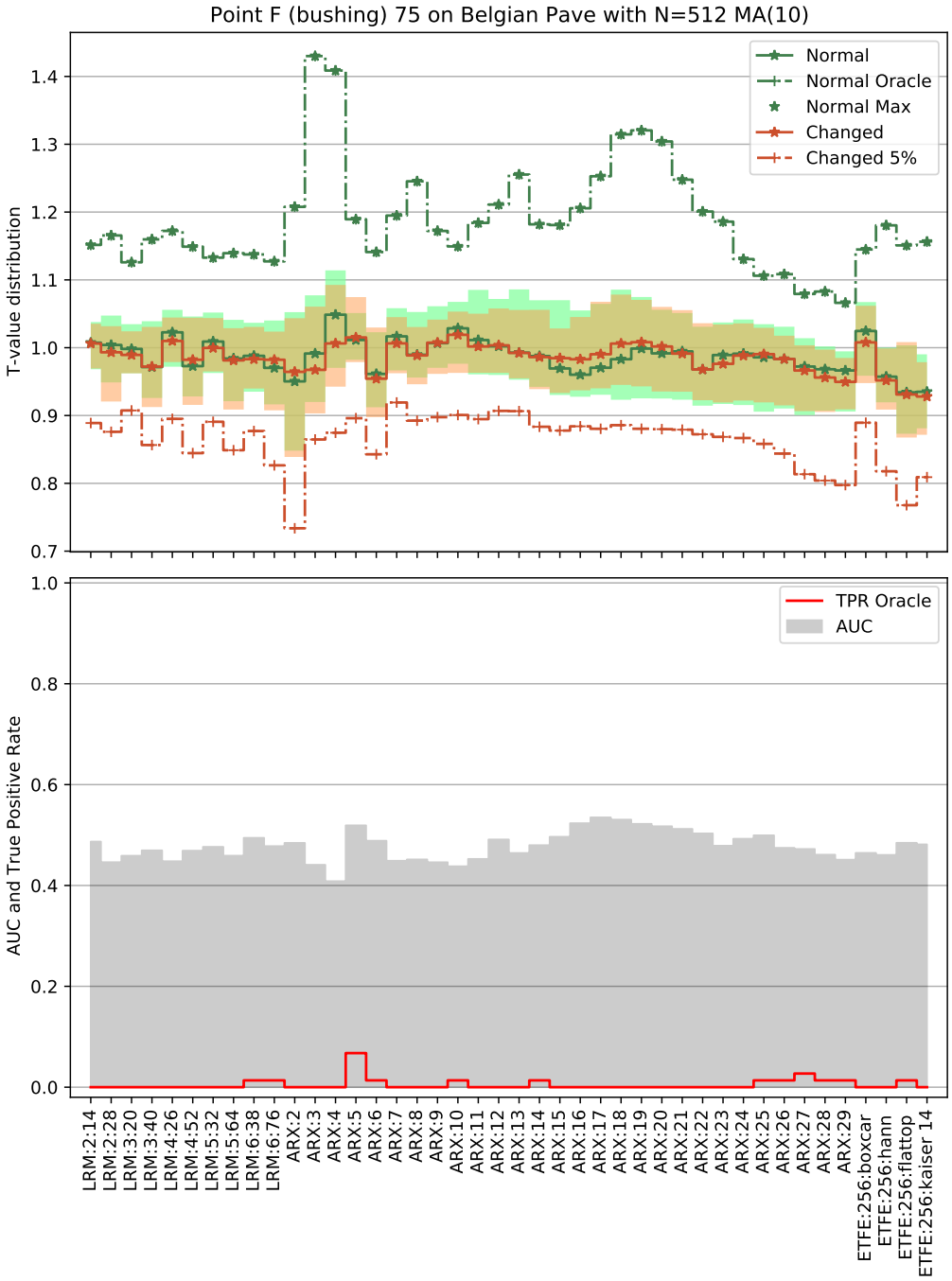
Point F (bushing) 75 on Belgian Pave with N=512 MA(10)
Normal
Normal Oracle
Normal Max
Changed
Changed 5%
T-value distribution
TPR Oracle
AUC
AUC and True Positive Rate
LRM:2:14
LRM:2:28
LRM:3:20
LRM:3:40
LRM:4:26
LRM:4:52
LRM:5:32
LRM:5:64
LRM:6:38
LRM:6:76
ARX:2
ARX:3
ARX:4
ARX:5
ARX:6
ARX:7
ARX:8
ARX:9
ARX:10
ARX:11
ARX:12
ARX:13
ARX:14
ARX:15
ARX:16
ARX:17
ARX:18
ARX:19
ARX:20
ARX:21
ARX:22
ARX:23
ARX:24
ARX:25
ARX:26
ARX:27
ARX:28
ARX:29
ETFE:256:boxcar
ETFE:256:hann
ETFE:256:flattop
ETFE:256:kaiser 14

Figure A.12

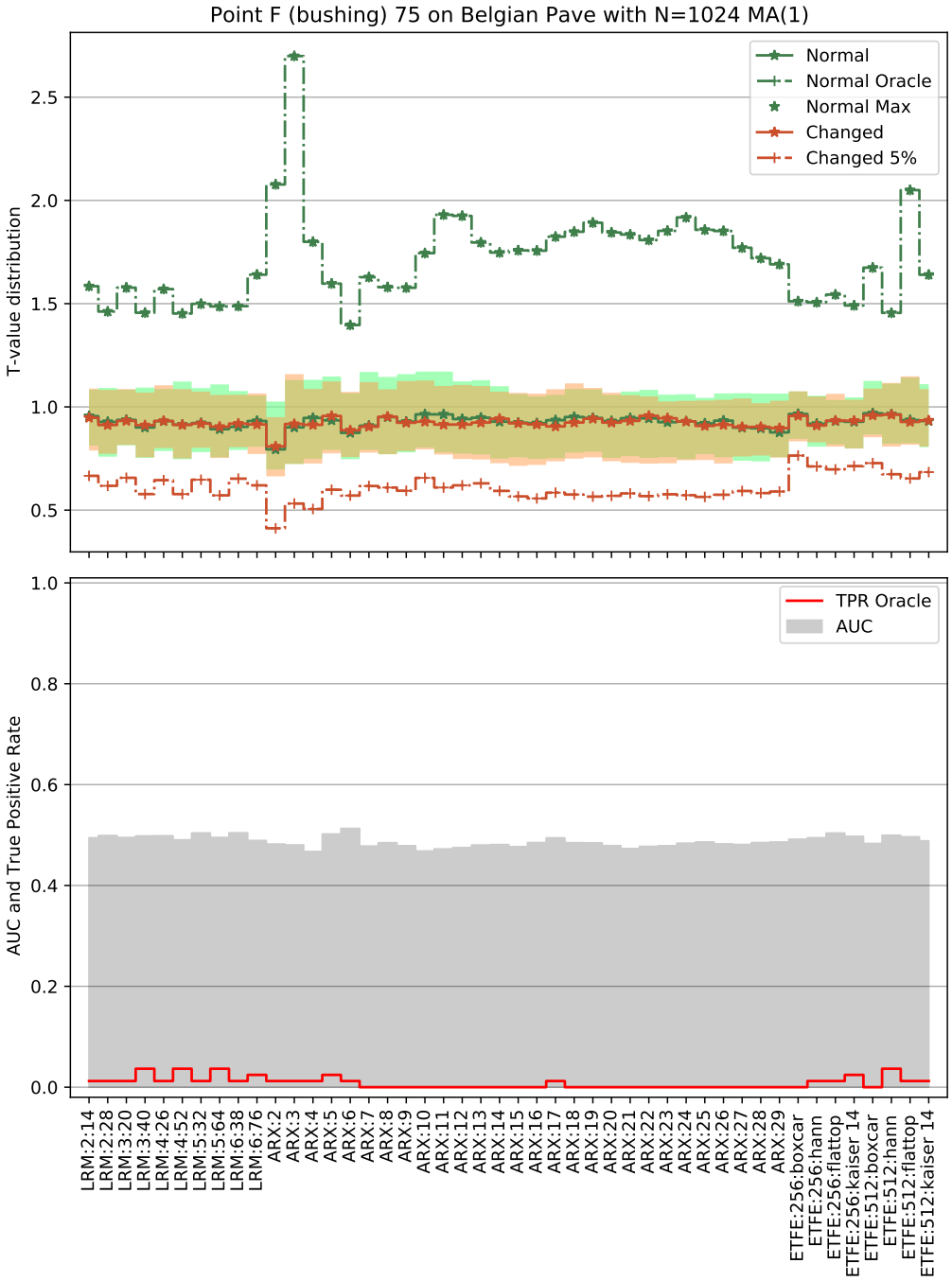
Point F (bushing) 75 on Belgian Pave with N=1024 MA(1)
Normal
Normal Oracle
Normal Max
Changed
Changed 5%
T-value distribution
2.5
2.0
1.5
1.0
0.5
TPR Oracle
AUC
AUC and True Positive Rate
1.0
0.8
0.6
0.4
0.2
0.0
LRM:2:14
LRM:2:28
LRM:3:20
LRM:3:40
LRM:4:26
LRM:4:52
LRM:5:32
LRM:5:64
LRM:6:38
LRM:6:76
ARX:2
ARX:3
ARX:4
ARX:5
ARX:6
ARX:7
ARX:8
ARX:9
ARX:10
ARX:11
ARX:12
ARX:13
ARX:14
ARX:15
ARX:16
ARX:17
ARX:18
ARX:19
ARX:20
ARX:21
ARX:22
ARX:23
ARX:24
ARX:25
ARX:26
ARX:27
ARX:28
ARX:29
ETFE:256:boxcar
ETFE:256:hann
ETFE:256:flattop
ETFE:256:kaiser 14
ETFE:512:boxcar
ETFE:512:hann
ETFE:512:flattop
ETFE:512:kaiser 14

Figure A.13

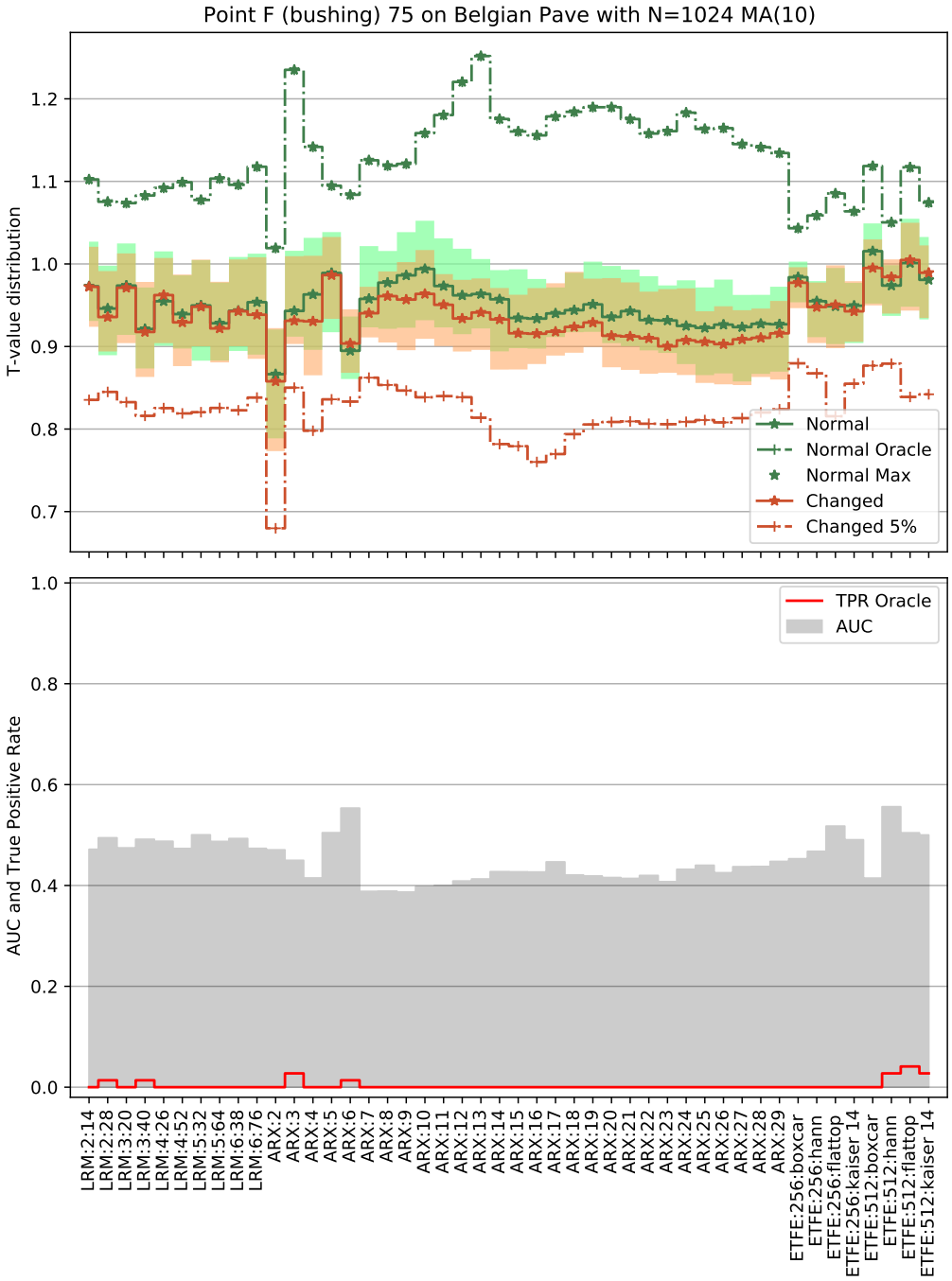
Point F (bushing) 75 on Belgian Pave with N=1024 MA(10)
T-value distribution
Normal
Normal Oracle
Normal Max
Changed
Changed 5%
AUC and True Positive Rate
TPR Oracle
AUC
LRM:2:14
LRM:2:28
LRM:3:20
LRM:3:40
LRM:4:26
LRM:4:52
LRM:5:32
LRM:5:64
LRM:6:38
LRM:6:76
ARX:2
ARX:3
ARX:4
ARX:5
ARX:6
ARX:7
ARX:8
ARX:9
ARX:10
ARX:11
ARX:12
ARX:13
ARX:14
ARX:15
ARX:16
ARX:17
ARX:18
ARX:19
ARX:20
ARX:21
ARX:22
ARX:23
ARX:24
ARX:25
ARX:26
ARX:27
ARX:28
ARX:29
ETFE:256:boxcar
ETFE:256:hann
ETFE:256:flattop
ETFE:256:kaiser 14
ETFE:512:boxcar
ETFE:512:hann
ETFE:512:flattop
ETFE:512:kaiser 14

Figure A.14

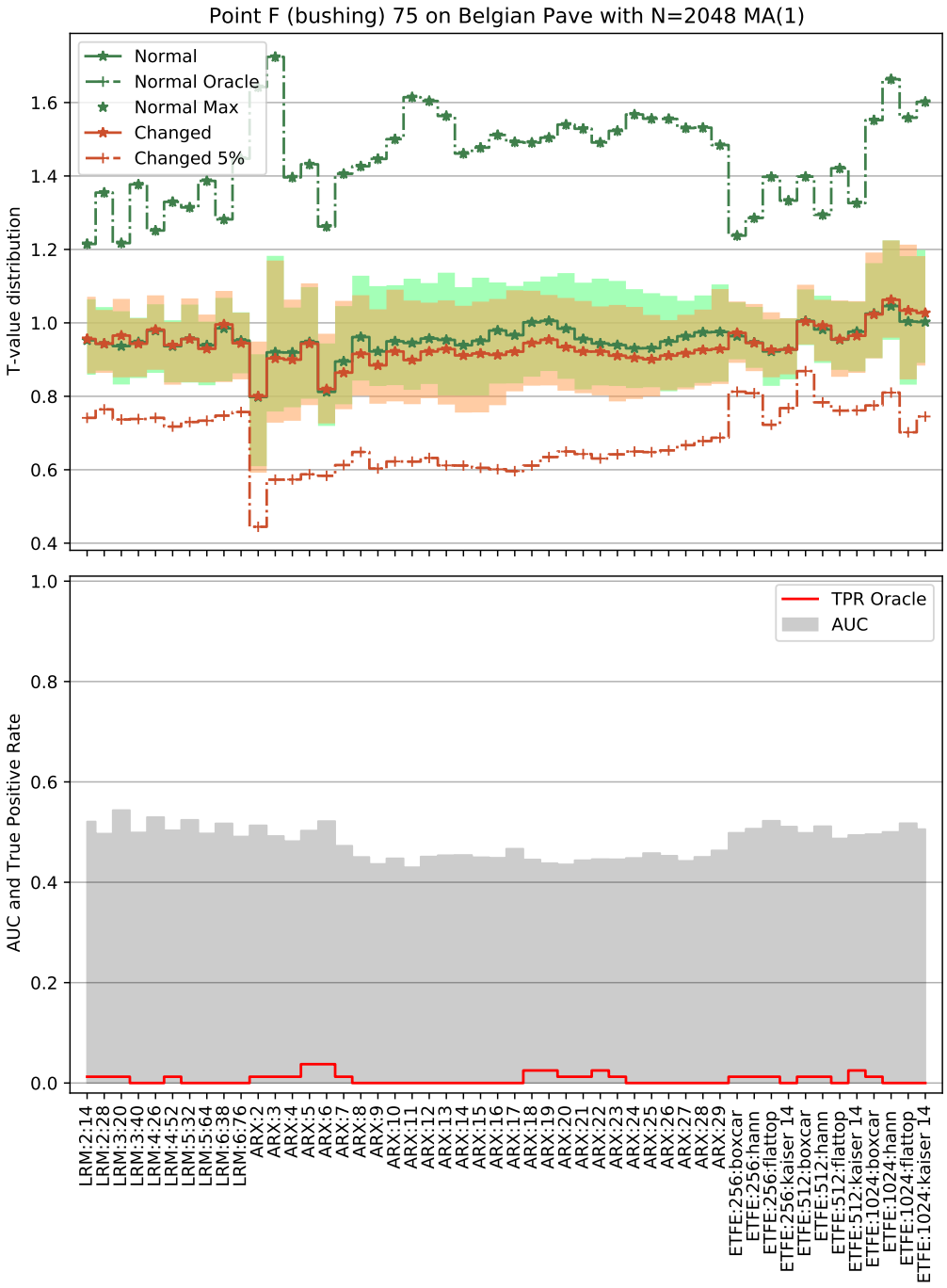
Point F (bushing) 75 on Belgian Pave with N=2048 MA(1)
Normal
Normal Oracle
Normal Max
Changed
Changed 5%
T-value distribution
TPR Oracle
AUC
AUC and True Positive Rate
LRM:2:14
LRM:2:28
LRM:3:20
LRM:3:40
LRM:4:26
LRM:4:52
LRM:5:32
LRM:5:64
LRM:6:38
LRM:6:76
ARX:2
ARX:3
ARX:4
ARX:5
ARX:6
ARX:7
ARX:8
ARX:9
ARX:10
ARX:11
ARX:12
ARX:13
ARX:14
ARX:15
ARX:16
ARX:17
ARX:18
ARX:19
ARX:20
ARX:21
ARX:22
ARX:23
ARX:24
ARX:25
ARX:26
ARX:27
ARX:28
ARX:29
ETFE:256:boxcar
ETFE:256:hann
ETFE:256:flattop
ETFE:256:kaiser 14
ETFE:512:boxcar
ETFE:512:hann
ETFE:512:flattop
ETFE:512:kaiser 14
ETFE:1024:boxcar
ETFE:1024:hann
ETFE:1024:flattop
ETFE:1024:kaiser 14

Figure A.15

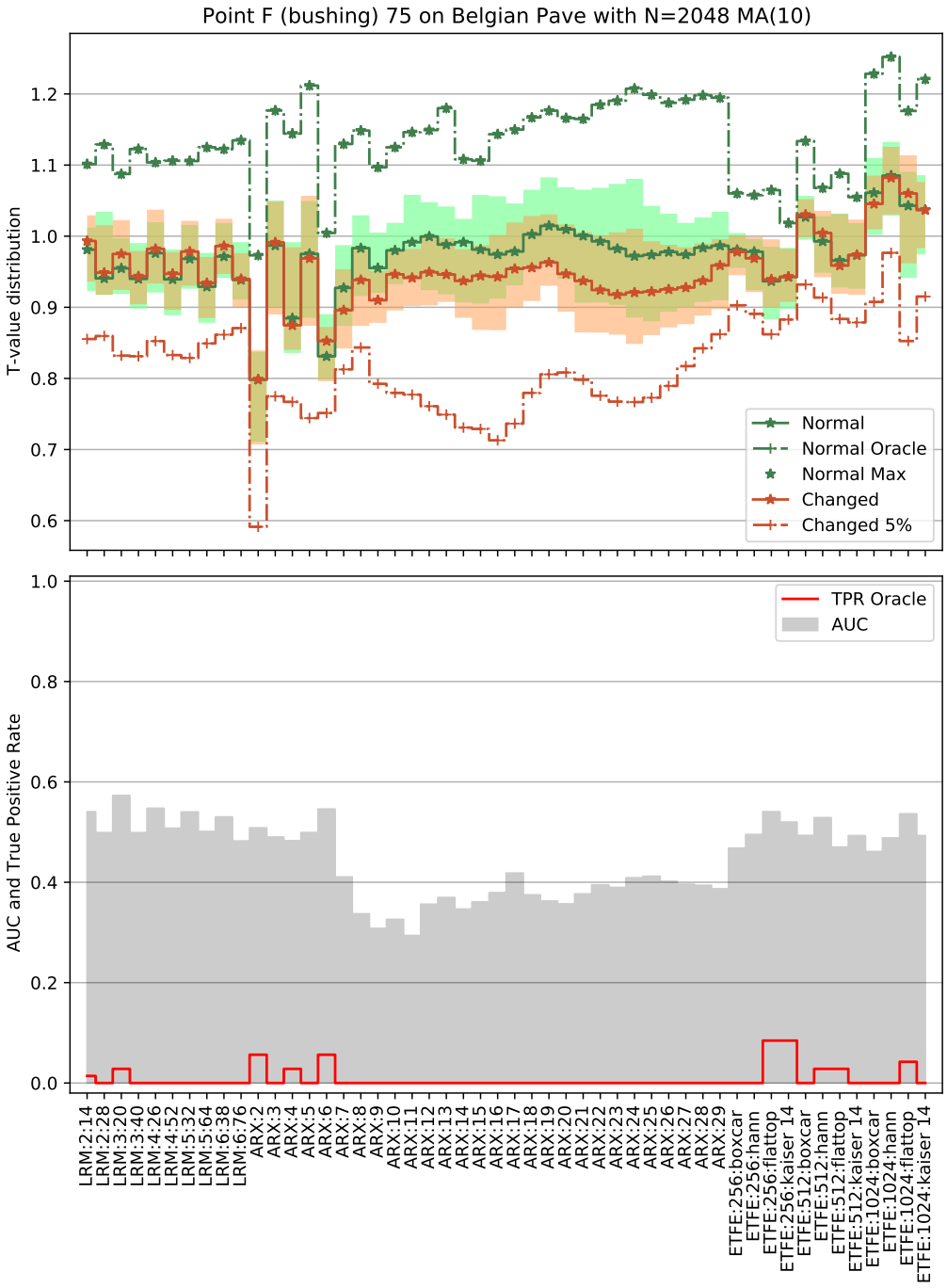
Point F (bushing) 75 on Belgian Pave with N=2048 MA(10)
T-value distribution
Normal
Normal Oracle
Normal Max
Changed
Changed 5%
AUC and True Positive Rate
TPR Oracle
AUC
LRM:2:14
LRM:2:28
LRM:3:20
LRM:3:40
LRM:4:26
LRM:4:52
LRM:5:32
LRM:5:64
LRM:6:38
LRM:6:76
ARX:2
ARX:3
ARX:4
ARX:5
ARX:6
ARX:7
ARX:8
ARX:9
ARX:10
ARX:11
ARX:12
ARX:13
ARX:14
ARX:15
ARX:16
ARX:17
ARX:18
ARX:19
ARX:20
ARX:21
ARX:22
ARX:23
ARX:24
ARX:25
ARX:26
ARX:27
ARX:28
ARX:29
ETFE:256:boxcar
ETFE:256:hann
ETFE:256:flattop
ETFE:256:kaiser 14
ETFE:512:boxcar
ETFE:512:hann
ETFE:512:flattop
ETFE:512:kaiser 14
ETFE:1024:boxcar
ETFE:1024:hann
ETFE:1024:flattop
ETFE:1024:kaiser 14

Figure A.16

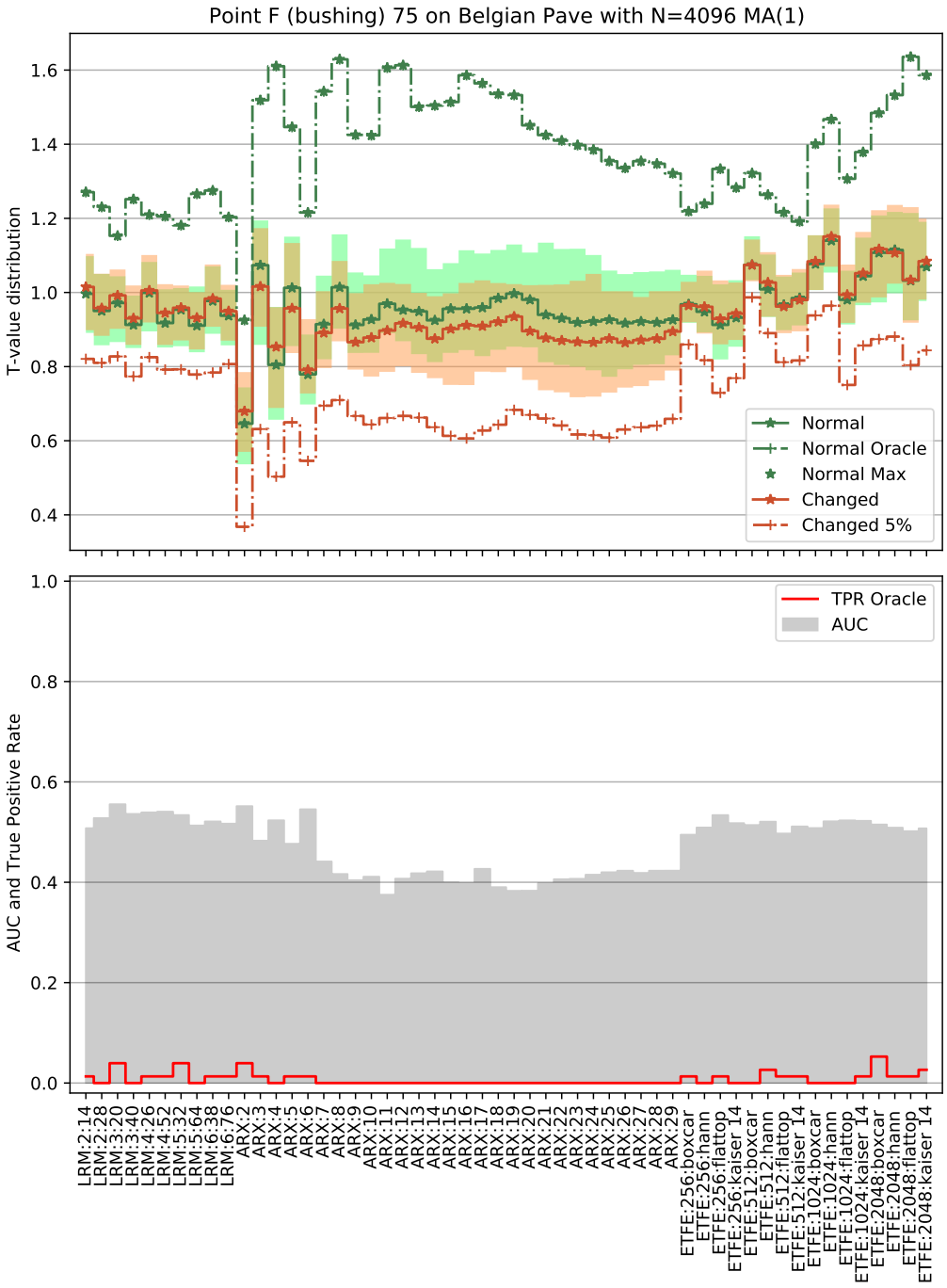
Point F (bushing) 75 on Belgian Pave with N=4096 MA(1)
T-value distribution
Normal
Normal Oracle
Normal Max
Changed
Changed 5%
AUC and True Positive Rate
TPR Oracle
AUC
LRM:2:14
LRM:2:28
LRM:3:20
LRM:3:40
LRM:4:26
LRM:4:52
LRM:5:32
LRM:5:64
LRM:6:38
LRM:6:76
ARX:2
ARX:3
ARX:4
ARX:5
ARX:6
ARX:7
ARX:8
ARX:9
ARX:10
ARX:11
ARX:12
ARX:13
ARX:14
ARX:15
ARX:16
ARX:17
ARX:18
ARX:19
ARX:20
ARX:21
ARX:22
ARX:23
ARX:24
ARX:25
ARX:26
ARX:27
ARX:28
ARX:29
ETFE:256:boxcar
ETFE:256:hann
ETFE:256:flattop
ETFE:256:kaiser 14
ETFE:512:boxcar
ETFE:512:hann
ETFE:512:flattop
ETFE:512:kaiser 14
ETFE:1024:boxcar
ETFE:1024:hann
ETFE:1024:flattop
ETFE:1024:kaiser 14
ETFE:2048:boxcar
ETFE:2048:hann
ETFE:2048:flattop
ETFE:2048:kaiser 14

Figure A.17

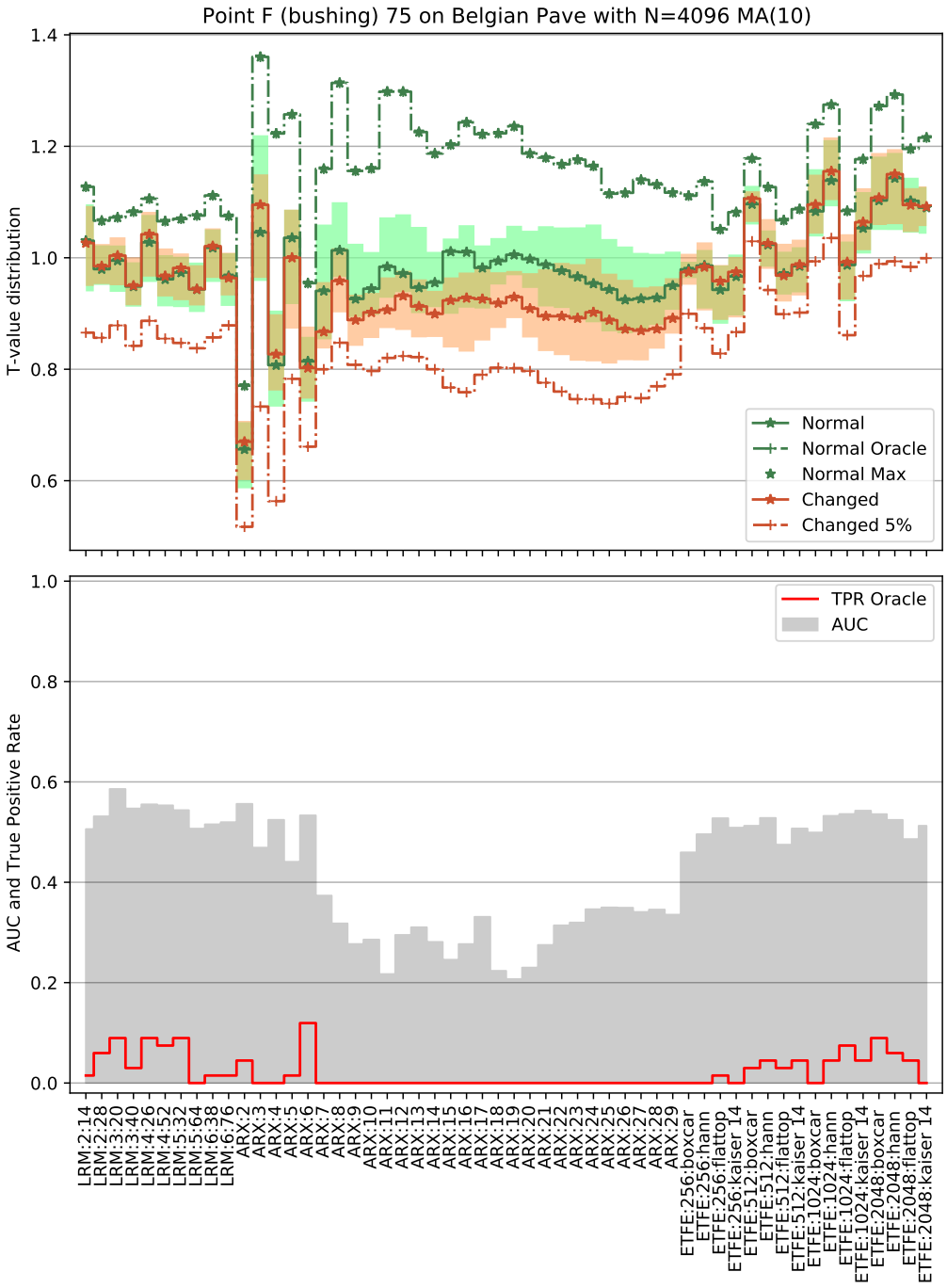
Point F (bushing) 75 on Belgian Pave with N=4096 MA(10)
T-value distribution
Normal
Normal Oracle
Normal Max
Changed
Changed 5%
AUC and True Positive Rate
TPR Oracle
AUC
LRM:2:14
LRM:2:28
LRM:3:20
LRM:3:40
LRM:4:26
LRM:4:52
LRM:5:32
LRM:5:64
LRM:6:38
LRM:6:76
ARX:2
ARX:3
ARX:4
ARX:5
ARX:6
ARX:7
ARX:8
ARX:9
ARX:10
ARX:11
ARX:12
ARX:13
ARX:14
ARX:15
ARX:16
ARX:17
ARX:18
ARX:19
ARX:20
ARX:21
ARX:22
ARX:23
ARX:24
ARX:25
ARX:26
ARX:27
ARX:28
ARX:29
ETFE:256:boxcar
ETFE:256:hann
ETFE:256:flattop
ETFE:256:kaiser 14
ETFE:512:boxcar
ETFE:512:hann
ETFE:512:flattop
ETFE:512:kaiser 14
ETFE:1024:boxcar
ETFE:1024:hann
ETFE:1024:flattop
ETFE:1024:kaiser 14
ETFE:2048:boxcar
ETFE:2048:hann
ETFE:2048:flattop
ETFE:2048:kaiser 14

Figure A.18

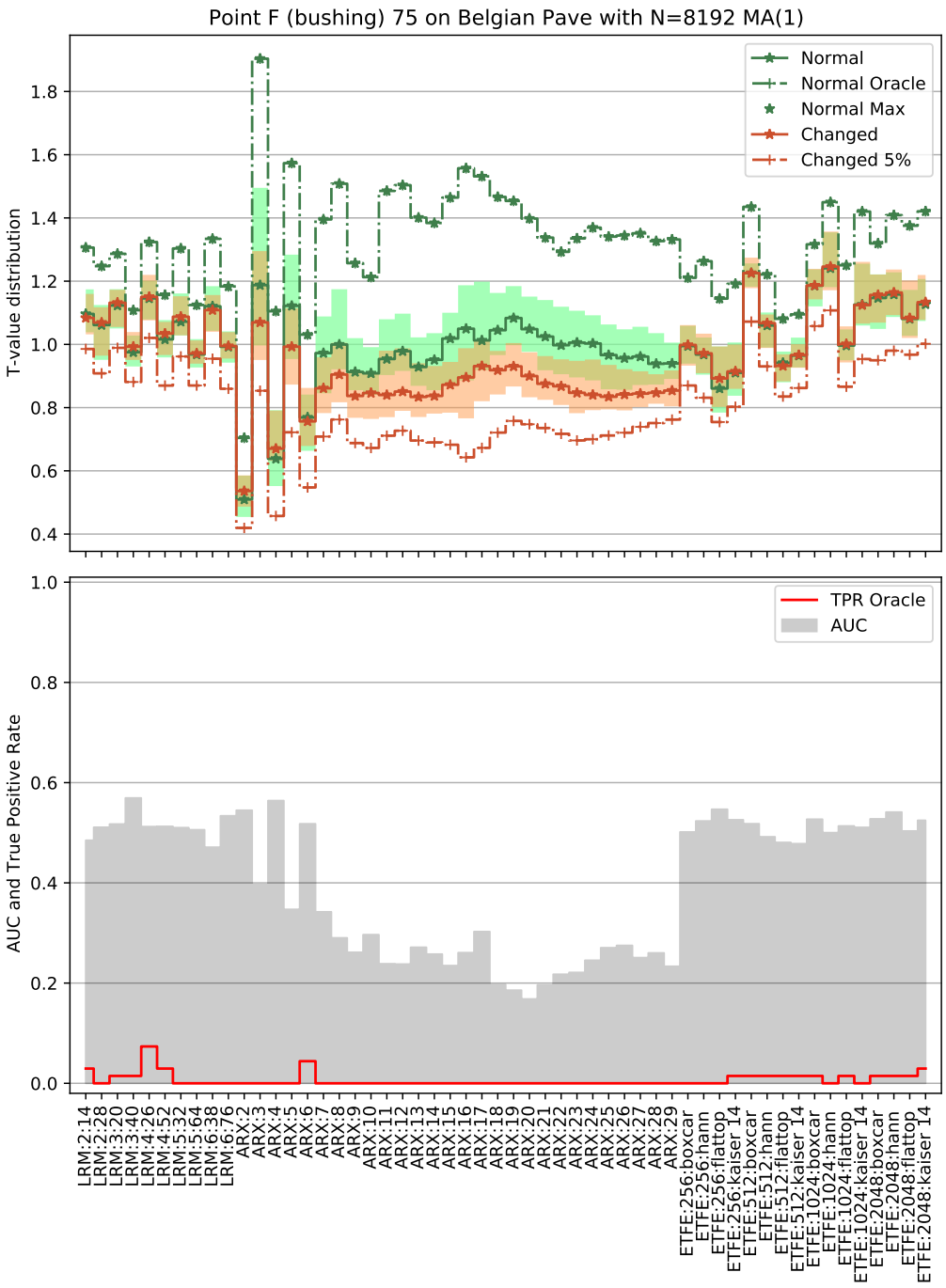
Point F (bushing) 75 on Belgian Pave with N=8192 MA(1)
Normal
Normal Oracle
Normal Max
Changed
Changed 5%
T-value distribution
TPR Oracle
AUC
AUC and True Positive Rate
LRM:2:14
LRM:2:28
LRM:3:20
LRM:3:40
LRM:4:26
LRM:4:52
LRM:5:32
LRM:5:64
LRM:6:38
LRM:6:76
ARX:2
ARX:3
ARX:4
ARX:5
ARX:6
ARX:7
ARX:8
ARX:9
ARX:10
ARX:11
ARX:12
ARX:13
ARX:14
ARX:15
ARX:16
ARX:17
ARX:18
ARX:19
ARX:20
ARX:21
ARX:22
ARX:23
ARX:24
ARX:25
ARX:26
ARX:27
ARX:28
ARX:29
ETFE:256:boxcar
ETFE:256:hann
ETFE:256:flattop
ETFE:256:kaiser 14
ETFE:512:boxcar
ETFE:512:hann
ETFE:512:flattop
ETFE:512:kaiser 14
ETFE:1024:boxcar
ETFE:1024:hann
ETFE:1024:flattop
ETFE:1024:kaiser 14
ETFE:2048:boxcar
ETFE:2048:hann
ETFE:2048:flattop
ETFE:2048:kaiser 14

Figure A.19

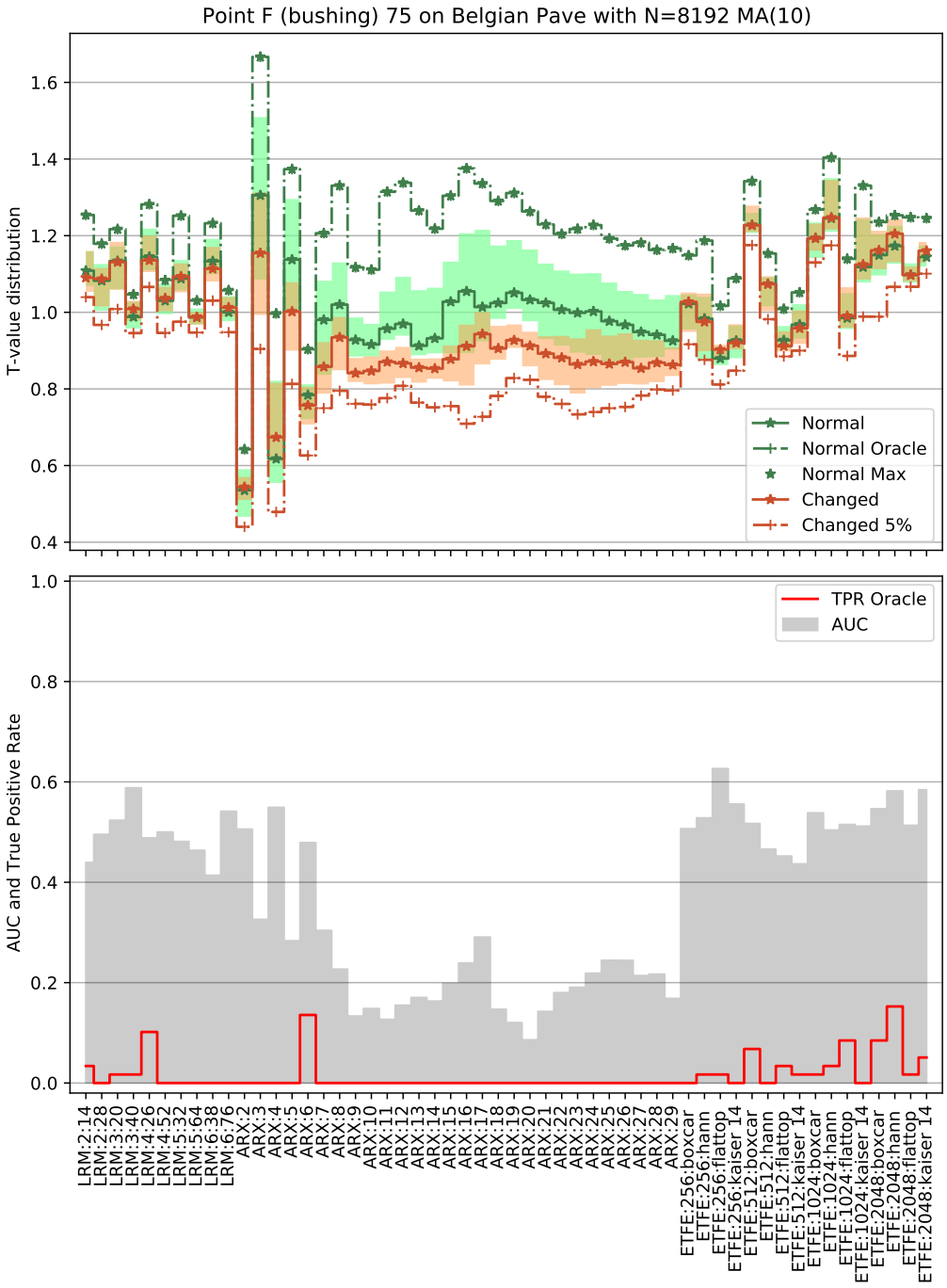
Point F (bushing) 75 on Belgian Pave with N=8192 MA(10)
T-value distribution
Normal
Normal Oracle
Normal Max
Changed
Changed 5%
AUC and True Positive Rate
TPR Oracle
AUC
LRM:2:14
LRM:2:28
LRM:3:20
LRM:3:40
LRM:4:26
LRM:4:52
LRM:5:32
LRM:5:64
LRM:6:38
LRM:6:76
ARX:2
ARX:3
ARX:4
ARX:5
ARX:6
ARX:7
ARX:8
ARX:9
ARX:10
ARX:11
ARX:12
ARX:13
ARX:14
ARX:15
ARX:16
ARX:17
ARX:18
ARX:19
ARX:20
ARX:21
ARX:22
ARX:23
ARX:24
ARX:25
ARX:26
ARX:27
ARX:28
ARX:29
ETFE:256:boxcar
ETFE:256:hann
ETFE:256:flattop
ETFE:256:kaiser 14
ETFE:512:boxcar
ETFE:512:hann
ETFE:512:flattop
ETFE:512:kaiser 14
ETFE:1024:boxcar
ETFE:1024:hann
ETFE:1024:flattop
ETFE:1024:kaiser 14
ETFE:2048:boxcar
ETFE:2048:hann
ETFE:2048:flattop
ETFE:2048:kaiser 14

Figure A.20

A.3 MBS: bushing 50% residual stiffness

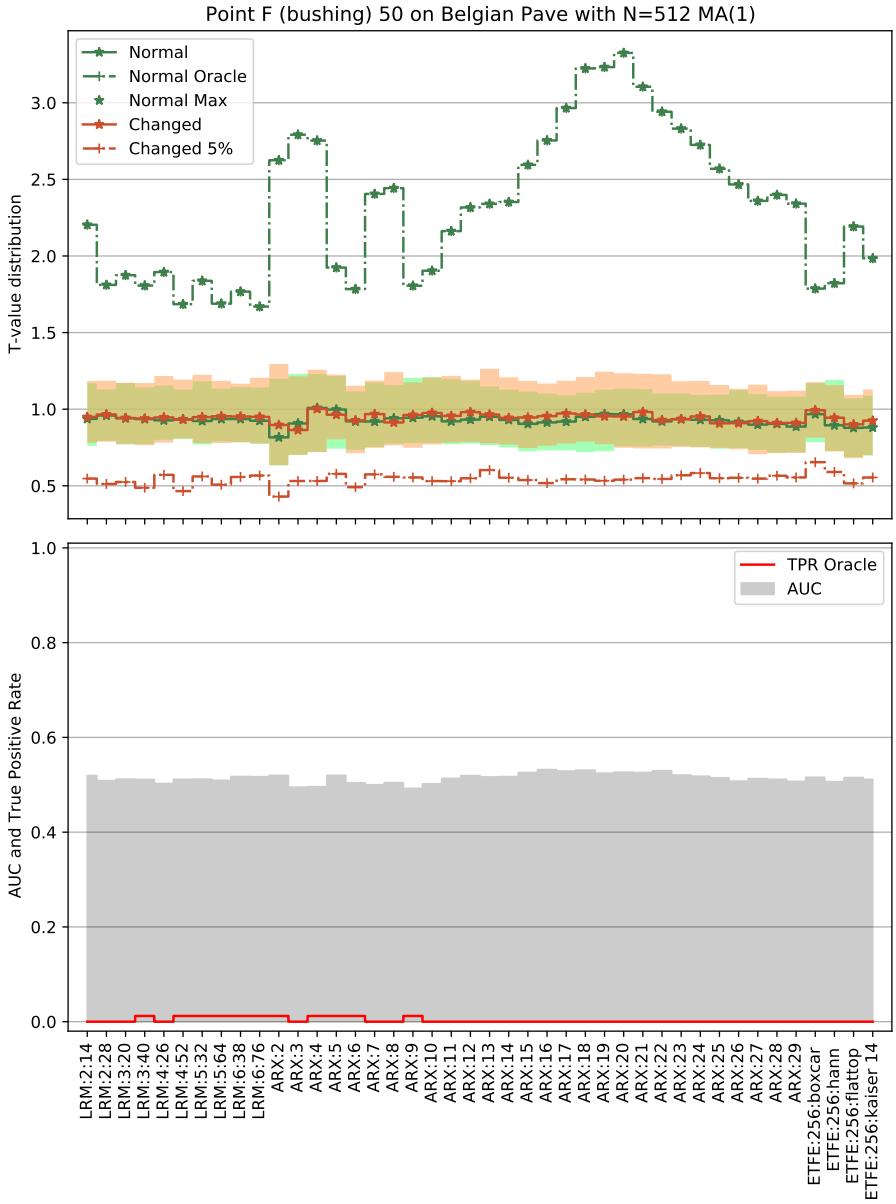

Figure A.21

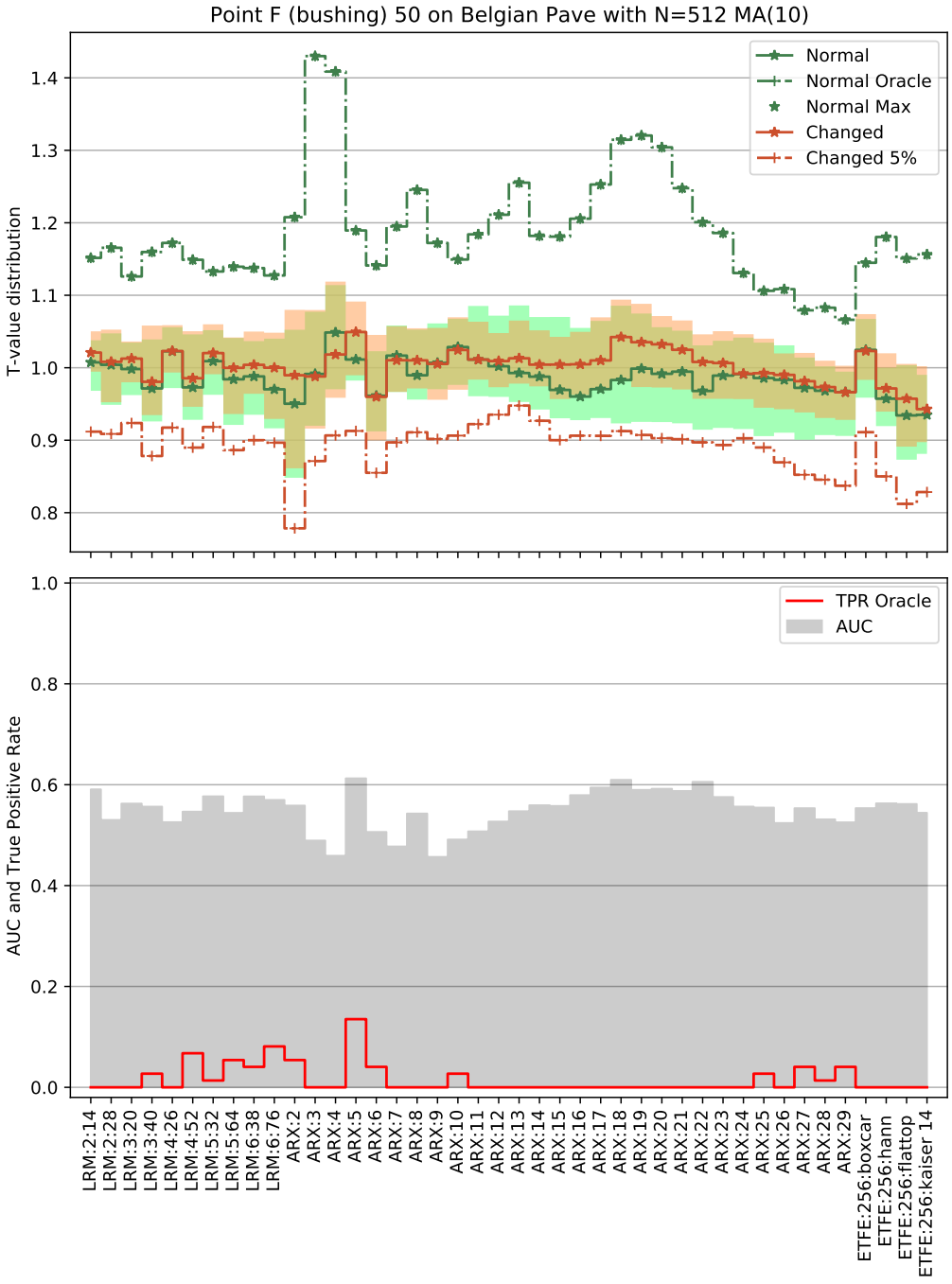
Point F (bushing) 50 on Belgian Pave with N=512 MA(10)
T-value distribution
Normal
Normal Oracle
Normal Max
Changed
Changed 5%
AUC and True Positive Rate
TPR Oracle
AUC
LRM:2:14
LRM:2:28
LRM:3:20
LRM:3:40
LRM:4:26
LRM:4:52
LRM:5:32
LRM:5:64
LRM:6:38
LRM:6:76
ARX:2
ARX:3
ARX:4
ARX:5
ARX:6
ARX:7
ARX:8
ARX:9
ARX:10
ARX:11
ARX:12
ARX:13
ARX:14
ARX:15
ARX:16
ARX:17
ARX:18
ARX:19
ARX:20
ARX:21
ARX:22
ARX:23
ARX:24
ARX:25
ARX:26
ARX:27
ARX:28
ARX:29
ETFE:256:boxcar
ETFE:256:hann
ETFE:256:flattop
ETFE:256:kaiser 14

Figure A.22

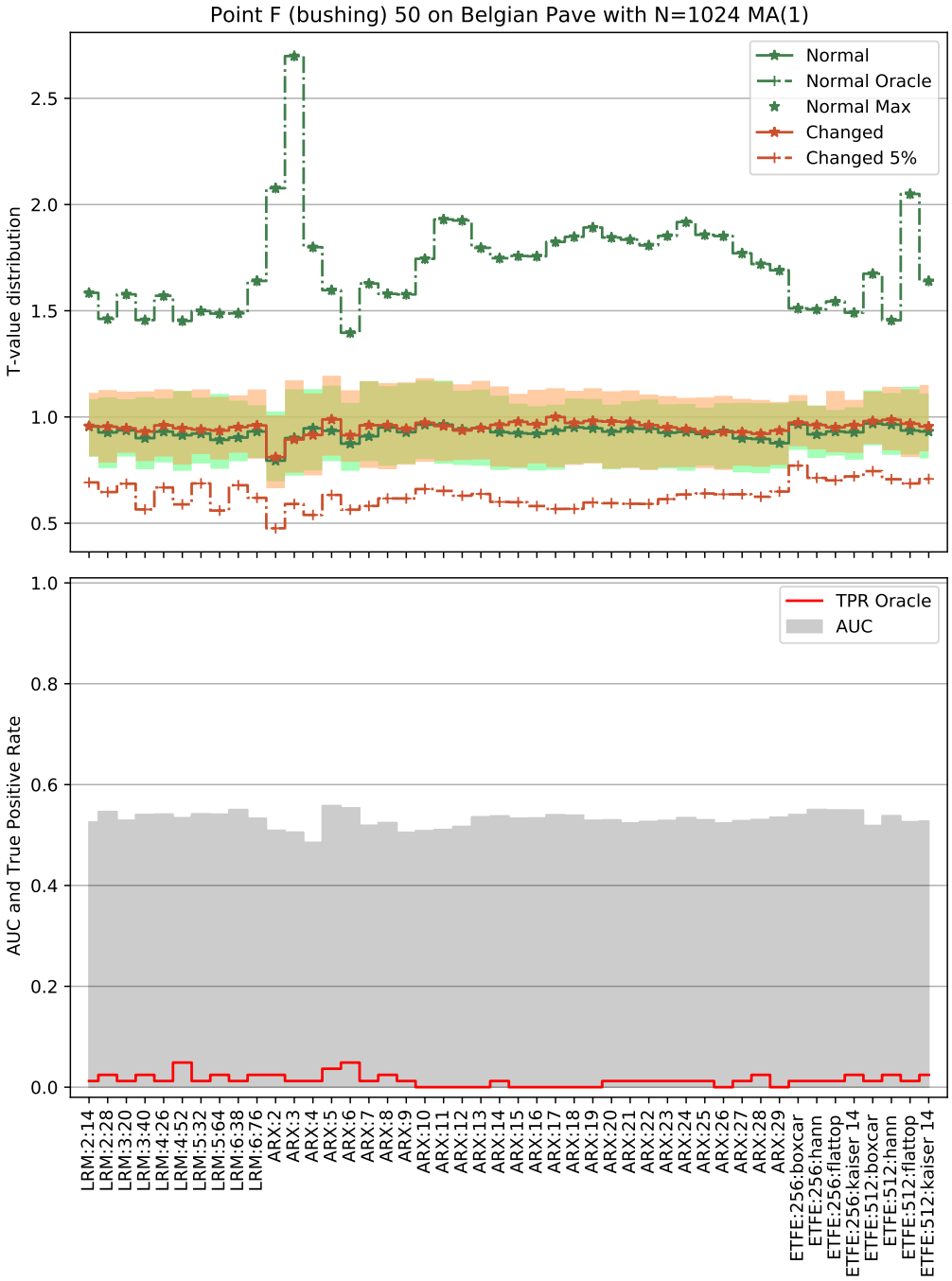
Point F (bushing) 50 on Belgian Pave with N=1024 MA(1)
Normal
Normal Oracle
Normal Max
Changed
Changed 5%
T-value distribution
2.5
2.0
1.5
1.0
0.5
TPR Oracle
AUC
AUC and True Positive Rate
1.0
0.8
0.6
0.4
0.2
0.0
LRM:2:14
LRM:2:28
LRM:3:20
LRM:3:40
LRM:4:26
LRM:4:52
LRM:5:32
LRM:5:64
LRM:6:38
LRM:6:76
ARX:2
ARX:3
ARX:4
ARX:5
ARX:6
ARX:7
ARX:8
ARX:9
ARX:10
ARX:11
ARX:12
ARX:13
ARX:14
ARX:15
ARX:16
ARX:17
ARX:18
ARX:19
ARX:20
ARX:21
ARX:22
ARX:23
ARX:24
ARX:25
ARX:26
ARX:27
ARX:28
ARX:29
ETFE:256:boxcar
ETFE:256:hann
ETFE:256:flattop
ETFE:256:kaiser 14
ETFE:512:boxcar
ETFE:512:hann
ETFE:512:flattop
ETFE:512:kaiser 14

Figure A.23

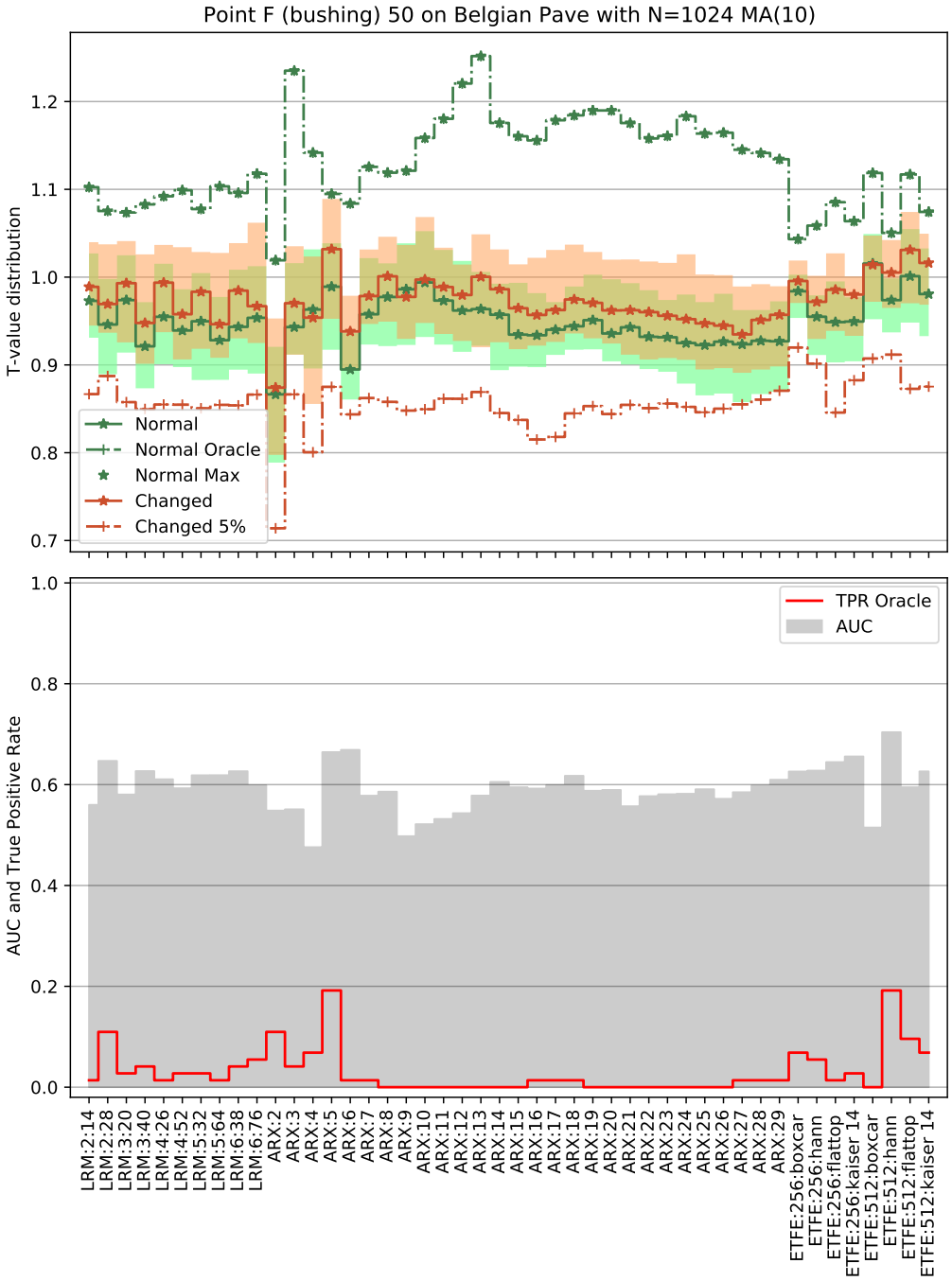
Point F (bushing) 50 on Belgian Pave with N=1024 MA(10)
T-value distribution
1.2
1.1
1.0
0.9
0.8
0.7
Normal
Normal Oracle
Normal Max
Changed
Changed 5%
AUC and True Positive Rate
1.0
0.8
0.6
0.4
0.2
0.0
TPR Oracle
AUC
LRM:2:14
LRM:2:28
LRM:3:20
LRM:3:40
LRM:4:26
LRM:4:52
LRM:5:32
LRM:5:64
LRM:6:38
LRM:6:76
ARX:2
ARX:3
ARX:4
ARX:5
ARX:6
ARX:7
ARX:8
ARX:9
ARX:10
ARX:11
ARX:12
ARX:13
ARX:14
ARX:15
ARX:16
ARX:17
ARX:18
ARX:19
ARX:20
ARX:21
ARX:22
ARX:23
ARX:24
ARX:25
ARX:26
ARX:27
ARX:28
ARX:29
ETFE:256:boxcar
ETFE:256:hann
ETFE:256:flattop
ETFE:256:kaiser 14
ETFE:512:boxcar
ETFE:512:hann
ETFE:512:flattop
ETFE:512:kaiser 14

Figure A.24

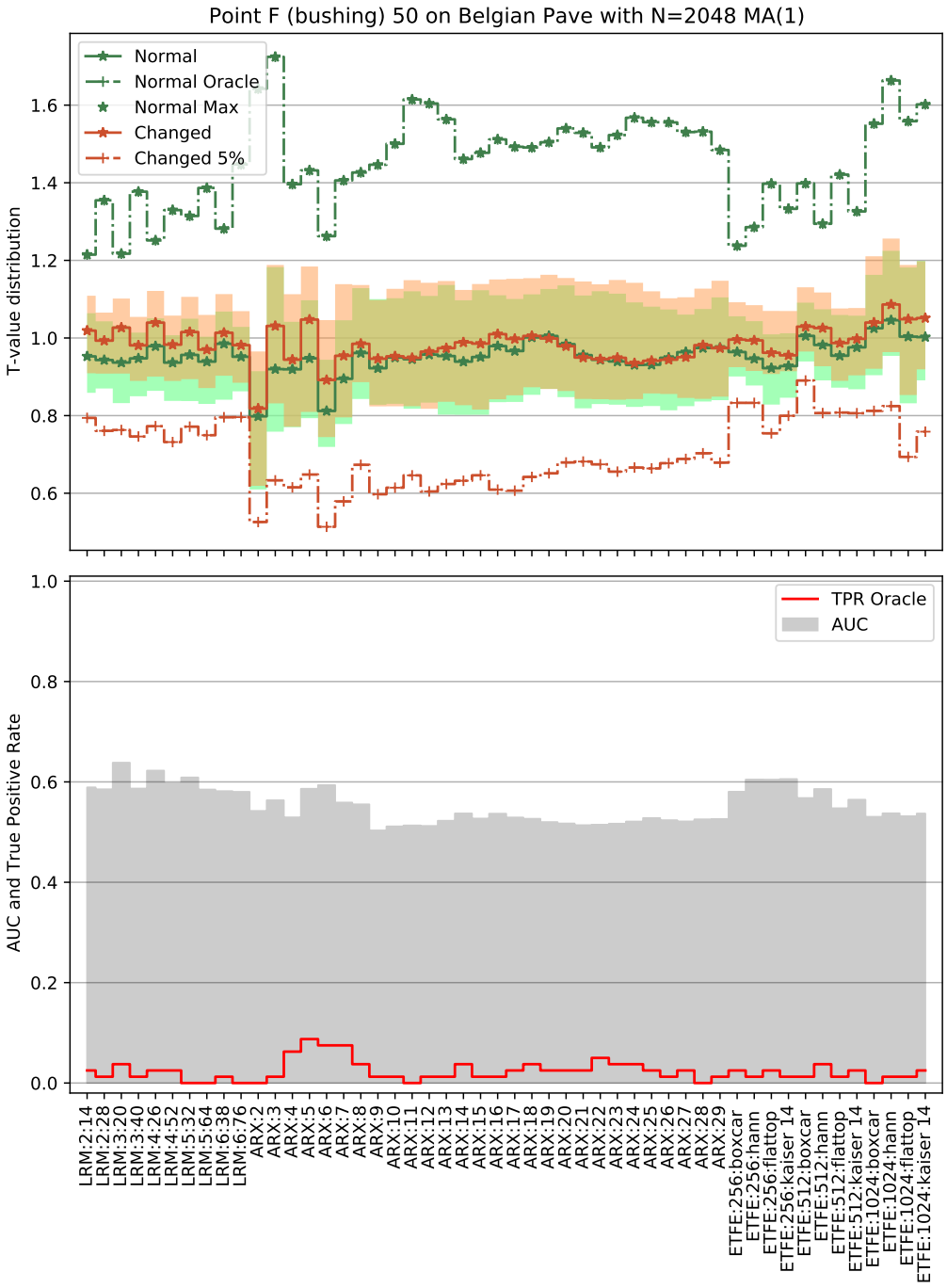
Point F (bushing) 50 on Belgian Pave with N=2048 MA(1)
Normal
Normal Oracle
Normal Max
Changed
Changed 5%
T-value distribution
1.6
1.4
1.2
1.0
0.8
0.6
TPR Oracle
AUC
AUC and True Positive Rate
1.0
0.8
0.6
0.4
0.2
0.0
LRM:2:14
LRM:2:28
LRM:3:20
LRM:3:40
LRM:4:26
LRM:4:52
LRM:5:32
LRM:5:64
LRM:6:38
LRM:6:76
ARX:2
ARX:3
ARX:4
ARX:5
ARX:6
ARX:7
ARX:8
ARX:9
ARX:10
ARX:11
ARX:12
ARX:13
ARX:14
ARX:15
ARX:16
ARX:17
ARX:18
ARX:19
ARX:20
ARX:21
ARX:22
ARX:23
ARX:24
ARX:25
ARX:26
ARX:27
ARX:28
ARX:29
ETFE:256:boxcar
ETFE:256:hann
ETFE:256:flattop
ETFE:256:kaiser 14
ETFE:512:boxcar
ETFE:512:hann
ETFE:512:flattop
ETFE:512:kaiser 14
ETFE:1024:boxcar
ETFE:1024:hann
ETFE:1024:flattop
ETFE:1024:kaiser 14

Figure A.25

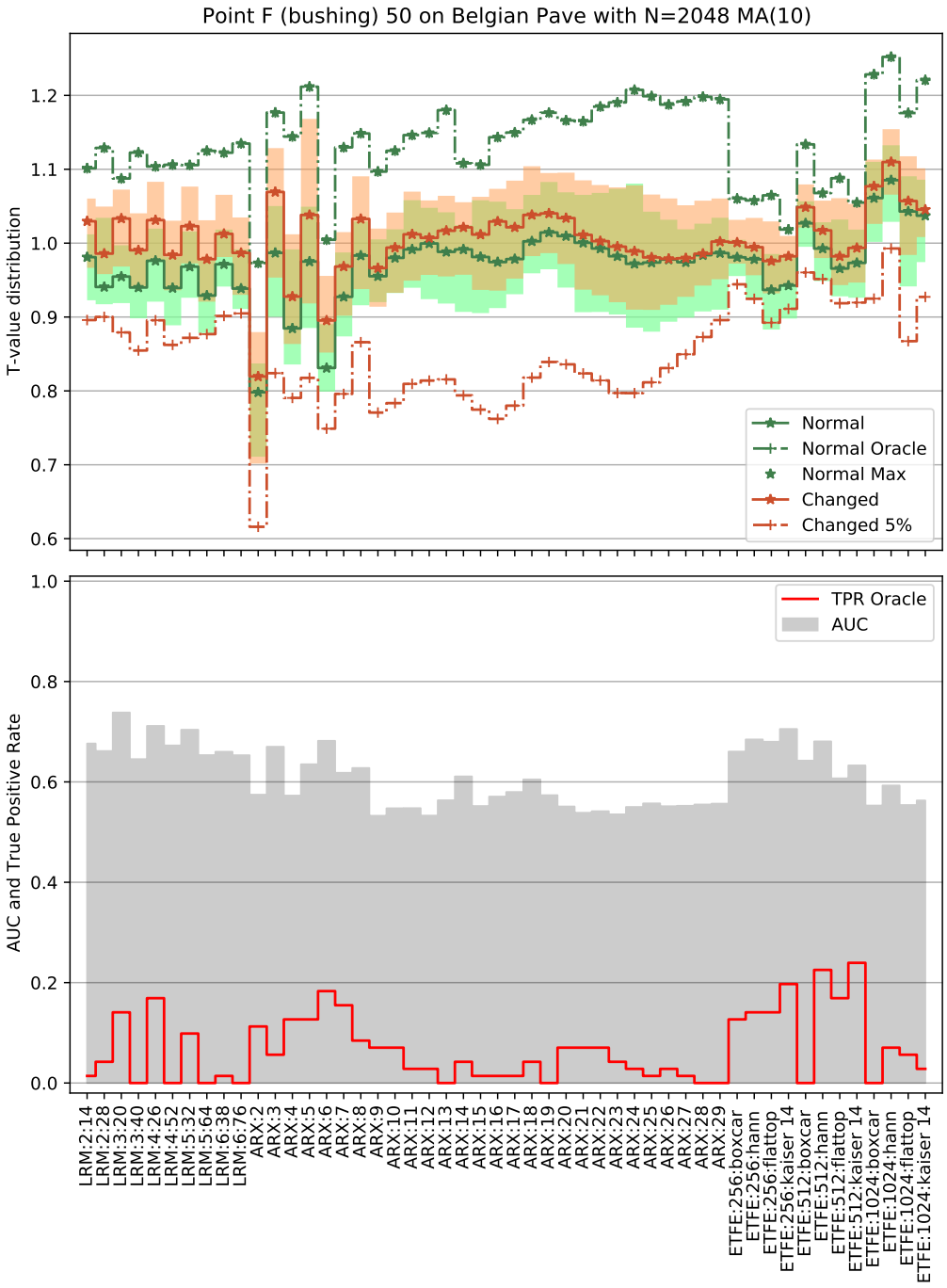
Point F (bushing) 50 on Belgian Pave with N=2048 MA(10)
T-value distribution
Normal
Normal Oracle
Normal Max
Changed
Changed 5%
AUC and True Positive Rate
TPR Oracle
AUC
LRM:2:14
LRM:2:28
LRM:3:20
LRM:3:40
LRM:4:26
LRM:4:52
LRM:5:32
LRM:5:64
LRM:6:38
LRM:6:76
ARX:2
ARX:3
ARX:4
ARX:5
ARX:6
ARX:7
ARX:8
ARX:9
ARX:10
ARX:11
ARX:12
ARX:13
ARX:14
ARX:15
ARX:16
ARX:17
ARX:18
ARX:19
ARX:20
ARX:21
ARX:22
ARX:23
ARX:24
ARX:25
ARX:26
ARX:27
ARX:28
ARX:29
ETFE:256:boxcar
ETFE:256:hann
ETFE:256:flattop
ETFE:256:kaiser 14
ETFE:512:boxcar
ETFE:512:hann
ETFE:512:flattop
ETFE:512:kaiser 14
ETFE:1024:boxcar
ETFE:1024:hann
ETFE:1024:flattop
ETFE:1024:kaiser 14

Figure A.26

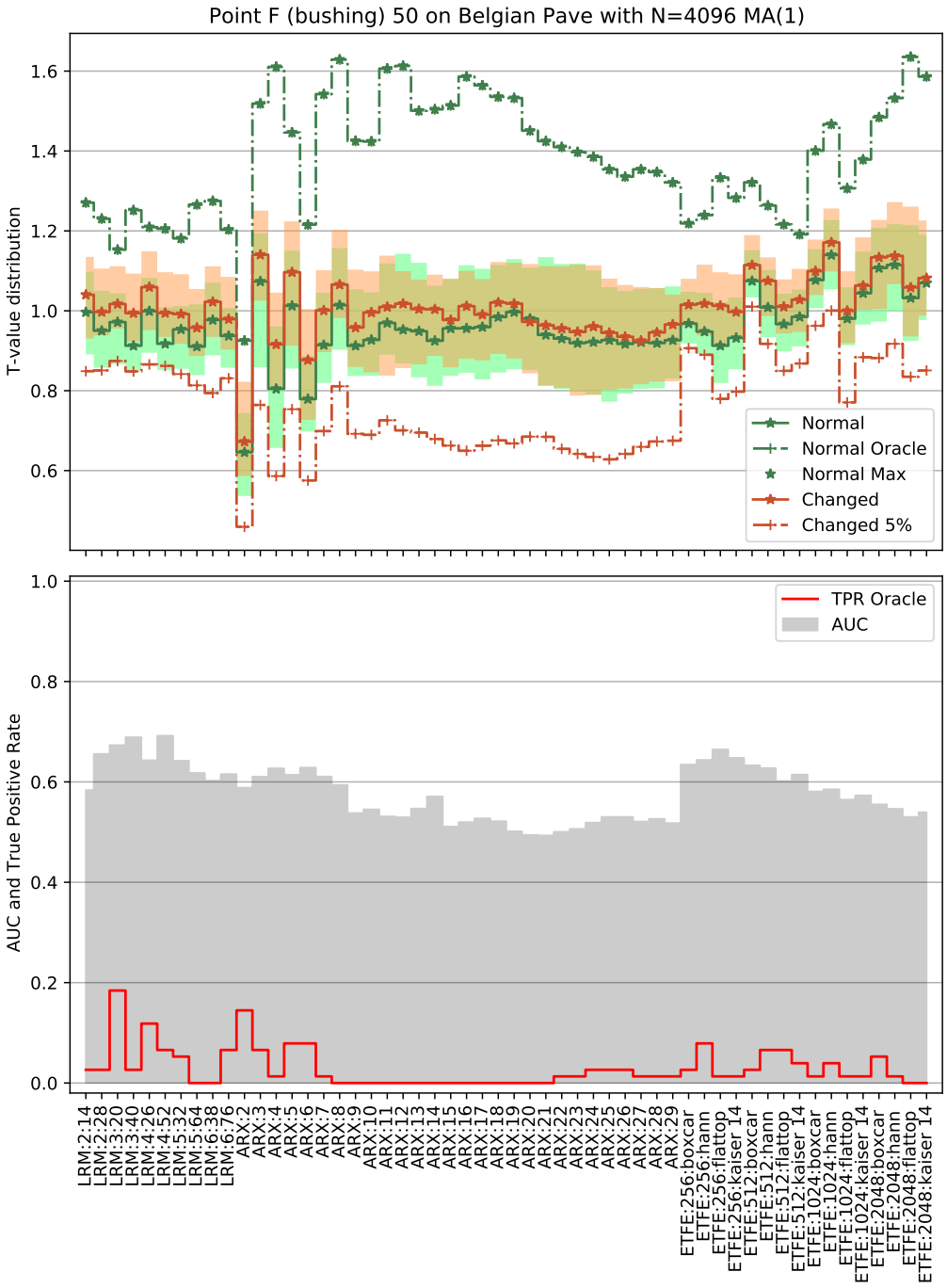
Point F (bushing) 50 on Belgian Pave with N=4096 MA(1)
T-value distribution
Normal
Normal Oracle
Normal Max
Changed
Changed 5%
AUC and True Positive Rate
TPR Oracle
AUC
LRM:2:14
LRM:2:28
LRM:3:20
LRM:3:40
LRM:4:26
LRM:4:52
LRM:5:32
LRM:5:64
LRM:6:38
LRM:6:76
ARX:2
ARX:3
ARX:4
ARX:5
ARX:6
ARX:7
ARX:8
ARX:9
ARX:10
ARX:11
ARX:12
ARX:13
ARX:14
ARX:15
ARX:16
ARX:17
ARX:18
ARX:19
ARX:20
ARX:21
ARX:22
ARX:23
ARX:24
ARX:25
ARX:26
ARX:27
ARX:28
ARX:29
ETFE:256:boxcar
ETFE:256:hann
ETFE:256:flattop
ETFE:256:kaiser 14
ETFE:512:boxcar
ETFE:512:hann
ETFE:512:flattop
ETFE:512:kaiser 14
ETFE:1024:boxcar
ETFE:1024:hann
ETFE:1024:flattop
ETFE:1024:kaiser 14
ETFE:2048:boxcar
ETFE:2048:hann
ETFE:2048:flattop
ETFE:2048:kaiser 14

Figure A.27

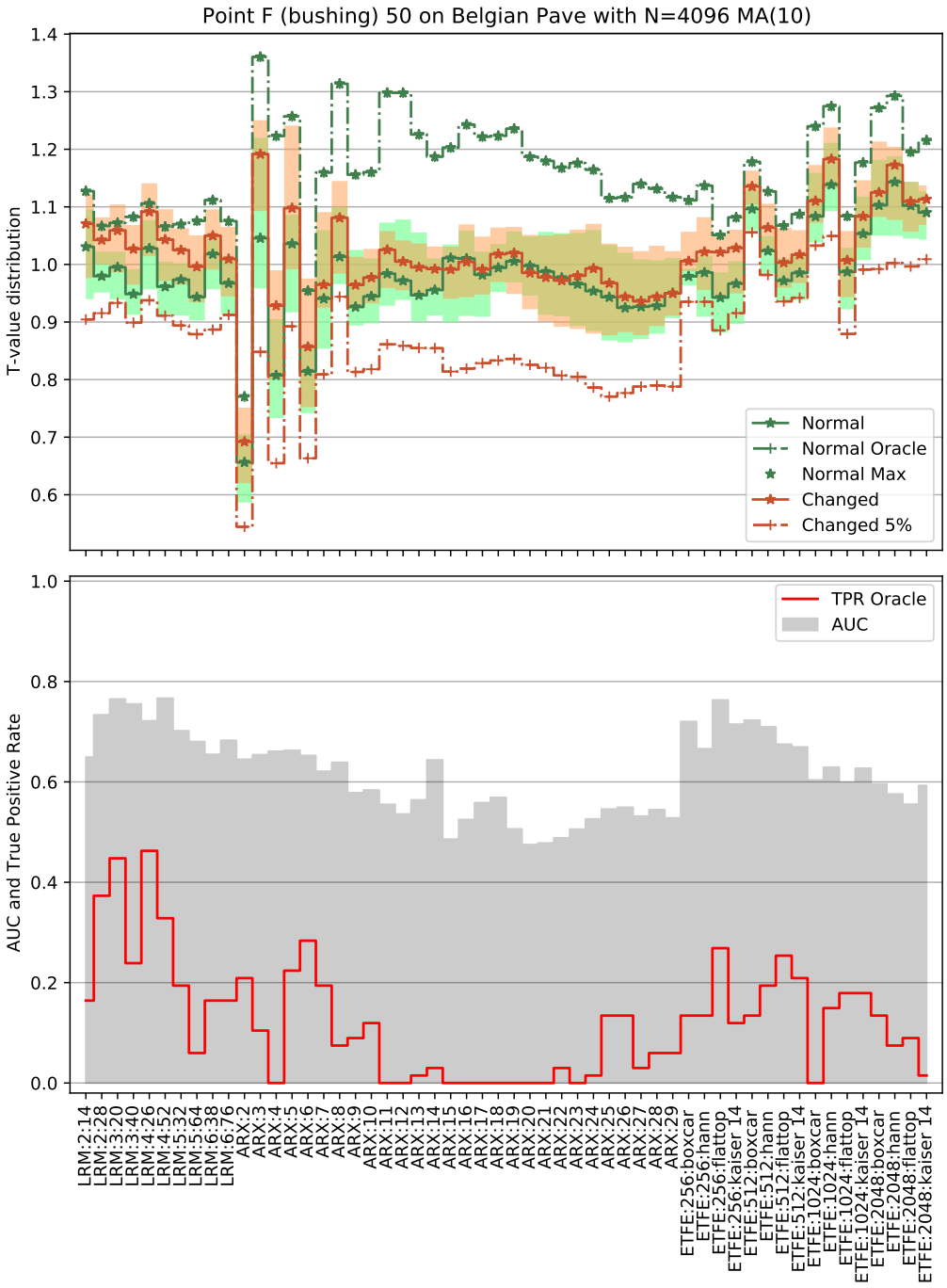
Point F (bushing) 50 on Belgian Pave with N=4096 MA(10)
T-value distribution
Normal
Normal Oracle
Normal Max
Changed
Changed 5%
AUC and True Positive Rate
TPR Oracle
AUC
LRM:2:14
LRM:2:28
LRM:3:20
LRM:3:40
LRM:4:26
LRM:4:52
LRM:5:32
LRM:5:64
LRM:6:38
LRM:6:76
ARX:2
ARX:3
ARX:4
ARX:5
ARX:6
ARX:7
ARX:8
ARX:9
ARX:10
ARX:11
ARX:12
ARX:13
ARX:14
ARX:15
ARX:16
ARX:17
ARX:18
ARX:19
ARX:20
ARX:21
ARX:22
ARX:23
ARX:24
ARX:25
ARX:26
ARX:27
ARX:28
ARX:29
ETFE:256:boxcar
ETFE:256:hann
ETFE:256:flattop
ETFE:256:kaiser 14
ETFE:512:boxcar
ETFE:512:hann
ETFE:512:flattop
ETFE:512:kaiser 14
ETFE:1024:boxcar
ETFE:1024:hann
ETFE:1024:flattop
ETFE:1024:kaiser 14
ETFE:2048:boxcar
ETFE:2048:hann
ETFE:2048:flattop
ETFE:2048:kaiser 14

Figure A.28

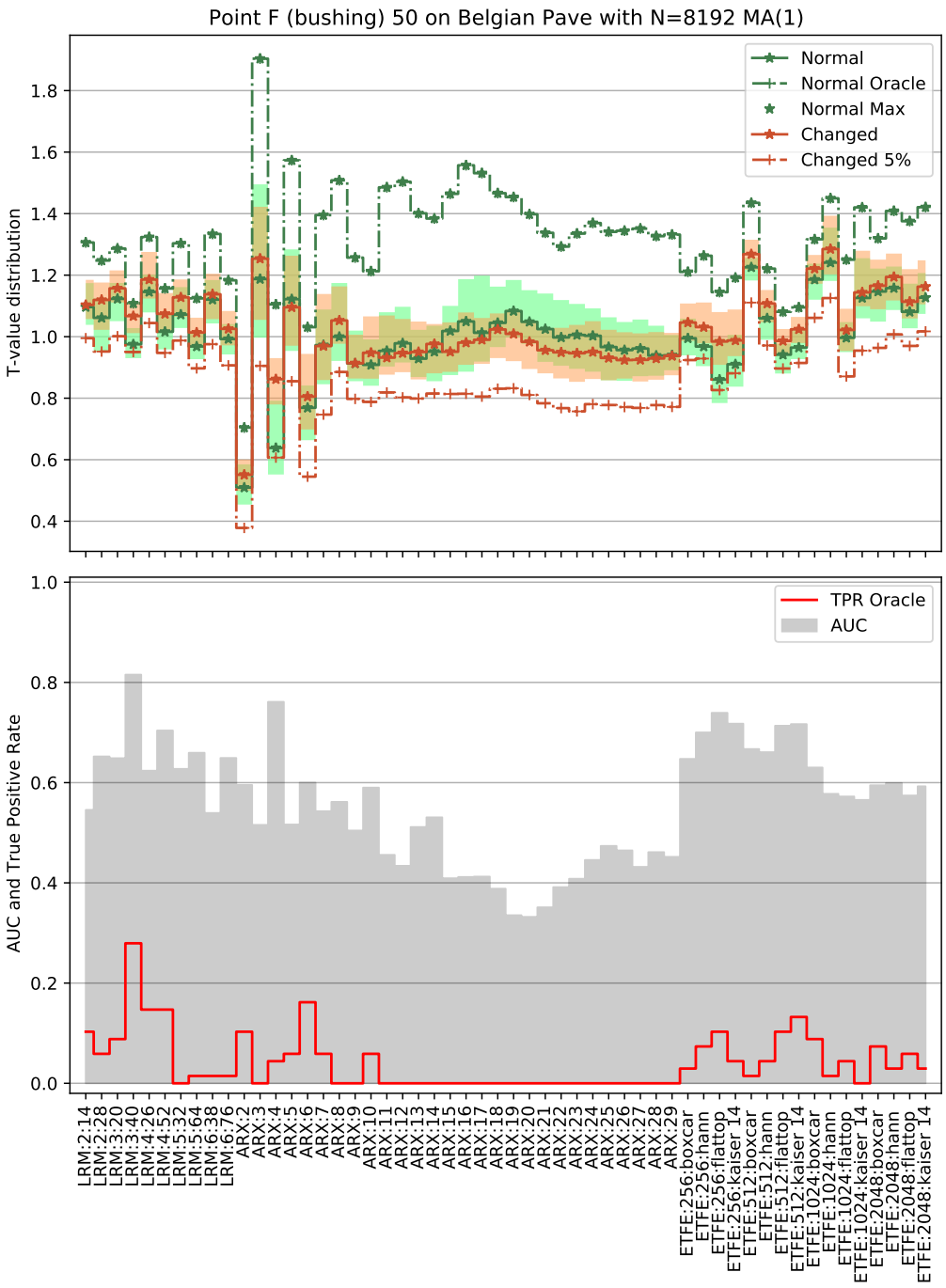
Point F (bushing) 50 on Belgian Pave with N=8192 MA(1)
Normal
Normal Oracle
Normal Max
Changed
Changed 5%
T-value distribution
TPR Oracle
AUC
AUC and True Positive Rate
LRM:2:14
LRM:2:28
LRM:3:20
LRM:3:40
LRM:4:26
LRM:4:52
LRM:5:32
LRM:5:64
LRM:6:38
LRM:6:76
ARX:2
ARX:3
ARX:4
ARX:5
ARX:6
ARX:7
ARX:8
ARX:9
ARX:10
ARX:11
ARX:12
ARX:13
ARX:14
ARX:15
ARX:16
ARX:17
ARX:18
ARX:19
ARX:20
ARX:21
ARX:22
ARX:23
ARX:24
ARX:25
ARX:26
ARX:27
ARX:28
ARX:29
ETFE:256:boxcar
ETFE:256:hann
ETFE:256:flattop
ETFE:256:kaiser 14
ETFE:512:boxcar
ETFE:512:hann
ETFE:512:flattop
ETFE:512:kaiser 14
ETFE:1024:boxcar
ETFE:1024:hann
ETFE:1024:flattop
ETFE:1024:kaiser 14
ETFE:2048:boxcar
ETFE:2048:hann
ETFE:2048:flattop
ETFE:2048:kaiser 14

Figure A.29

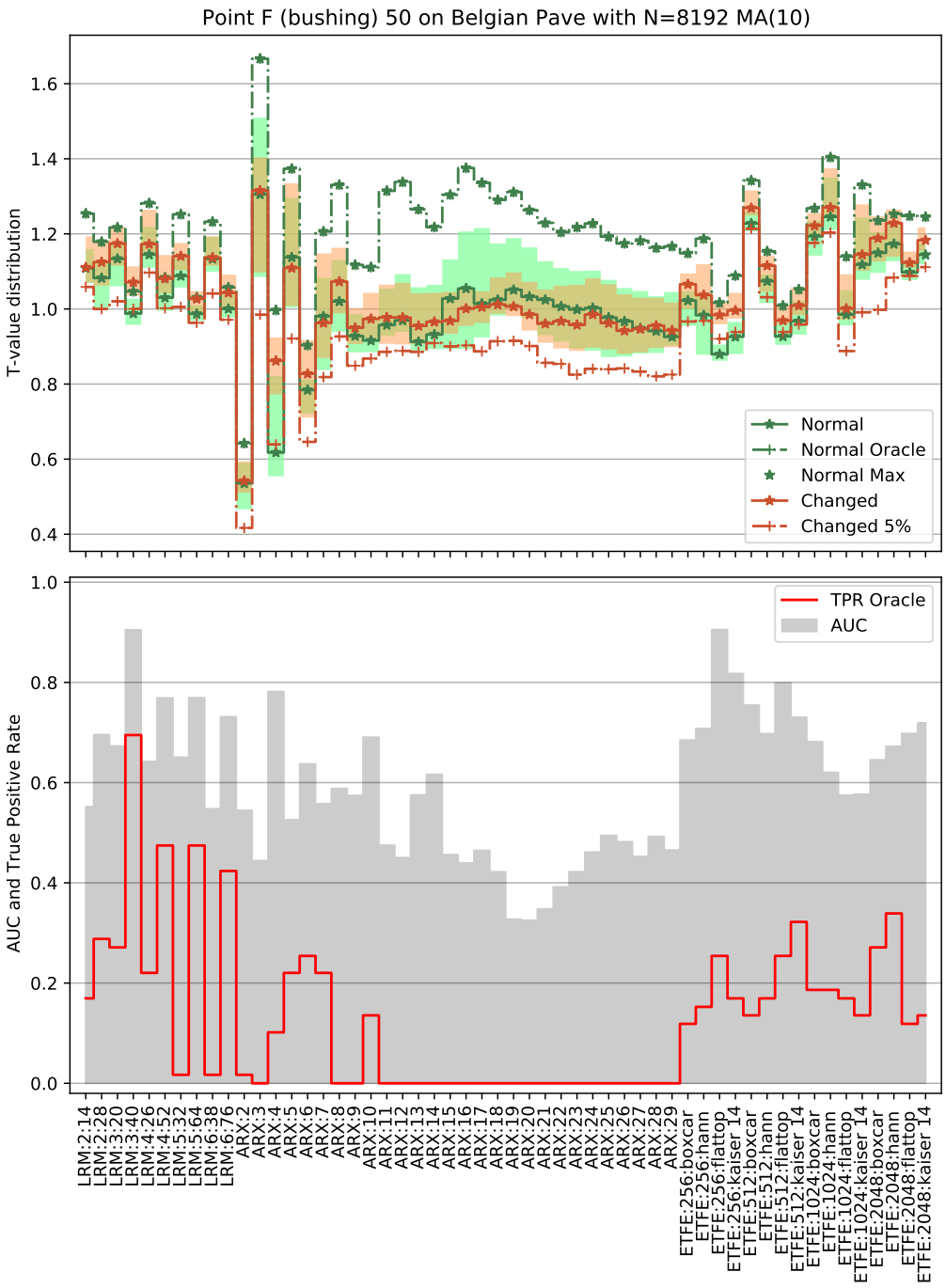
Point F (bushing) 50 on Belgian Pave with N=8192 MA(10)
T-value distribution
Normal
Normal Oracle
Normal Max
Changed
Changed 5%
AUC and True Positive Rate
TPR Oracle
AUC
LRM:2:14
LRM:2:28
LRM:3:20
LRM:3:40
LRM:4:26
LRM:4:52
LRM:5:32
LRM:5:64
LRM:6:38
LRM:6:76
ARX:2
ARX:3
ARX:4
ARX:5
ARX:6
ARX:7
ARX:8
ARX:9
ARX:10
ARX:11
ARX:12
ARX:13
ARX:14
ARX:15
ARX:16
ARX:17
ARX:18
ARX:19
ARX:20
ARX:21
ARX:22
ARX:23
ARX:24
ARX:25
ARX:26
ARX:27
ARX:28
ARX:29
ETFE:256:boxcar
ETFE:256:hann
ETFE:256:flattop
ETFE:256:kaiser 14
ETFE:512:boxcar
ETFE:512:hann
ETFE:512:flattop
ETFE:512:kaiser 14
ETFE:1024:boxcar
ETFE:1024:hann
ETFE:1024:flattop
ETFE:1024:kaiser 14
ETFE:2048:boxcar
ETFE:2048:hann
ETFE:2048:flattop
ETFE:2048:kaiser 14

Figure A.30

A.4 MBS: bushing 25% residual stiffness

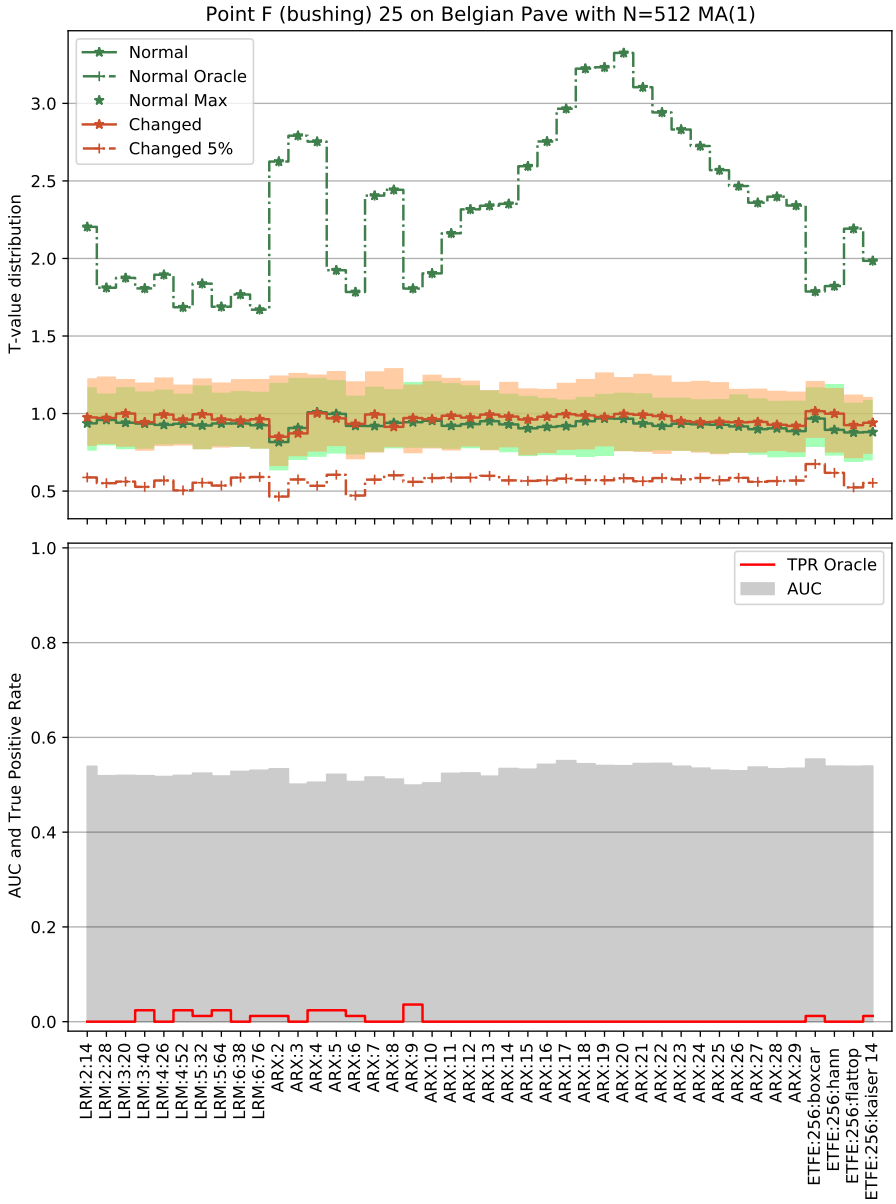

Figure A.31

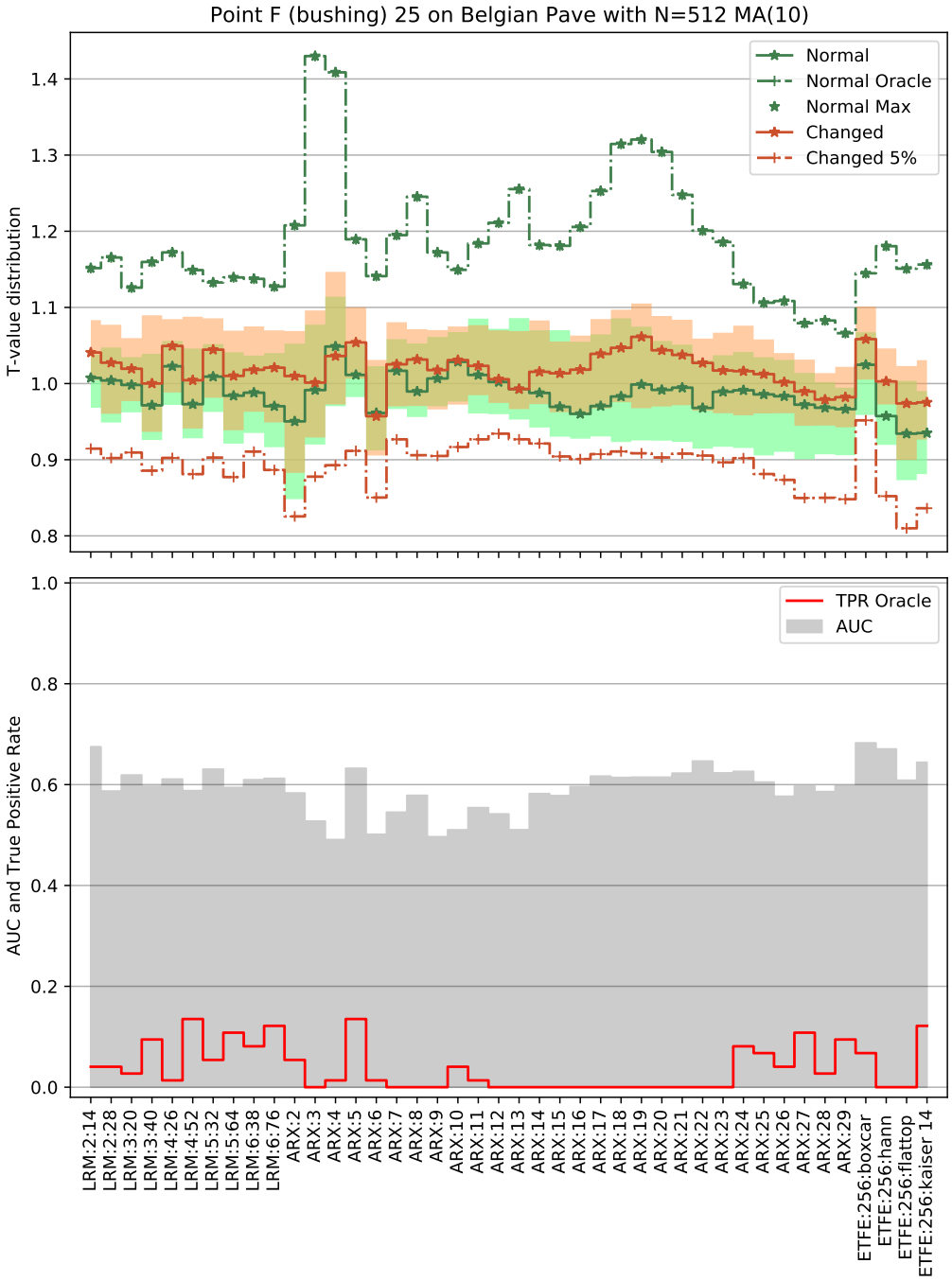
Point F (bushing) 25 on Belgian Pave with N=512 MA(10)
T-value distribution
Normal
Normal Oracle
Normal Max
Changed
Changed 5%
AUC and True Positive Rate
TPR Oracle
AUC
LRM:2:14
LRM:2:28
LRM:3:20
LRM:3:40
LRM:4:26
LRM:4:52
LRM:5:32
LRM:5:64
LRM:6:38
LRM:6:76
ARX:2
ARX:3
ARX:4
ARX:5
ARX:6
ARX:7
ARX:8
ARX:9
ARX:10
ARX:11
ARX:12
ARX:13
ARX:14
ARX:15
ARX:16
ARX:17
ARX:18
ARX:19
ARX:20
ARX:21
ARX:22
ARX:23
ARX:24
ARX:25
ARX:26
ARX:27
ARX:28
ARX:29
ETFE:256:boxcar
ETFE:256:hann
ETFE:256:flattop
ETFE:256:kaiser 14

Figure A.32

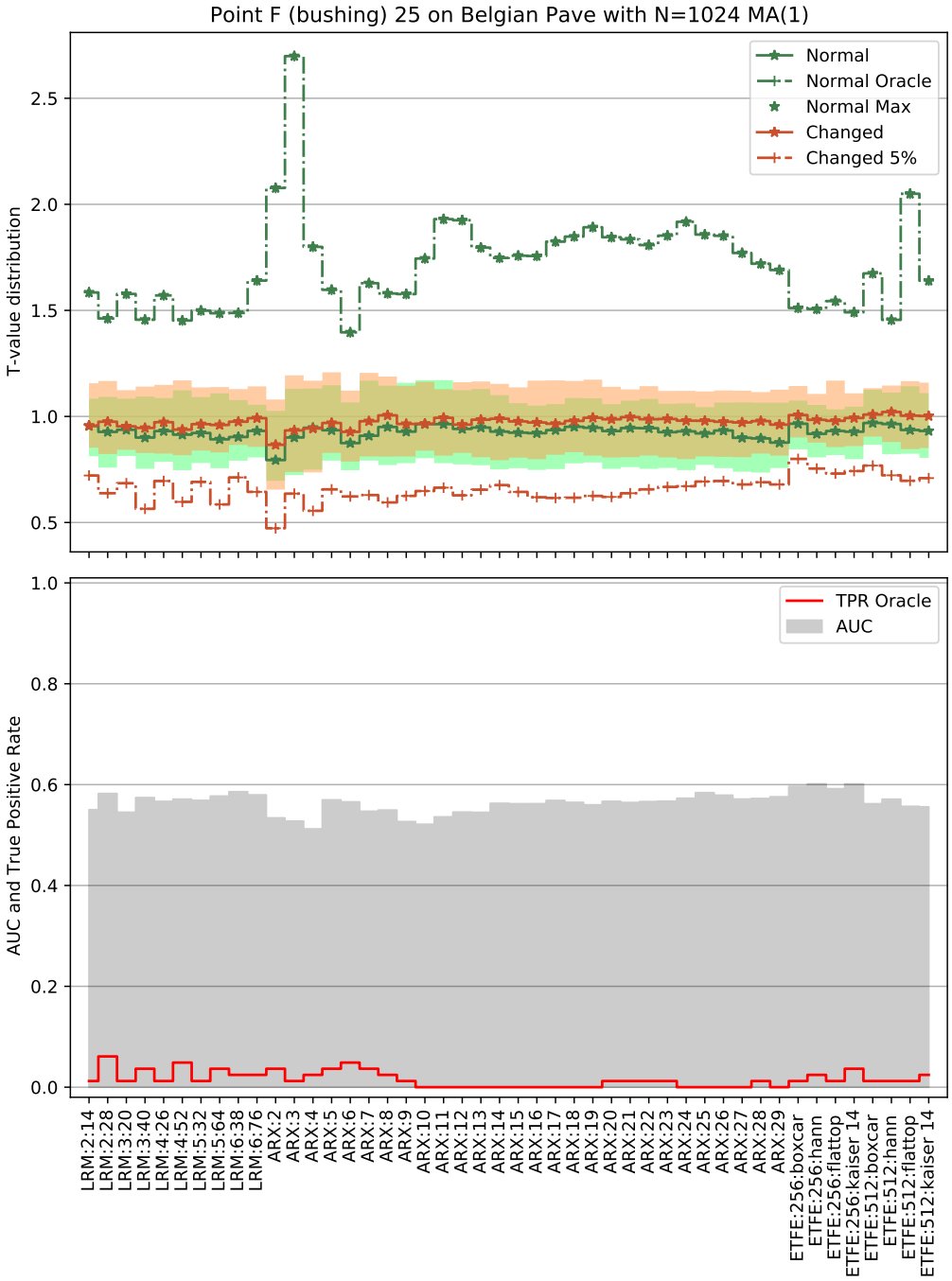
Point F (bushing) 25 on Belgian Pave with N=1024 MA(1)
Normal
Normal Oracle
Normal Max
Changed
Changed 5%
T-value distribution
2.5
2.0
1.5
1.0
0.5
TPR Oracle
AUC
AUC and True Positive Rate
1.0
0.8
0.6
0.4
0.2
0.0
LRM:2:14
LRM:2:28
LRM:3:20
LRM:3:40
LRM:4:26
LRM:4:52
LRM:5:32
LRM:5:64
LRM:6:38
LRM:6:76
ARX:2
ARX:3
ARX:4
ARX:5
ARX:6
ARX:7
ARX:8
ARX:9
ARX:10
ARX:11
ARX:12
ARX:13
ARX:14
ARX:15
ARX:16
ARX:17
ARX:18
ARX:19
ARX:20
ARX:21
ARX:22
ARX:23
ARX:24
ARX:25
ARX:26
ARX:27
ARX:28
ARX:29
ETFE:256:boxcar
ETFE:256:hann
ETFE:256:flattop
ETFE:256:kaiser 14
ETFE:512:boxcar
ETFE:512:hann
ETFE:512:flattop
ETFE:512:kaiser 14

Figure A.33

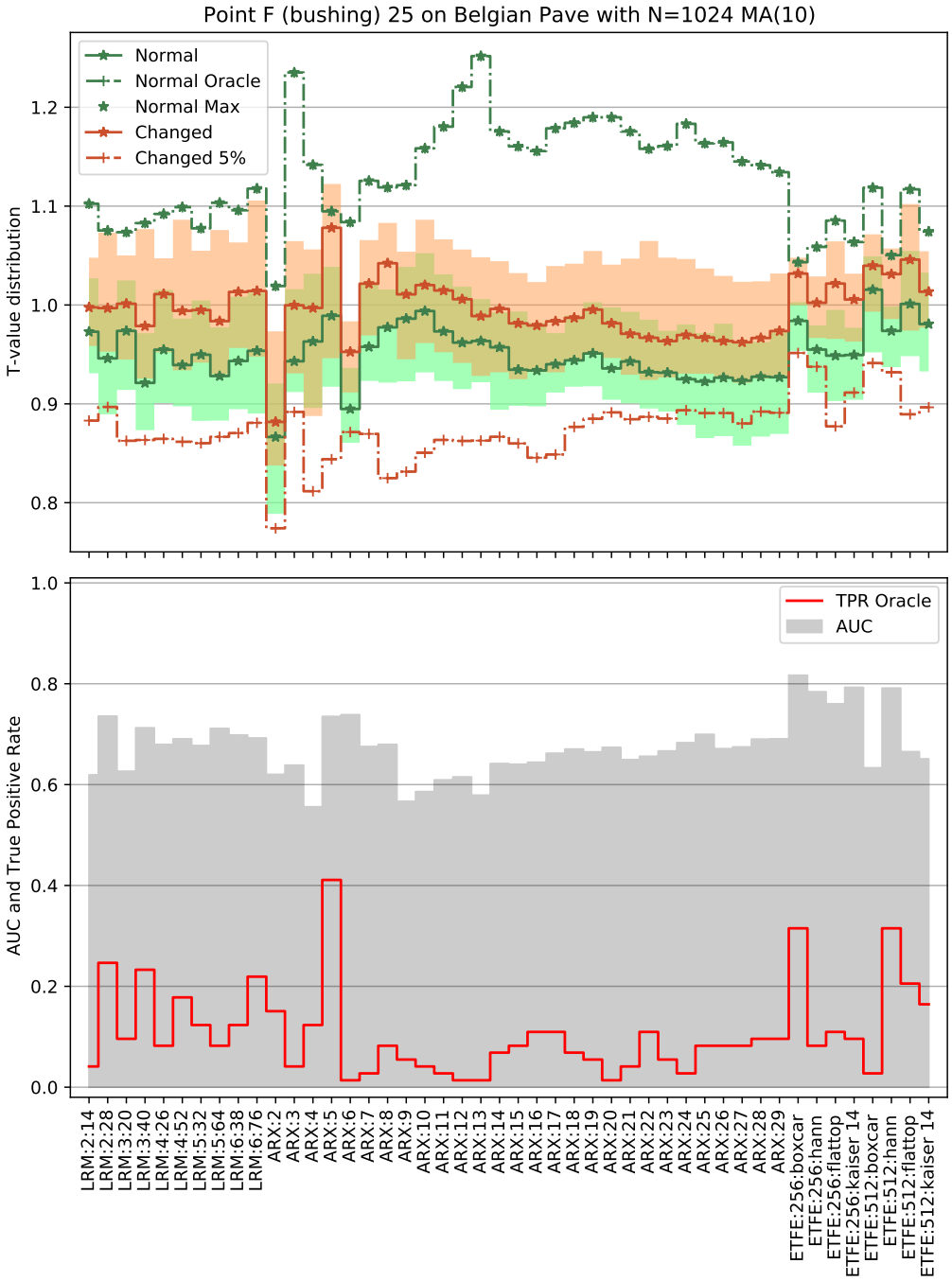
Point F (bushing) 25 on Belgian Pave with N=1024 MA(10)
Normal
Normal Oracle
Normal Max
Changed
Changed 5%
T-value distribution
1.2
1.1
1.0
0.9
0.8
TPR Oracle
AUC
AUC and True Positive Rate
1.0
0.8
0.6
0.4
0.2
0.0
LRM:2:14
LRM:2:28
LRM:3:20
LRM:3:40
LRM:4:26
LRM:4:52
LRM:5:32
LRM:5:64
LRM:6:38
LRM:6:76
ARX:2
ARX:3
ARX:4
ARX:5
ARX:6
ARX:7
ARX:8
ARX:9
ARX:10
ARX:11
ARX:12
ARX:13
ARX:14
ARX:15
ARX:16
ARX:17
ARX:18
ARX:19
ARX:20
ARX:21
ARX:22
ARX:23
ARX:24
ARX:25
ARX:26
ARX:27
ARX:28
ARX:29
ETFE:256:boxcar
ETFE:256:hann
ETFE:256:flattop
ETFE:256:kaiser 14
ETFE:512:boxcar
ETFE:512:hann
ETFE:512:flattop
ETFE:512:kaiser 14

Figure A.34

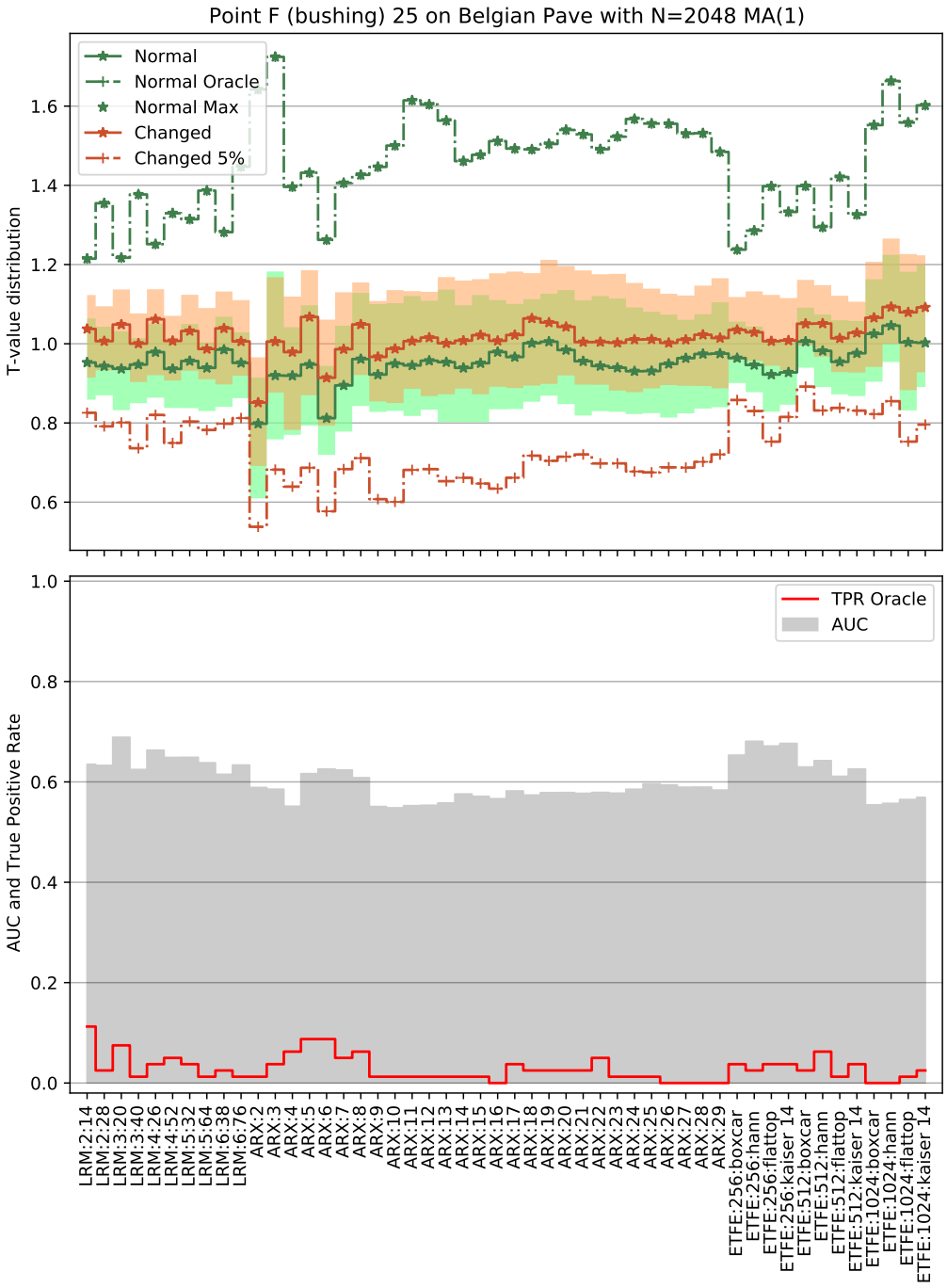
Point F (bushing) 25 on Belgian Pave with N=2048 MA(1)
Normal
Normal Oracle
Normal Max
Changed
Changed 5%
T-value distribution
1.6
1.4
1.2
1.0
0.8
0.6
TPR Oracle
AUC
AUC and True Positive Rate
1.0
0.8
0.6
0.4
0.2
0.0
LRM:2:14
LRM:2:28
LRM:3:20
LRM:3:40
LRM:4:26
LRM:4:52
LRM:5:32
LRM:5:64
LRM:6:38
LRM:6:76
ARX:2
ARX:3
ARX:4
ARX:5
ARX:6
ARX:7
ARX:8
ARX:9
ARX:10
ARX:11
ARX:12
ARX:13
ARX:14
ARX:15
ARX:16
ARX:17
ARX:18
ARX:19
ARX:20
ARX:21
ARX:22
ARX:23
ARX:24
ARX:25
ARX:26
ARX:27
ARX:28
ARX:29
ETFE:256:boxcar
ETFE:256:hann
ETFE:256:flattop
ETFE:256:kaiser 14
ETFE:512:boxcar
ETFE:512:hann
ETFE:512:flattop
ETFE:512:kaiser 14
ETFE:1024:boxcar
ETFE:1024:hann
ETFE:1024:flattop
ETFE:1024:kaiser 14

Figure A.35

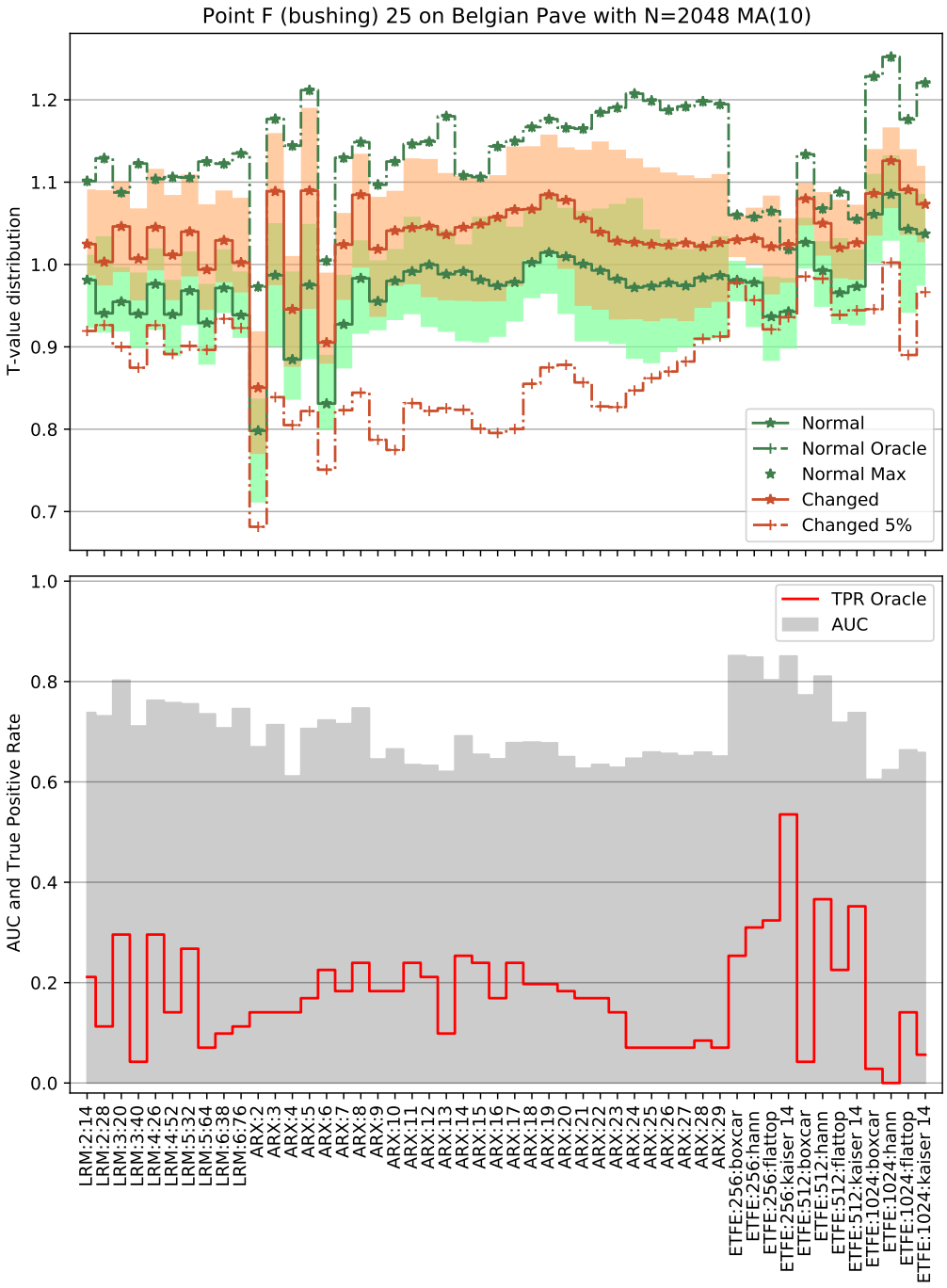
Point F (bushing) 25 on Belgian Pave with N=2048 MA(10)
T-value distribution
Normal
Normal Oracle
Normal Max
Changed
Changed 5%
AUC and True Positive Rate
TPR Oracle
AUC
LRM:2:14
LRM:2:28
LRM:3:20
LRM:3:40
LRM:4:26
LRM:4:52
LRM:5:32
LRM:5:64
LRM:6:38
LRM:6:76
ARX:2
ARX:3
ARX:4
ARX:5
ARX:6
ARX:7
ARX:8
ARX:9
ARX:10
ARX:11
ARX:12
ARX:13
ARX:14
ARX:15
ARX:16
ARX:17
ARX:18
ARX:19
ARX:20
ARX:21
ARX:22
ARX:23
ARX:24
ARX:25
ARX:26
ARX:27
ARX:28
ARX:29
ETFE:256:boxcar
ETFE:256:hann
ETFE:256:flattop
ETFE:256:kaiser 14
ETFE:512:boxcar
ETFE:512:hann
ETFE:512:flattop
ETFE:512:kaiser 14
ETFE:1024:boxcar
ETFE:1024:hann
ETFE:1024:flattop
ETFE:1024:kaiser 14

Figure A.36

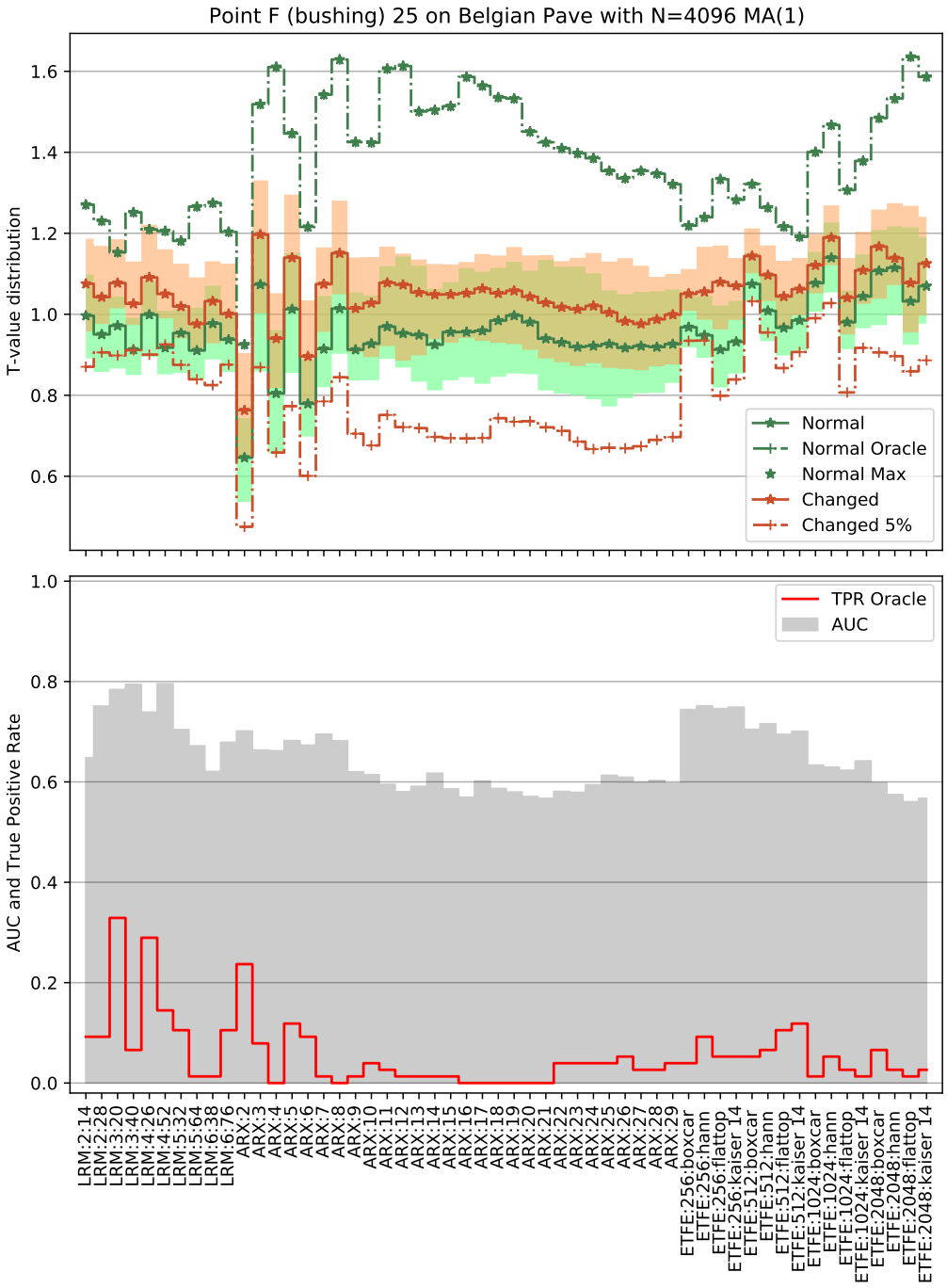
Point F (bushing) 25 on Belgian Pave with N=4096 MA(1)
T-value distribution
Normal
Normal Oracle
Normal Max
Changed
Changed 5%
AUC and True Positive Rate
TPR Oracle
AUC
LRM:2:14
LRM:2:28
LRM:3:20
LRM:3:40
LRM:4:26
LRM:4:52
LRM:5:32
LRM:5:64
LRM:6:38
LRM:6:76
ARX:2
ARX:3
ARX:4
ARX:5
ARX:6
ARX:7
ARX:8
ARX:9
ARX:10
ARX:11
ARX:12
ARX:13
ARX:14
ARX:15
ARX:16
ARX:17
ARX:18
ARX:19
ARX:20
ARX:21
ARX:22
ARX:23
ARX:24
ARX:25
ARX:26
ARX:27
ARX:28
ARX:29
ETFE:256:boxcar
ETFE:256:hann
ETFE:256:flattop
ETFE:256:kaiser 14
ETFE:512:boxcar
ETFE:512:hann
ETFE:512:flattop
ETFE:512:kaiser 14
ETFE:1024:boxcar
ETFE:1024:hann
ETFE:1024:flattop
ETFE:1024:kaiser 14
ETFE:2048:boxcar
ETFE:2048:hann
ETFE:2048:flattop
ETFE:2048:kaiser 14

Figure A.37

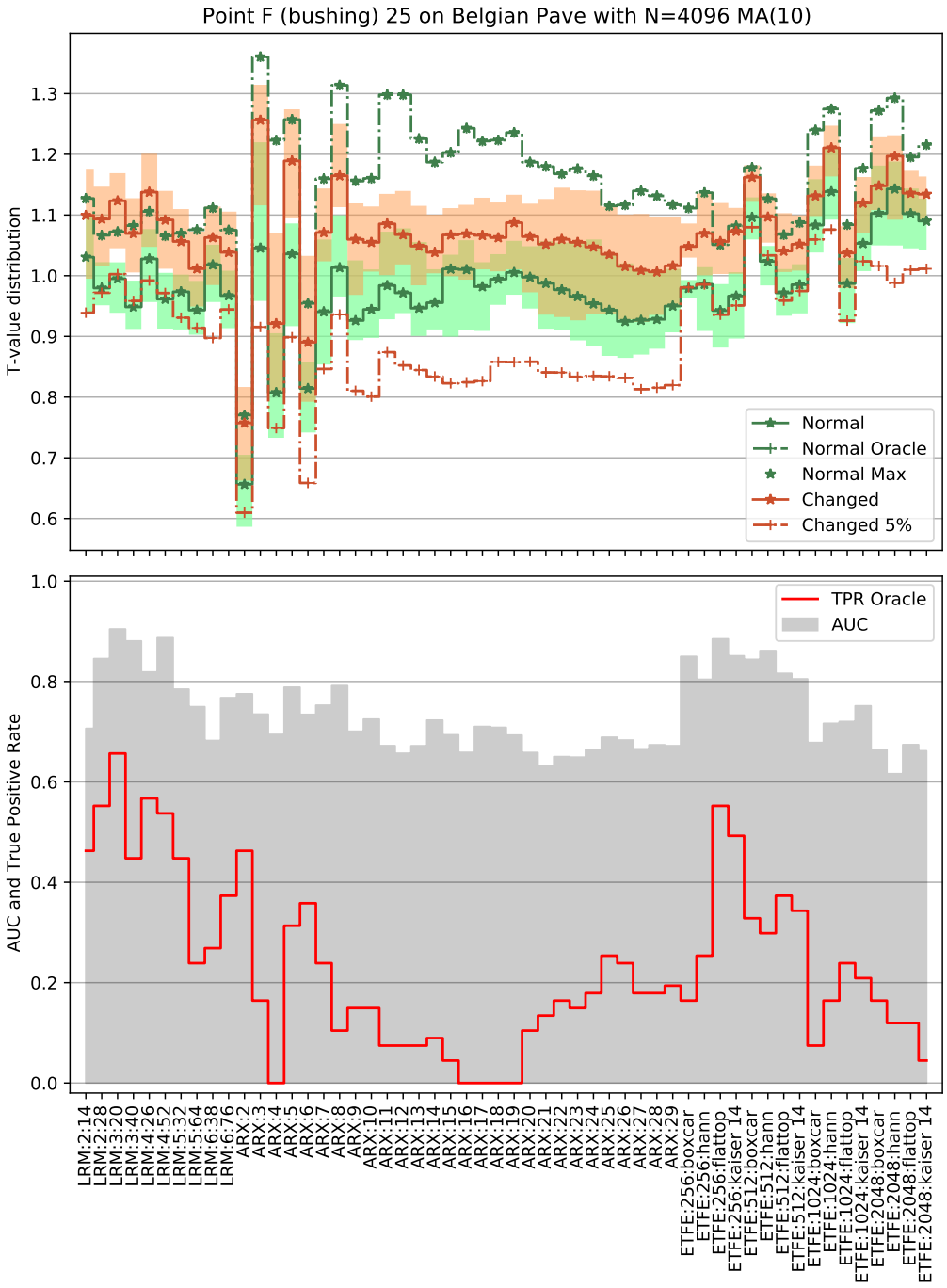
Point F (bushing) 25 on Belgian Pave with N=4096 MA(10)
T-value distribution
Normal
Normal Oracle
Normal Max
Changed
Changed 5%
AUC and True Positive Rate
TPR Oracle
AUC
LRM:2:14
LRM:2:28
LRM:3:20
LRM:3:40
LRM:4:26
LRM:4:52
LRM:5:32
LRM:5:64
LRM:6:38
LRM:6:76
ARX:2
ARX:3
ARX:4
ARX:5
ARX:6
ARX:7
ARX:8
ARX:9
ARX:10
ARX:11
ARX:12
ARX:13
ARX:14
ARX:15
ARX:16
ARX:17
ARX:18
ARX:19
ARX:20
ARX:21
ARX:22
ARX:23
ARX:24
ARX:25
ARX:26
ARX:27
ARX:28
ARX:29
ETFE:256:boxcar
ETFE:256:hann
ETFE:256:flattop
ETFE:256:kaiser 14
ETFE:512:boxcar
ETFE:512:hann
ETFE:512:flattop
ETFE:512:kaiser 14
ETFE:1024:boxcar
ETFE:1024:hann
ETFE:1024:flattop
ETFE:1024:kaiser 14
ETFE:2048:boxcar
ETFE:2048:hann
ETFE:2048:flattop
ETFE:2048:kaiser 14

Figure A.38

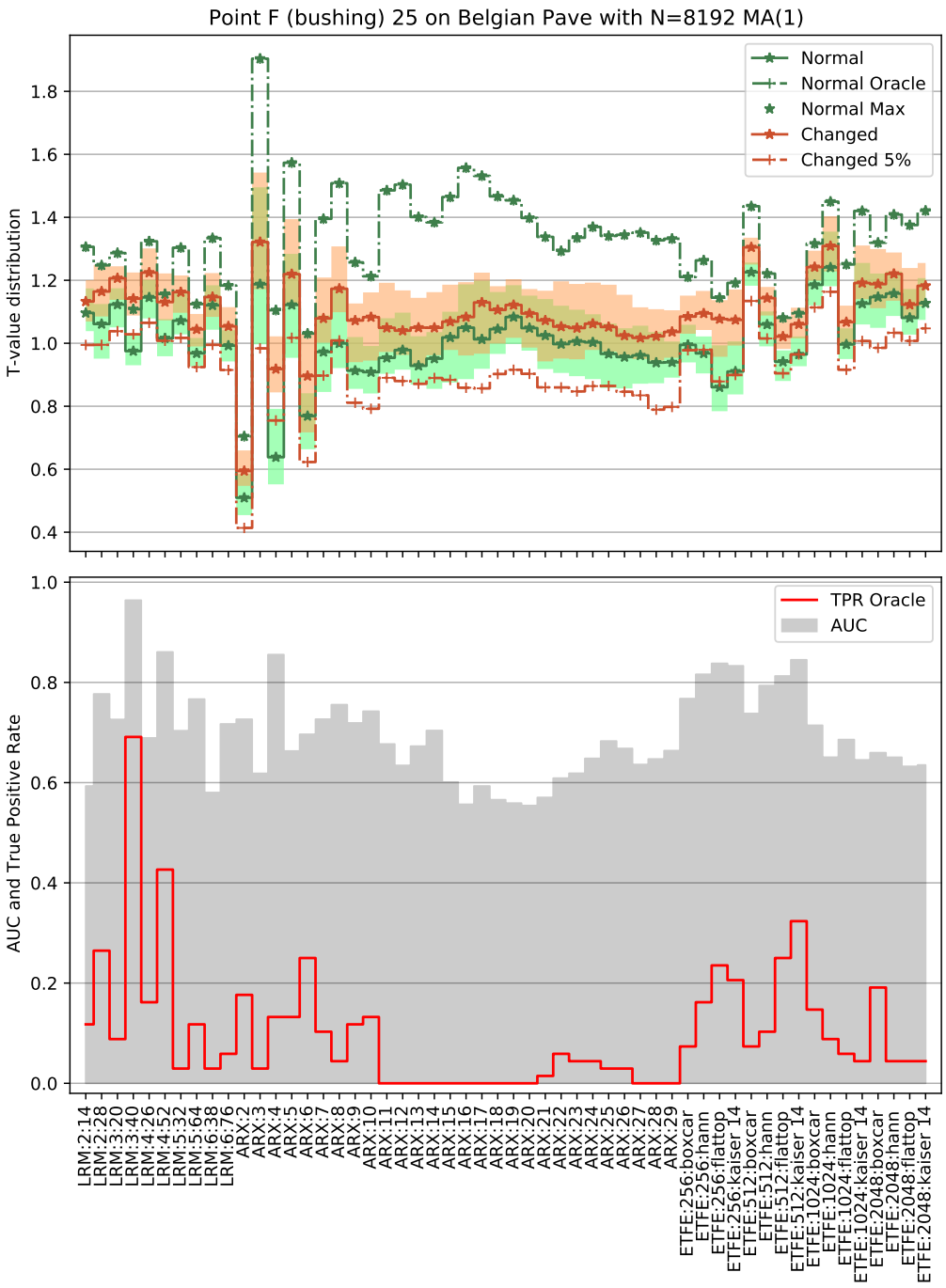
Point F (bushing) 25 on Belgian Pave with N=8192 MA(1)
Normal
Normal Oracle
Normal Max
Changed
Changed 5%
T-value distribution
TPR Oracle
AUC
AUC and True Positive Rate
LRM:2:14
LRM:2:28
LRM:3:20
LRM:3:40
LRM:4:26
LRM:4:52
LRM:5:32
LRM:5:64
LRM:6:38
LRM:6:76
ARX:2
ARX:3
ARX:4
ARX:5
ARX:6
ARX:7
ARX:8
ARX:9
ARX:10
ARX:11
ARX:12
ARX:13
ARX:14
ARX:15
ARX:16
ARX:17
ARX:18
ARX:19
ARX:20
ARX:21
ARX:22
ARX:23
ARX:24
ARX:25
ARX:26
ARX:27
ARX:28
ARX:29
ETFE:256:boxcar
ETFE:256:hann
ETFE:256:flattop
ETFE:256:kaiser 14
ETFE:512:boxcar
ETFE:512:hann
ETFE:512:flattop
ETFE:512:kaiser 14
ETFE:1024:boxcar
ETFE:1024:hann
ETFE:1024:flattop
ETFE:1024:kaiser 14
ETFE:2048:boxcar
ETFE:2048:hann
ETFE:2048:flattop
ETFE:2048:kaiser 14

Figure A.39

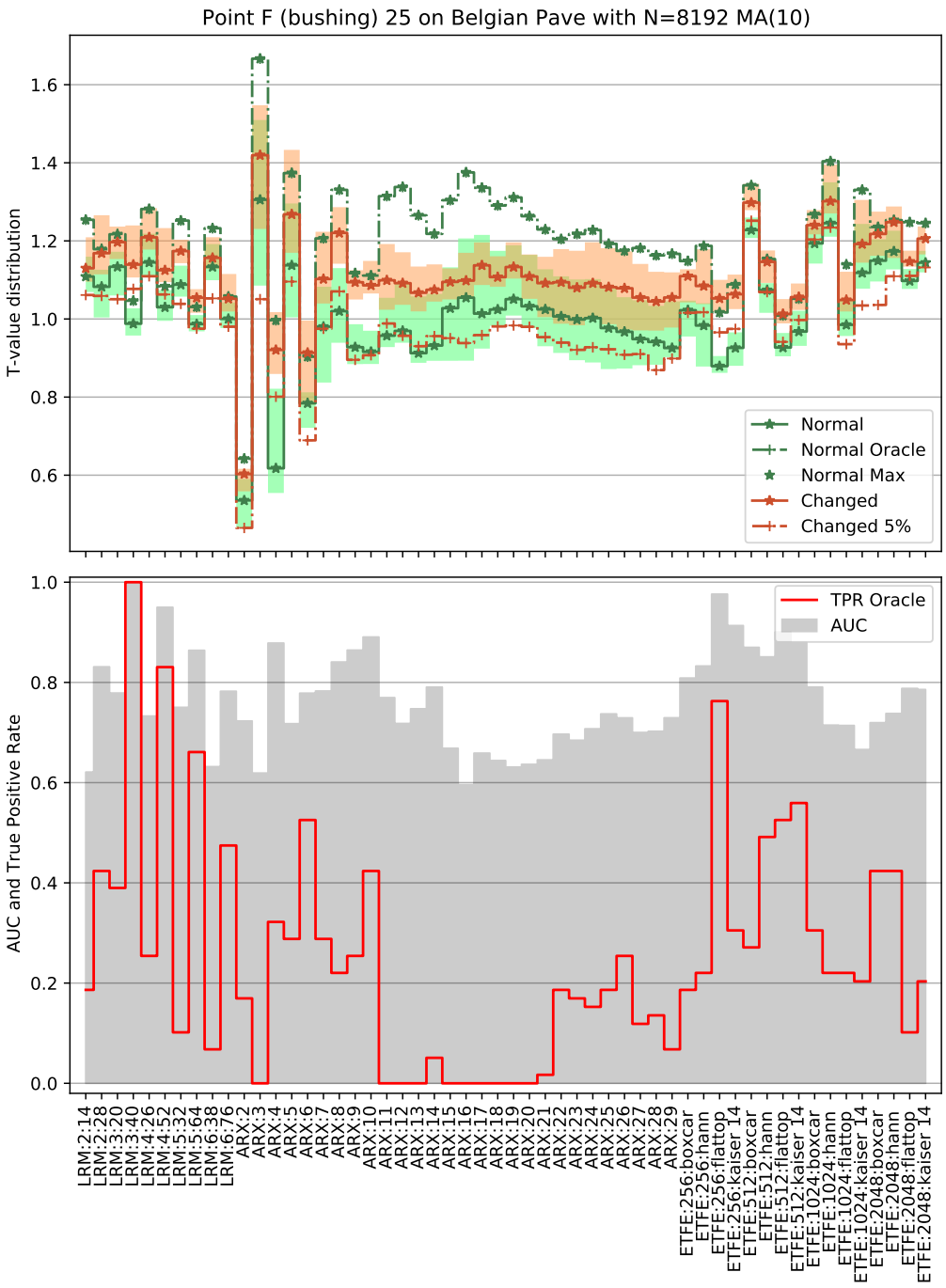
Point F (bushing) 25 on Belgian Pave with N=8192 MA(10)
T-value distribution
Normal
Normal Oracle
Normal Max
Changed
Changed 5%
AUC and True Positive Rate
TPR Oracle
AUC
LRM:2:14
LRM:2:28
LRM:3:20
LRM:3:40
LRM:4:26
LRM:4:52
LRM:5:32
LRM:5:64
LRM:6:38
LRM:6:76
ARX:2
ARX:3
ARX:4
ARX:5
ARX:6
ARX:7
ARX:8
ARX:9
ARX:10
ARX:11
ARX:12
ARX:13
ARX:14
ARX:15
ARX:16
ARX:17
ARX:18
ARX:19
ARX:20
ARX:21
ARX:22
ARX:23
ARX:24
ARX:25
ARX:26
ARX:27
ARX:28
ARX:29
ETFE:256:boxcar
ETFE:256:hann
ETFE:256:flattop
ETFE:256:kaiser 14
ETFE:512:boxcar
ETFE:512:hann
ETFE:512:flattop
ETFE:512:kaiser 14
ETFE:1024:boxcar
ETFE:1024:hann
ETFE:1024:flattop
ETFE:1024:kaiser 14
ETFE:2048:boxcar
ETFE:2048:hann
ETFE:2048:flattop
ETFE:2048:kaiser 14

Figure A.40

A.5 Life-cycle test

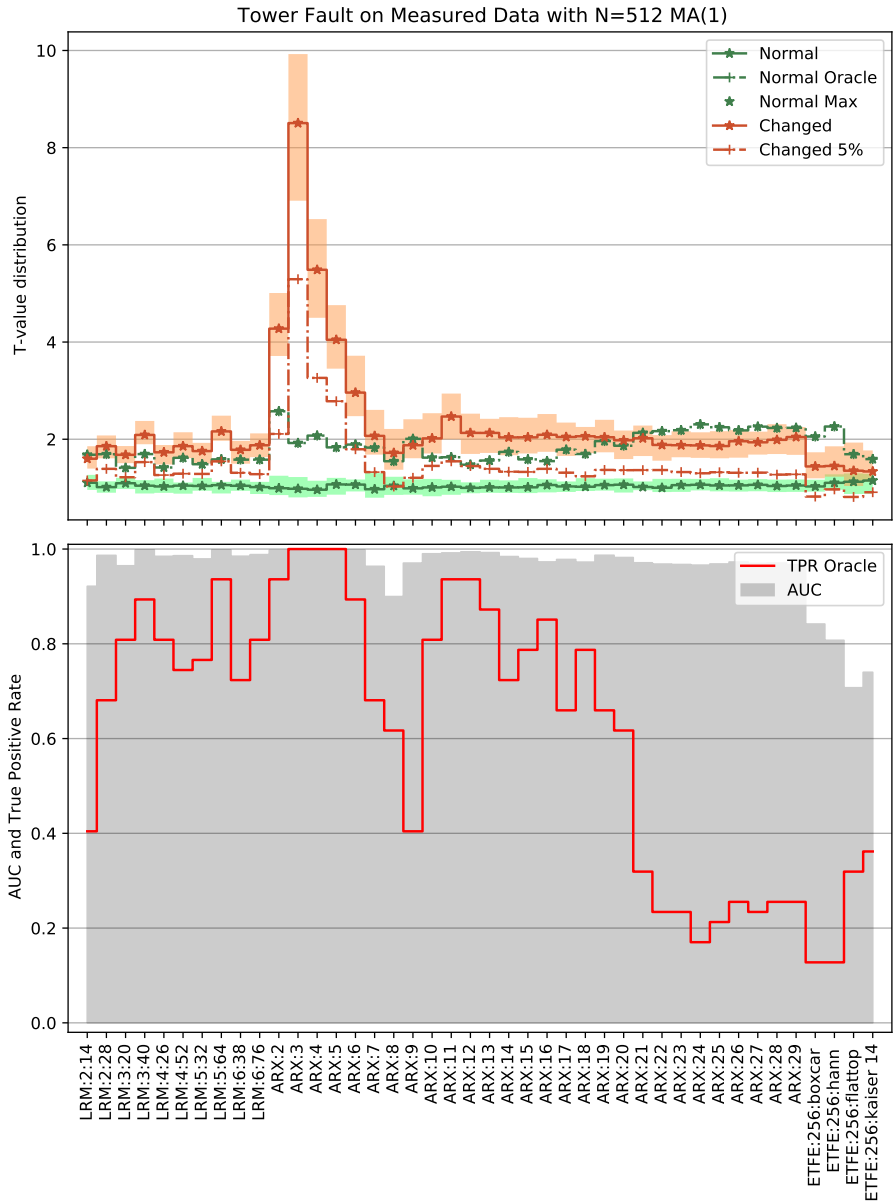
Tower Fault on Measured Data with N=512 MA(1)
T-value distribution
Normal
Normal Oracle
Normal Max
Changed
Changed 5%
AUC and True Positive Rate
TPR Oracle
AUC
LRM:2:14
LRM:2:28
LRM:3:20
LRM:3:40
LRM:4:26
LRM:4:52
LRM:5:32
LRM:5:64
LRM:6:38
LRM:6:76
ARX:2
ARX:3
ARX:4
ARX:5
ARX:6
ARX:7
ARX:8
ARX:9
ARX:10
ARX:11
ARX:12
ARX:13
ARX:14
ARX:15
ARX:16
ARX:17
ARX:18
ARX:19
ARX:20
ARX:21
ARX:22
ARX:23
ARX:24
ARX:25
ARX:26
ARX:27
ARX:28
ARX:29
ETFE:256:boxcar
ETFE:256:hann
ETFE:256:flattop
ETFE:256:kaiser 14

Figure A.41

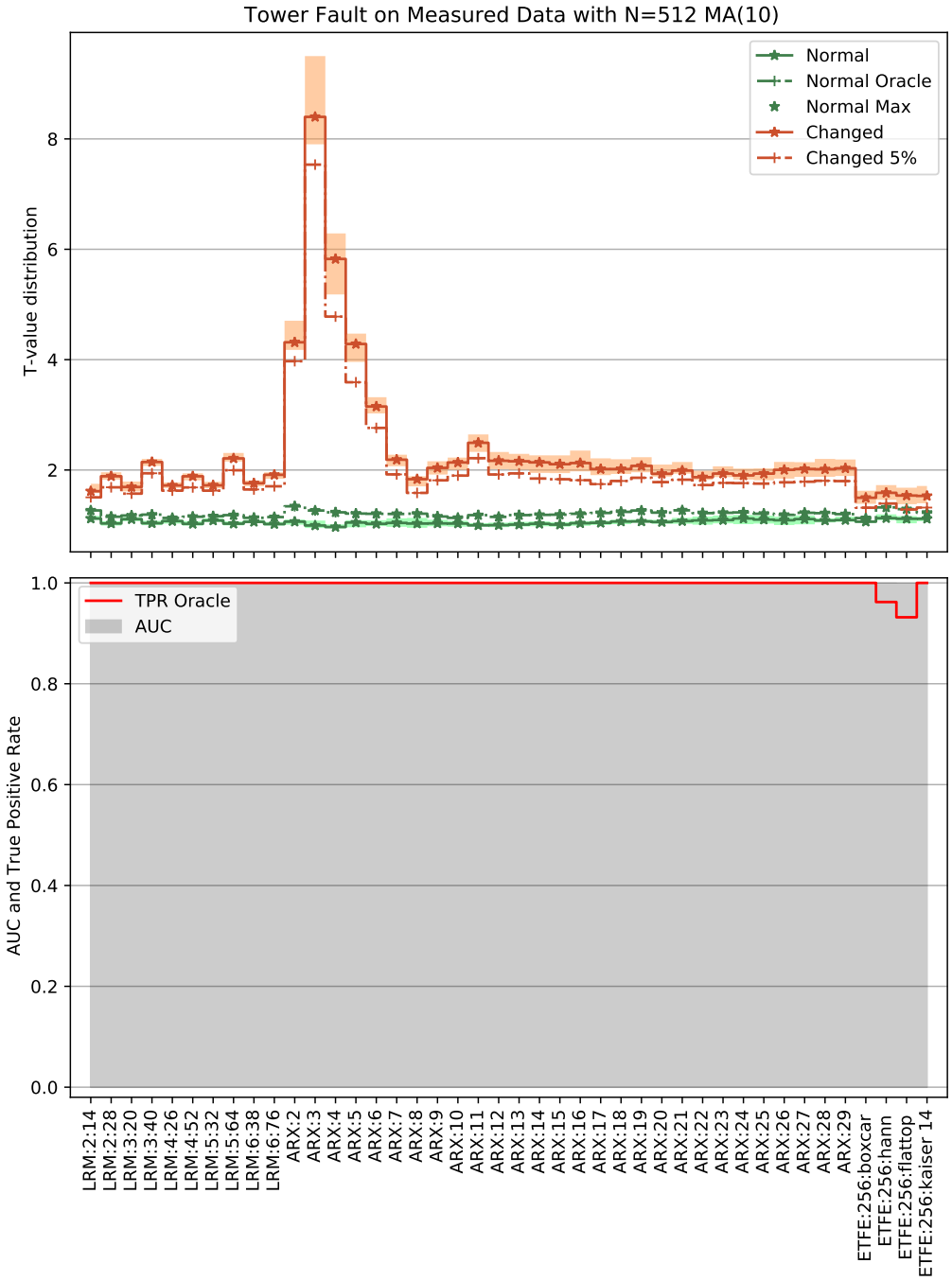
Tower Fault on Measured Data with N=512 MA(10)
Normal
Normal Oracle
Normal Max
Changed
Changed 5%
T-value distribution
TPR Oracle
AUC
AUC and True Positive Rate
LRM:2:14
LRM:2:28
LRM:3:20
LRM:3:40
LRM:4:26
LRM:4:52
LRM:5:32
LRM:5:64
LRM:6:38
LRM:6:76
ETFE:256:boxcar
ETFE:256:hann
ETFE:256:flattop
ETFE:256:kaiser 14

Figure A.42

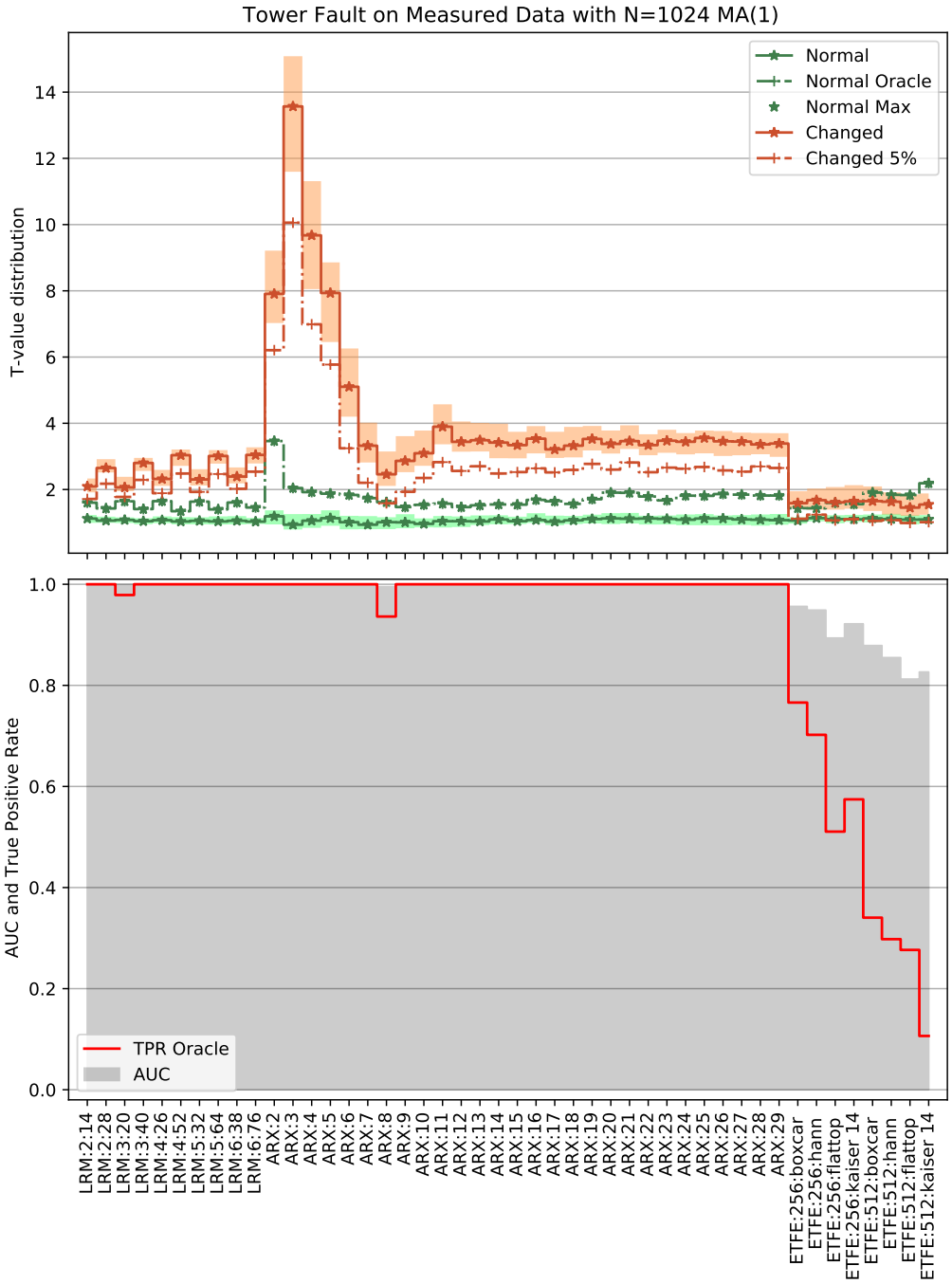
Tower Fault on Measured Data with N=1024 MA(1)
Normal
Normal Oracle
Normal Max
Changed
Changed 5%
T-value distribution
AUC and True Positive Rate
TPR Oracle
AUC
LRM:2:14
LRM:2:28
LRM:3:20
LRM:3:40
LRM:4:26
LRM:4:52
LRM:5:32
LRM:5:64
LRM:6:38
LRM:6:76
ARX:2
ARX:3
ARX:4
ARX:5
ARX:6
ARX:7
ARX:8
ARX:9
ARX:10
ARX:11
ARX:12
ARX:13
ARX:14
ARX:15
ARX:16
ARX:17
ARX:18
ARX:19
ARX:20
ARX:21
ARX:22
ARX:23
ARX:24
ARX:25
ARX:26
ARX:27
ARX:28
ARX:29
ETFE:256:boxcar
ETFE:256:hann
ETFE:256:flattop
ETFE:256:kaiser 14
ETFE:512:boxcar
ETFE:512:hann
ETFE:512:flattop
ETFE:512:kaiser 14

Figure A.43

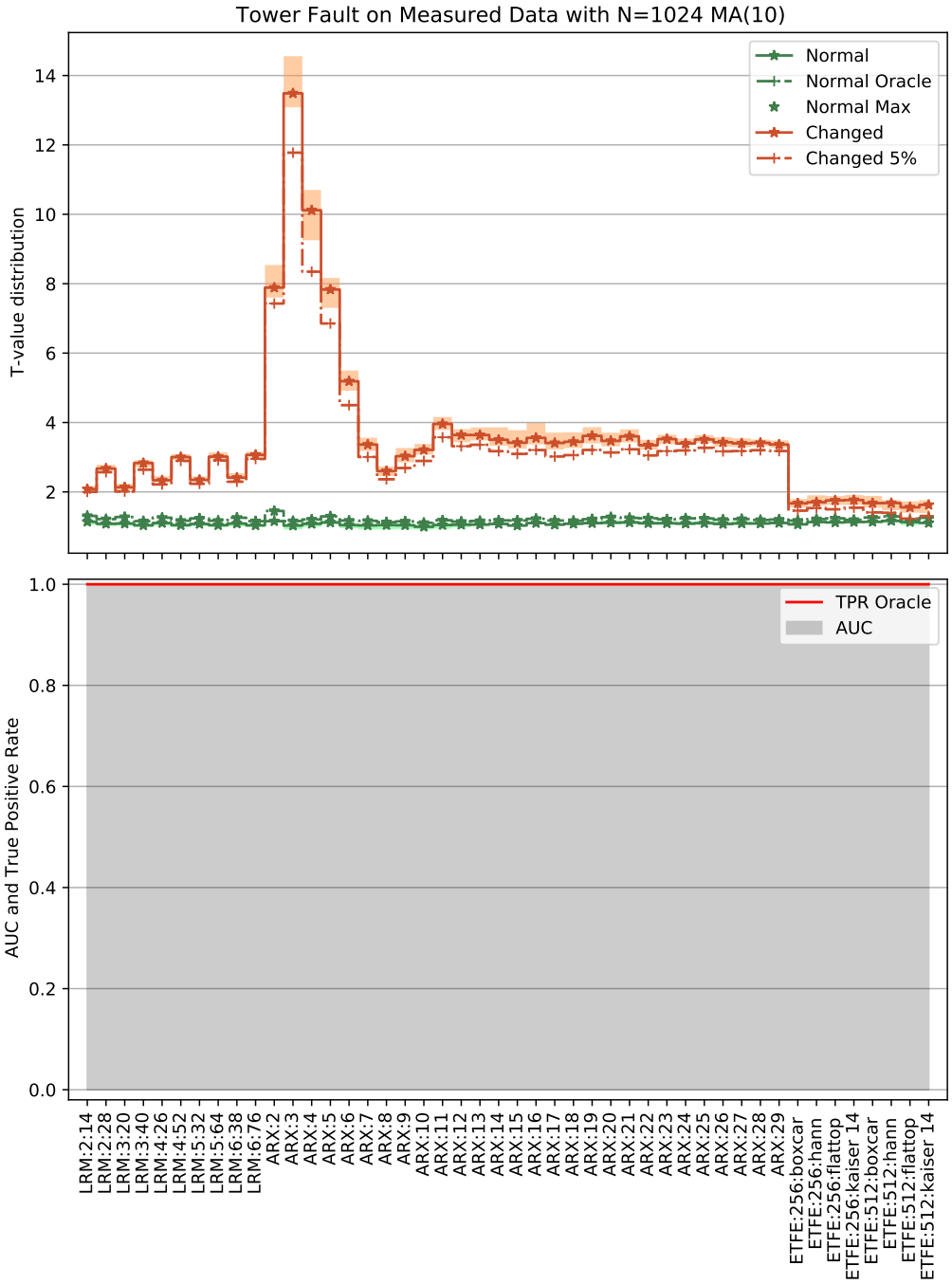
Tower Fault on Measured Data with N=1024 MA(10)
Normal
Normal Oracle
Normal Max
Changed
Changed 5%
T-value distribution
AUC and True Positive Rate
TPR Oracle
AUC
LRM:2:14
LRM:2:28
LRM:3:20
LRM:3:40
LRM:4:26
LRM:4:52
LRM:5:32
LRM:5:64
LRM:6:38
LRM:6:76
ARX:2
ARX:3
ARX:4
ARX:5
ARX:6
ARX:7
ARX:8
ARX:9
ARX:10
ARX:11
ARX:12
ARX:13
ARX:14
ARX:15
ARX:16
ARX:17
ARX:18
ARX:19
ARX:20
ARX:21
ARX:22
ARX:23
ARX:24
ARX:25
ARX:26
ARX:27
ARX:28
ARX:29
ETFE:256:boxcar
ETFE:256:hann
ETFE:256:flattop
ETFE:256:kaiser 14
ETFE:512:boxcar
ETFE:512:hann
ETFE:512:flattop
ETFE:512:kaiser 14

Figure A.44